ABSTRACT

Title of Dissertation: SPECIFIC HEAT AND NERNST EFFECT OF ELECTRON-DOPED CUPRATE SUPERCONDUCTORS

Hamza Balci, Doctor of Philosophy, 2004

Dissertation directed by: Professor Richard L. Greene
Department of Physics

This thesis consists of two separate studies on $Pr_{2-x}Ce_xCuO_4$ (PCCO), a member of the electron-doped high temperature cuprate superconductor family: specific heat and the Nernst effect.

We measured the specific heat of PCCO single crystals in order to probe the symmetry of the superconducting order parameter, to study the effect of oxygen reduction (annealing) on bulk properties of the crystals, and to determine properties like the condensation energy and the thermodynamic critical field. The order parameter symmetry has been established to be d-wave in the hole-doped cuprates. Experiments performed on electron-doped cuprates show conflicting results. Different experiments suggest s-wave symmetry, d-wave symmetry, or a transition from d-wave to s-wave symmetry with increasing cerium doping. However, most of these experiments are surface sensitive experiments. Specific heat, as a bulk method of probing the gap symmetry is essential in order to convincingly determine the gap symmetry. Our data proposes a way to reconcile all these conflicting results regard-

ing the gap symmetry. In addition, prior specific heat measurements attempting to determine thermodynamic properties like the condensation energy were not successful due to inefficient methods of data analysis or poor sample quality. With improvements on sample quality and data analysis, we reliably determined these properties.

The second part of this thesis is a study of the Nernst effect in PCCO thin films with different cerium dopings. We probed the superconducting fluctuations, studied transport phenomena in the normal state, and accurately measured H_{c2} by using the Nernst effect. After the discovery of the anomalous Nernst effect in the normal state of the hole-doped cuprates, many alternative explanations have been proposed. Vortex-like excitations above T_c, superconducting fluctuations, AFM fluctuations, and preformed Cooper pairs are some of these proposals. The electron-doped cuprates, due to their significant differences from the hole-doped cuprates in terms of coherence length and the phase stiffness temperature (a measure of superfluid density) are the ideal materials to test these ideas. Our data on the electron-doped cuprates does not show any anomalous Nernst effect, and hence it supports the superconducting fluctuations picture among the various proposals.

SPECIFIC HEAT AND NERNST EFFECT OF ELECTRON-DOPED CUPRATE SUPERCONDUCTORS

by

Hamza Balci

Dissertation submitted to the Faculty of the Graduate School of the
University of Maryland at College Park in partial fulfillment
of the requirements for the degree of
Doctor of Philosophy
2004

Advisory Committee:

Professor Richard L. Greene, Chairman
Professor J. Robert Anderson
Professor Steven M. Anlage
Professor Bryan Eichhorn
Professor Christopher J. Lobb

DEDICATION

To My Mother

ACKNOWLEDGEMENTS

I would like to thank Dr. Richard L. Greene for being my advisor in this thesis project. I have heard so many great things about Dr. Greene from the people who have worked with him that I feel whatever I say about him would be at best a repetition of my predecessors. Rick has been a great advisor with his deep insight and knowledge of superconductivity, an excellent teacher with his ability to make things clear and understandable, and an honest scientist willing to criticize even the most "obvious" conclusions of our work. Above all, his humble character and attractive personality is what made it a joy to be his student.

I had the luck of joining Greene's group when there were three post-docs with different areas of expertise in the group: Patrick Fournier, Amlan Biswas, and Vera Smolyaninova. Each of these post-docs (now they are all professors) have helped me in different ways. Particularly Vera taught me almost everything I know about specific heat measurements which ended up being a major part of this thesis. Amlan was the first guy to go to when a problem was too difficult for me. He usually had a simple explanation or a practical solution which saved the day. And Patrick always generously spent his time answering my questions, which I had many, in his tight schedule.

Now I should thank the graduate students which managed to keep the lab interesting for the long hours we spent together. Joshua Higgins has been a good friend and a patient colleague. His personality made things much easier and his patience with me was what kept things going. Mumtaz Qazilbash has set the standards of critical thought in the lab, and a reason for me to look into things deeper than I usually would. And of course I should mention Matt Sullivan for keeping our lab lively with his "frequent" visits. I have learned different things from all these people and I thank all of them.

In the later years of my PhD I had the chance to work with Yoram Dagan and Chris Hill. I thank Yoram for sharing his deep insight of superconductivity with me and for letting me have the time I need on the PPMS in the tight schedule of the machine. I also thank Chris for the Labview programs he wrote for me, and the thin film samples he prepared.

I thank Dr.Lobb for always having an open door for my questions. He always had a simple explanation for the questions which I was not able find an answer for in the papers or in the books.

I was also lucky to have Bob Anderson as my academic advisor in the graduate school and the first person to interact with in this country. Dr. Anderson saved me from a couple of courses, and he was always a relief for me as an international student when things got stuck because of my inexperience in the graduate school.

I would like to thank Dr. Anlage and Dr. Yakovenko for sharing their knowledge and insight of physics with me. I also thank Dr. Eichhorn for helping me prepare my thermometers, and having his lab open for me. I am grateful to have the chance to interact with such distinguished scientists.

I thank Z.Li for teaching me how to grow single crystals, and preparing many samples for me which made the specific heat part of this thesis possible. I also thank Doug Benson and Brian Straughn for helping me many times with equipment related problems, and for keeping things working in the center.

Finally, I cannot express enough gratitude for my mother who has supported and motivated me for many years and who has been behind me in every thing I do.

TABLE OF CONTENTS

LIST OF TABLES

LIST OF FIGURES

Table of Symbols Abbreviations	
β	the coefficient of the phonon specific heat
τ	relaxation time
α	Peltier conductivity
σ	electrical conductivity
$\gamma(0)$	zero-field residual specific heat
γ_0	impurity band-width
Δ_0	maximum of the superconducting gap
ξ_0	the coherence length at T=0
μ_0	permeability of free space
θ_D	Debye temperature
γ_n	Sommerfeld coefficient
ΔT_c	the width of the superconducting transition
Bi-2212	$Bi_2Sr_2CaCu_2O_8$
EDS (EDX)	energy dispersive x-ray spectroscopy
e_y	Nernst signal
H_{c1}	lower critical magnetic field
H_{c2}	upper critical magnetic field
k	thermal conductance
LSCO	$La_{2-x}Sr_xCuO_4$
NCCO	$Nd_{2-x}Ce_xCuO_4$
PCCO	$Pr_{2-x}Ce_xCuO_4$
STO	$SrTiO_3$
T_c	critical temperature
WDS (WDX)	wavelength dispersive x-ray spectroscopy
YBCO	$YBa_2Cu_3O_7$

Table 1: Table of symbols and abbreviations used in the thesis.

Chapter 1

Introduction

Superconductivity was discovered experimentally by H. Kamerlingh Onnes in 1911 on a mercury sample right after ^{4}He was liquified[1]. In the following years many metals and simple compounds were found to exhibit superconductivity below 23 K. However, the mechanism of this low temperature phenomenon was not understood until a microscopic theory was developed by Bardeen, Cooper, and Schrieffer (BCS) in the 1950's [2, 3]. BCS theory showed that superconductivity was a result of the condensation of pairs of electrons (Cooper pairs) into a coherent ground state, and the pairing mechanism was phonon mediated (the idea of electrons forming pairs due to electron-phonon interaction was first suggested by Fröhlich before BCS theory [4]). The Cooper pair formation, which implies an attraction between the electrons, can be understood as follows: an electron in a solid forms a potential well around itself by attracting the positive ions around them. When two such electrons approach each other, they can reduce their energy by sharing each others potential well (through phonon exchange between the ions), and forming a larger potential well. By sharing each others potential well they effectively attract each other. BCS theory made many predictions almost all of which were proven correct by experiments, which established it as the microscopic theory of superconductivity by the late 1960's. For a comprehensive treatment of superconductivity as of 1968 see volumes I and II of the book "Superconductivity" (collection of review articles

written by distinguished experts of each field) edited by R. D. Parks [5].

The upper limit for superconductivity was projected from BCS theory to be around 30-40K since it was thought that lattice instabilities would destroy Cooper pairing in the strong coupling regime [6]. For many years this prediction was not challenged experimentally and the highest known transition temperature (T_c) achieved was T_c=23 K in the A-15 compounds. Then, in 1986 Alex Müller and Georg Bednorz discovered superconductivity in a ceramic sample of LaBaCuO (LBCO) at ≈30 K [7]. This unexpected discovery was the beginning of a new era in the history of superconductivity, and researchers around the world started trying every possible combination of materials to look for superconductivity in these copper oxide ceramics, or cuprates. Six months after the discovery of superconductivity in LBCO, groups from the University of Alabama-Huntsville and University of Houston synthesized a new superconductor by substituting yttrium for lanthanum in LBCO [8]. The new compound, $YBa_2Cu_3O_7$ (YBCO), was superconducting at ≈90 K! In the following years such high transition temperatures were found in many different systems [8, 9, 10] and the transition temperature of the cuprates has been lifted up to 138 K by using a mixture of thallium, mercury, copper, barium, calcium, and oxygen. Clearly 138 K is much higher than 23 K (the highest T_c before cuprates), which suggests that BCS theory and the phonon induced pairing mechanism may not the right models to describe superconductivity in these multi-component and complicated materials. The cuprates are also called high-temperature superconductors (HTSC) to contrast them with the prior "low-T_c" materials.

The most important question of high-temperature superconductivity research today, which is also the motivation for our research, is to understand the mechanism of high-temperature superconductivity. Such understanding could in turn open the way for the synthesis of superconductors of even higher transition temperatures. When making a comparison between the mechanism of superconductivity in high-T_c cuprates and in the conventional superconductors, the first question to ask is whether

superconductivity occurs as a result of condensation of electrons into a coherent state. In other words "are there Cooper pairs in cuprate superconductors"? The answer to this question has been given by experiments measuring flux quantization in cuprates, and similar to conventional superconductors electron pairs are found to be responsible for superconductivity in the cuprates.

The next step is obviously to understand if the electron pairs are coupled through the electron-phonon interaction, or to answer the question "what is the pairing mechanism in cuprates"? The answer to this question has not been firmly established yet, and there are **many** proposed answers. However, candidate explanations involving proximity to an antiferromagnetic (AFM) state have been gaining more support than the other proposals in the last several years (see references [11, 12, 13, 14] for detailed reviews about the mechanism of superconductivity in high-T_c cuprates).

There are several reasons for the increased popularity of the models involving the proximity to an AFM state, most importantly the confirmation of their pairing symmetry prediction in one of the cuprate families-the hole-doped cuprates (an overview of the two cuprate families is given in Section 1.1). Electrons in conventional superconductors pair up due to phonons, and therefore the pairing interaction is isotropic, i.e. there is no preferred direction in k-space. The pairing of the electrons around the Fermi surface creates a range of energies which are depleted of single electron excitations. This is called the superconducting gap, and it is a fundamental property of superconductivity in both the low-T_c and high-T_c superconductors. The isotropic electron-phonon interaction leads to an isotropic superconducting gap (there are several exceptions to this statement like MgB_2 [15]) This type of pairing symmetry is called s-wave symmetry. However, models involving AFM do not predict an isotropic pairing symmetry, instead they predict a pairing symmetry in which the pairing amplitude (superconducting gap) goes to zero on four points (nodes) around the Fermi surface and in which the phase of the pairing symmetry changes sign across these nodes. This type of symmetry is called d-wave symmetry (see Fig.

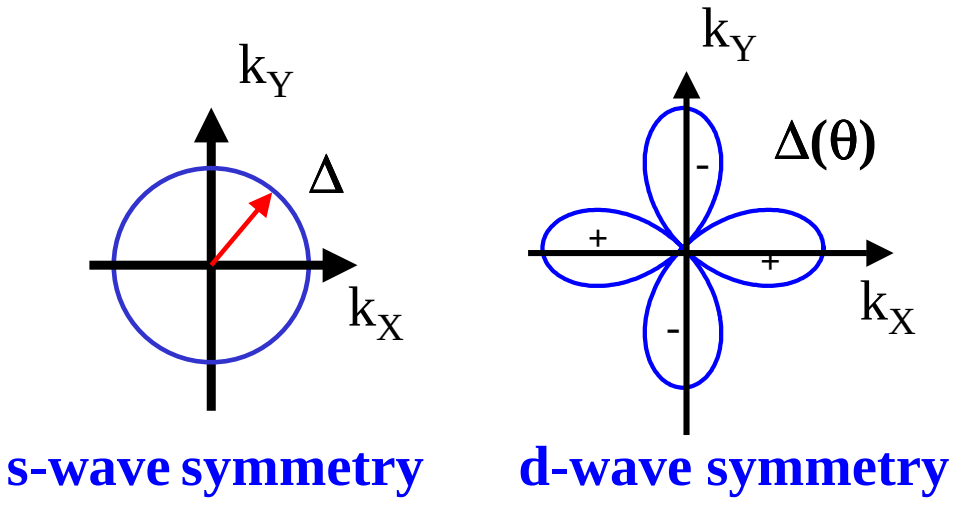

Figure 1.1: Superconducting gaps with s-wave and d-wave symmetry.

1.1).

The d-wave symmetry has been firmly established experimentally for the hole-doped cuprates, however the situation is not as clear in the other cuprate family- the electron-doped cuprates. It is essential to know the symmetry of the electron-doped cuprates as well. One of the main questions that this thesis deals with is the pairing symmetry in electron-doped cuprates, and specific heat measurements are used to probe the gap symmetry of the electron-doped cuprates.

Before discussing the experiments probing the symmetry of the order parameter in the two families of cuprates, a brief overview of the similarities and differences between electron and hole-doped cuprates will be made.

1.1 Electron vs hole doping of the cuprates

Despite the absence of any experimental proof, the copper oxide planes are considered to be responsible for superconductivity in these materials. The cuprate superconductors are obtained by doping a parent compound which is an antiferro-

magnetic insulator with holes or electrons. Depending on the type of doping, the cuprates are called electron-doped cuprates [16] or hole-doped cuprates. For example $La_{1.85}Sr_{0.15}CuO_4$ (LSCO) is a superconductor that has a T_c=39K. The parent compound for LSCO is La_2CuO_4 (LCO) which is an antiferromagnetic (AFM) insulator (for antiferromagnetism in La_2CuO_4 see Ref. [17] and references therein). By replacing La^{3+} (lanthanum) with Sr^{2+} (strontium), holes are introduced to the copper-oxide planes. At about 0.02 extra holes per copper oxide plane, the AFM is suppressed, and the material enters into a new state, which is still not well-understood. If the material is doped further with holes superconductivity appears with a very low transition temperature at 0.06 extra holes per copper oxide plane. Further doping increases the number of carriers per copper-oxide plane and also increases T_c. At about 0.15 extra holes per copper oxide plane the T_c reaches a maximum temperature, and then reduces with further doping. The superconductivity completely disappears when the carrier density reaches 0.3 extra holes per copper oxide plane. Hence in a doping versus temperature phase diagram, superconductivity occurs under a dome-like structure (see Fig. 1.2). The electron-doped cuprate NCCO has a very similar phase diagram in which superconductivity is obtained by replacing Nd^{3+} with Ce^{4+} and hence doping the copper oxide planes of an AFM insulator with electrons [18]. The magnetic properties of electron-doped cuprates and the suppression of AFM with cerium doping have been studied mainly by neutron scattering [19, 20, 21] and muon spin resonance [22]. Similar to the hole-doped LSCO where the maximum T_c is obtained at 0.15 extra holes per CuO plane, the maximum T_c in the electron-doped NCCO (or PCCO) is obtained at 0.15 extra electrons. However, the superconducting dome in electron-doped cuprates is much narrower in doping, and lower in temperature (see Fig. 1.2).

The crystal structure of electron-doped and hole-doped cuprates is very similar as can be seen in Fig. 1.3. Fig. 1.3 shows a comparison of the crystal structure in LSCO and NCCO. LSCO has an orthorhombic structure, whereas NCCO has a tetragonal

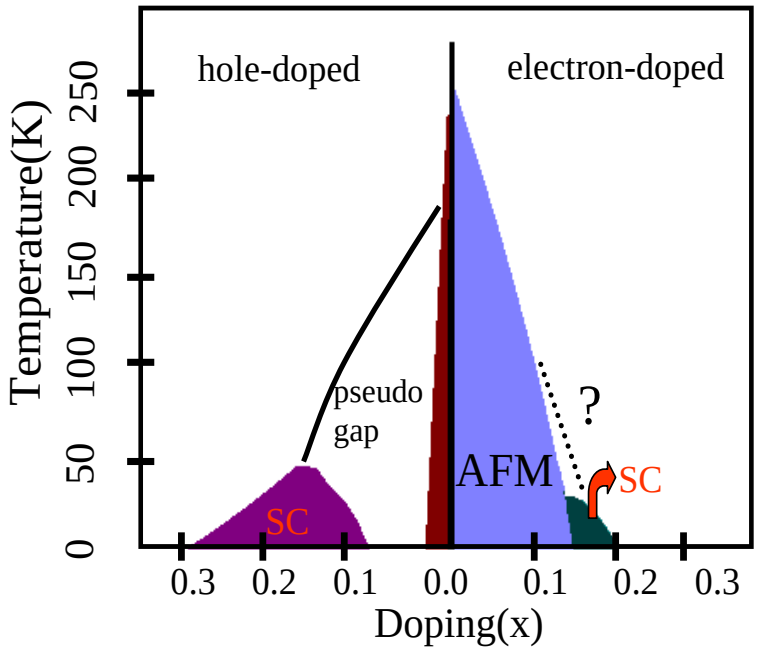

Figure 1.2: The right side on the x-axis is the phase diagram for electron-doped cuprate superconductor $Nd_{2-x}Ce_xCuO_4$ (NCCO) and the left side is the phase diagram for hole-doped cuprate LSCO. The "?" on the electron-doped side is due to the lack of consensus regarding the pseudogap state in the electron-doped cuprates.

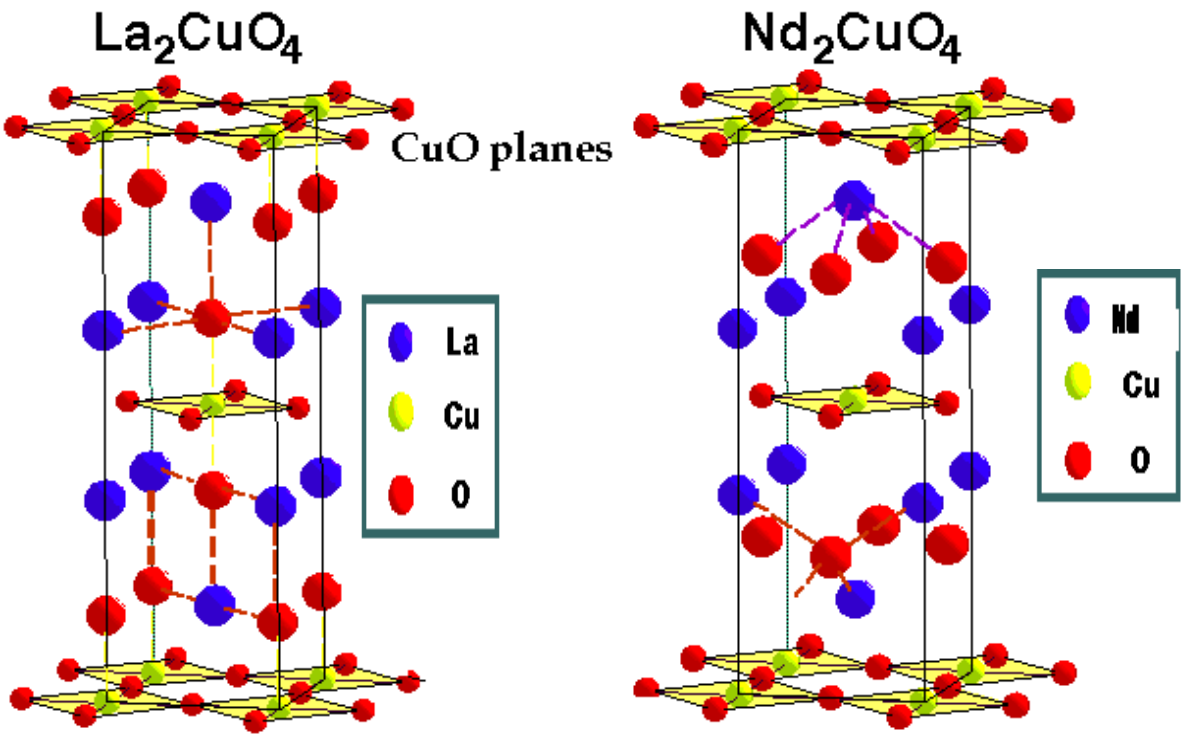

Figure 1.3: Crystal structure of the parent compound for the hole doped cuprate LSCO, and electron-doped cuprate NCCO.

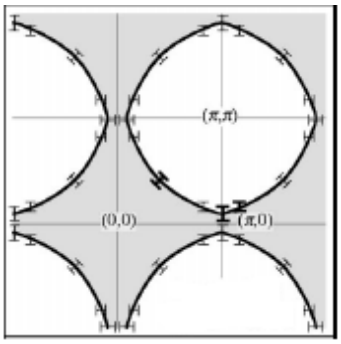

Figure 1.4: Schematic Fermi surface of LSCO x=0.15 from Ref [23].

crystal structure [16]. Both LSCO and NCCO have a perovskite structure with one layer of CuO plane, however unlike LSCO NCCO does not have the apical oxygen. Our current understanding is that in both of the cuprate families the elements between the copper-oxide planes act like a charge reservoir for the copper-oxide planes and they are not otherwise involved in superconductivity.

In addition to the crystal structure the Fermi surfaces are also similar for the hole and electron-doped cuprates, they both have cylindrical Fermi surfaces. See Fig. 1.4 for a schematic of the Fermi surface in cuprates, and Fig. 1.5 for ARPES (Angular Resolved Photoemission Spectroscopy) pictures of the Fermi surface of electron-doped and hole doped cuprates. An important point that will be referred to later in the specific heat chapter is the green areas in Fig. 1.5-a. These areas are the intersecting regions of the magnetic Brillouin zone with the Fermi surface, and they are the areas in which the AFM fluctuations are strongest. They are called hot-spots, and they are common in both the electron and hole-doped cuprates (Fig. 1.4 is from Ref. [23], Fig. 1.5-a is from Ref. [24] and Fig. 1.5-b is from Ref. [25]).

The fact that electron-doped and hole-doped cuprates look very similar in terms of crystal structure, Fermi surface, and phase diagram suggests that whatever mechanism makes one of them superconducting is responsible for the superconductivity in the other as well, and hence the pairing symmetry of both families should be the

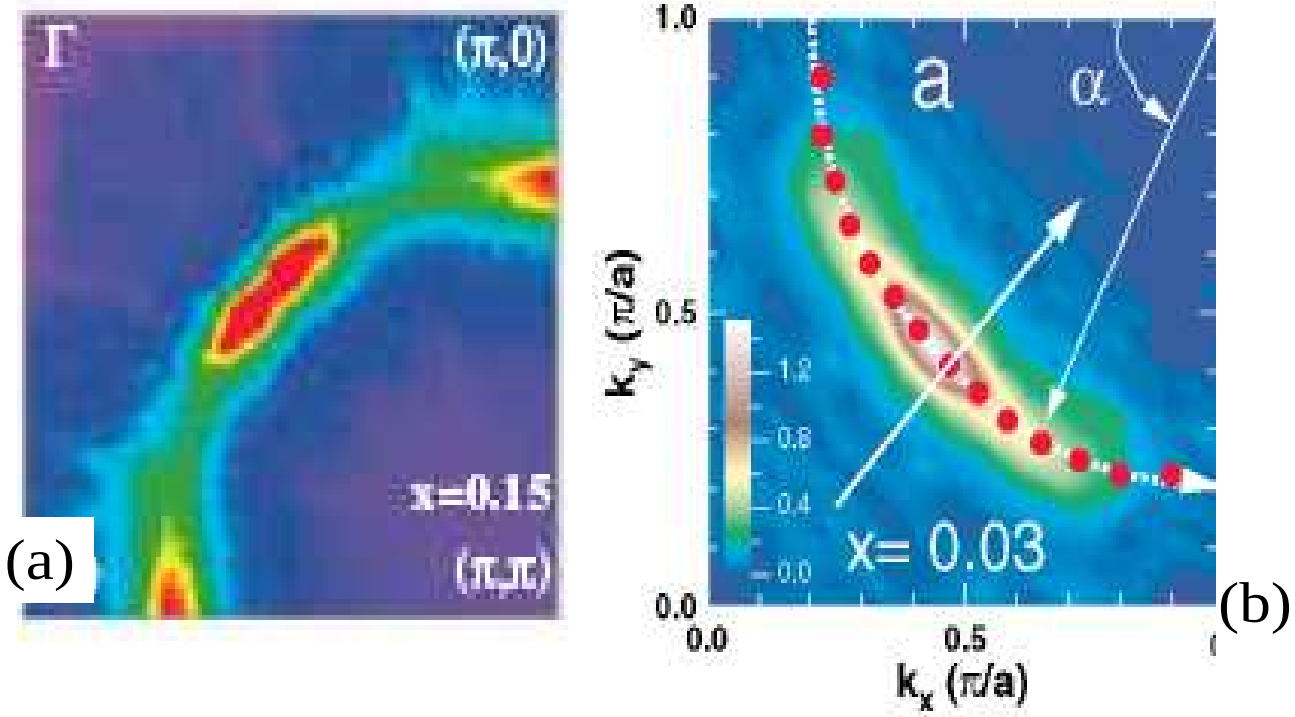

Figure 1.5: (a)-The Fermi surface of electron-doped cuprate NCCO from Ref. [24] and (b)- hole doped cuprate LSCO from Ref. [25]. Even though the dopings of the two materials are different, the general features of the Fermi surfaces are similar.

same. However, even though the general features look alike, the details are quite different between the two families. First of all, the superconductivity occurs in a much narrower doping range in the electron-doped family compared to the hole-doped family. In addition T_c's in the electron-doped family are much lower than in the hole-doped family. Another main difference between the two families is the doping range in which AFM is observed; in the electron-doped cuprates the AFM occurs over a much broader doping range. In order to address the question of whether these quantitative differences between the two families affect the pairing mechanism, we studied the pairing symmetry in the electron-doped cuprates and compared it with the established pairing symmetry, d-wave, of the hole-doped cuprates.

The pairing symmetry of hole-doped cuprates has been well-studied by many experiments which include both surface-sensitive experiments and bulk measurements. Consistent results from these different experiments have shown that the gap symmetry is $d_{x^2-y^2}$ in the hole-doped cuprates [26, 27]. The situation is less clear in the electron-doped cuprates. Early penetration depth [28, 29, 30] and Raman scattering [31] experiments on electron-doped(n-type) $Nd_{1.85}Ce_{0.15}CuO_4$ (NCCO) suggested *s*-wave symmetry. Recent penetration depth [32, 33], tri-crystal [34], photoemission [24, 35], Raman scattering [36] and point contact tunneling experiments [37] on NCCO and $Pr_{2-x}Ce_xCuO_4$ (PCCO), mostly x=0.15, favor d-wave symmetry. In addition to these measurements which show s-wave or d-wave symmetry, there are penetration depth [38] and point contact tunnelling [37] experiments that have shown evidence for a change in the order parameter as the doping changes from under-doped (d-wave) to over-doped (s-wave). The latest penetration depth measurements performed on high quality PCCO thin films showed an anisotropic s-wave symmetry for all dopings [39]. However, since most of these prior measurements on the n-type cuprates are surface sensitive, there is a need for bulk measurements (e.g. specific heat) to convincingly determine the pairing symmetry, as was the case for the p-type cuprates [40, 41, 42, 43]. Our specific heat study is an attempt to

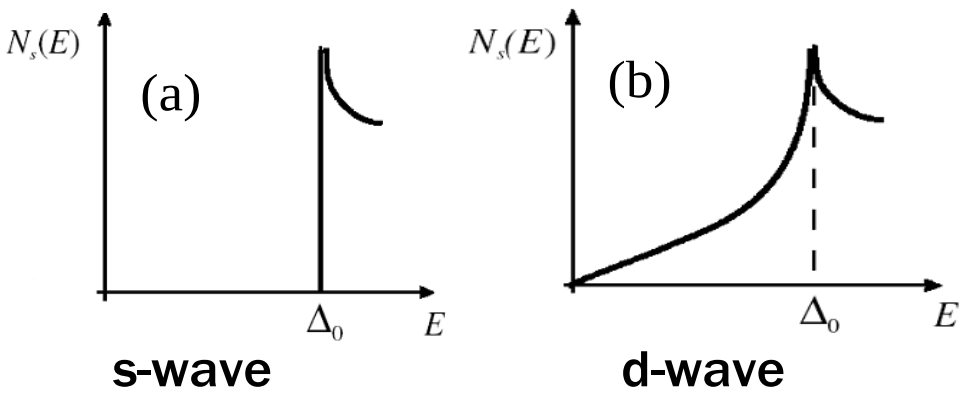

Figure 1.6: Density of electronic states for s-wave and d-wave superconductors. This figure is from Ref. [45].

satisfactorily answer the question of pairing symmetry in electron-doped cuprates.

1.2 Introduction to specific heat

Specific heat in the simplest form is the amount of heat necessary to increase the temperature of a material by a unit amount. Depending on whether the pressure or the volume is kept constant, the specific heat is shown by C_p or C_v respectively. In our measurements the pressure is kept constant, hence C_p is measured. The specific heat of a metal in general has contributions from electrons, phonons, and possibly from magnetic structure of the material. For an extensive review of specific heat of a metal at low temperatures see Ref. [44].

The electronic specific heat of a metal is given by:

$$C_{el} \equiv \frac{\partial u}{\partial T} = \frac{\partial}{\partial T} \int E f(E) N(E) dE \tag{1.1}$$

where u is the internal energy, $N(E)$ is the density of states, and $f(E)$ is the Fermi-Dirac distribution function [46]. As mentioned, the specific heat is sensitive to low temperature electronic excitations. Different gap symmetries have different density of electronic states (see Fig. 1.6). Conventional low-T_c superconductors

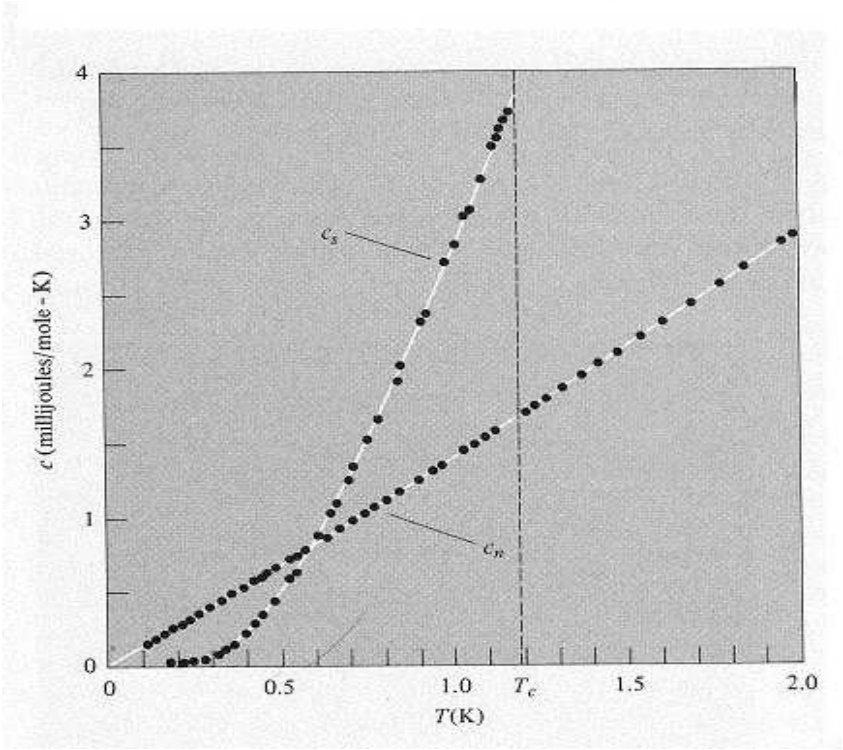

Figure 1.7: Electronic specific heat of aluminum in the normal (H>H_c) and superconducting states. The low temperature electronic specific heat decays exponentially to zero. This figure is from Ref. [48].

show an s-wave gap symmetry, i.e the gap is non-zero in every direction on the Fermi surface (see Fig. 1.1). Since there is a non-zero gap everywhere on the Fermi surface, the probability of creating a quasiparticle due to thermal fluctuations goes exponentially to zero as $T \rightarrow 0$. This shows up in specific heat as an exponential temperature dependence as $T \rightarrow 0$, $C_{el} \propto T^{-1.5} e^{-\Delta/kT}$ [47], where Δ is the energy gap. See Fig. 1.7 for an example of exponential decay of electronic specific heat in a conventional superconductor aluminum, and references [48, 49, 48, 50] for specific heat measurements in different low-T_c superconductors.

For a $d_{x^2-y^2}$-wave superconductor electronic excitations exist even at the lowest temperatures (see Fig. 1.6), since the superconducting gap goes to zero in certain directions (the nodes, i.e. along the 110 direction in k-space). The $d_{x^2-y^2}$ super-

conducting gap can be simply represented as $\Delta = \Delta_0 \cos(2\theta)$, where Δ_0 is the gap maximum. Due to the finite slope of the gap as one gets close to the nodes ($\theta = 45^o$), the density of states increases linearly with energy, $N(E) \propto E$. At very low temperatures, $T \ll \Delta$, only the quasiparticle spectrum close to the nodes is populated. Therefore, for low temperatures one can insert $N(E) \propto E$ in Eq. 1.1, and integrate around a $k_B T$ of the Fermi energy. This first order approximation results in an electronic specific heat that is proportional to T^2, $C_{el} \propto T^2$ for T$\ll$T$_c$ [51].

In the mixed state, there are two types of quasiparticle excitations in the bulk of the superconductor: bound states inside the vortex cores, and extended states outside the vortex cores. In conventional s-wave superconductors, the in-core bound states dominate the quasiparticle spectrum. The vortex core and the bound states in these cores can be modelled like a particle in a box. As is well-known the spacing between the bound energy levels of a particle in a box is inversely proportional to the square of the size of the box ($\varepsilon_0 = \hbar^2/m\xi^2$, where ε_0 is the spacing between the energy levels, or as is also called in literature the "minigap", and ξ is the coherence length). As the size of the box gets larger, the population of these energy levels approaches a continuum. Thus the in-core bound states of a conventional s-wave superconductor are heavily populated due to their large coherence length, and therefore dominate the quasiparticle excitation spectrum [52]. Since the core of the vortices is assumed to be a continuum of quasiparticle excitations, a single vortex can be considered as a unit for these quasiparticle excitations. The number of vortices is linearly proportional to the magnetic field H, therefore the electronic specific heat, which is a measure of the density of these quasiparticle excitations, is also linearly proportional to the magnetic field [52]. For an example of field dependence of a conventional superconductor see Ref. [53]. A rigorous derivation gives:

$$C_{el} = \kappa \gamma_n T \frac{H}{H_{c2}(T)}, \tag{1.2}$$

where γ_n is the Sommerfeld coefficient, κ is a geometrical factor of order 1, and

$H_{c2}(T)$ is the upper critical field at the particular temperature the measurement is performed. The Sommerfeld constant, γ_n, is proportional to the density of states at the Fermi level ($N(E_f)$) [54]:

$$\gamma_n = \frac{1}{3}\pi^2 N(E_f) k_B^2. \tag{1.3}$$

In a superconductor with lines of nodes(i.e. a d-wave superconductor), the extended quasiparticles outside the vortex core dominate the excitation spectrum. Volovik *et al.* [51, 55] showed that the supercurrents around the vortex cores cause the energy spectrum of these extended quasiparticles to be Doppler shifted by an amount $\hbar\vec{k}.\vec{v}_s$, where $\vec{k}$ is the quasiparticle momentum and $\vec{v}_s$ is the superfluid velocity. This energy shift excites the quasiparticles above the small superconducting gap near the nodes. This mechanism is not important in conventional s-wave superconductors since a magnetic field of the order of H_{c2} would be needed to excite the quasiparticles above the superconducting gap. The Doppler shift is most effective near the nodes on the Fermi level. It is enough to look at the density of these excitations at the Fermi level in order to understand the $H^{1/2}$ dependence of the electronic specific heat. The quasiparticle DOS at the Fermi level for a single vortex can be written as:

$$N(0) = \int \frac{d^3k}{(2\pi)^3} \int d^2r \delta[E(k,r) - \hbar\vec{k}.\vec{v}_s] \tag{1.4}$$

The average superfluid velocity $< v_s >$ is inversely proportional to the inter-vortex spacing $R(H)$. On the other hand, the area integral over r in Eq. 1.4 should be extended from the core of one vortex until the core of the next vortex since the extended quasiparticles rather than the vortex cores are the dominant contribution. This integral results in an area proportional to $R^2(H)$. Therefore, N(0) is proportional to $R^2(H) \times 1/R(H) = R(H)$.

The inter-vortex spacing $R(H)$ is proportional to inverse square root of the magnetic field, $R(H) \propto 1/\sqrt{H}$. The field dependence of the inter-vortex spacing can be

qualitatively understood as follows: Since extended quasiparticles are considered, the vortex can be considered to occupy an area of A_0 (not the area of the vortex-core) which extends up to the next vortex. This area in the simple case of a square lattice is just equal to $R^2(H)$, and in general it is proportional to the square of the inter-vortex separation. Therefore the total area of the sample is occupied by n vortices each of which occupies an area of A_0. Hence, $nA_0=A_{sample}$=constant. Since the number of vortices is proportional with H, the total area occupied by each vortex is proportional to 1/H. Since $A_0 \propto R^2(H)$, and $A_0 \propto 1/H$ then $R(H) \propto 1/\sqrt{H}$. The number of vortices is linearly proportional to H, therefore the quasiparticle DOS is proportional to $H \times 1/\sqrt{H} = \sqrt{H}$ [51, 55, 56]. Thus, the electronic specific heat for a d-wave superconductor is proportional to $\sqrt{H}$ at T=0. For non-zero temperatures there is a temperature dependent minimum field after which the $\sqrt{H}$ dependence should be observed [51, 55]. For more detailed discussions of the quasiparticle DOS around a d-wave vortex and the influence of d-wave symmetry on the vortex-core see references [57, 58, 59].

In addition to electronic excitations the specific heat includes the phonon contribution and a possible Schottky contribution. At low enough temperatures the phonon specific heat has a T^3 temperature dependence [54]:

$$C_{phonon} = \beta T^3 = \frac{12\pi^4}{5} n k_B (\frac{T}{\theta_D})^3 \tag{1.5}$$

where θ_D is the Debye temperature and n is the number of atoms per formula unit. The Debye temperature and β are the two often quoted parameters, and they are related to each other by the simple relation: $\theta_D = 10(\frac{1944n}{\beta})^{1/3}$[60], where β is in units of mJ/moleK^4. The phonon specific heat is independent of magnetic field. As a rule of thumb the phonon specific heat shows this T^3 type temperature dependence at $T < \theta_D/50$. At higher temperatures higher order terms of the lattice harmonic approximation (T^5, T^7, ...etc) should be included [54]. Our experiments are all in the temperature range that the T^3 type description is valid for the phonon specific

heat, and the higher order contributions are negligibly small.

The Schottky contribution to the specific heat can have various sources. Extrinsic residual paramagnetic centers (electronic Schottky effect) in the sample or intrinsic electronic and nuclear moments are some of the possible sources for this contribution to the specific heat [61]. However, all Schottky contributions have similar field and temperature dependencies but on a different scale; i.e. the nuclear Schottky contribution is usually at lower temperature than electronic Schottky contribution but the two have the same temperature dependence, shown in Fig. 1.8. The paramagnetic centers usually act like two-level spin systems (S=1/2). This type of contribution has been identified in many cuprates and is strongly sample dependent (due to the different density of paramagnetic centers). The contribution of these two-level spin systems to the specific heat is given by [61]:

$$C_{Sch} = \frac{Nx^2e^x}{(1+e^x)^2}, \qquad x = \frac{g\mu_B H}{k_B T}, \tag{1.6}$$

where N is the density of the paramagnetic centers, μ_B is the Bohr magneton, and H is the effective field on these paramagnetic centers. The Schottky contribution becomes effective when the thermal energy, k_BT, becomes comparable to the level spacing of the magnetic system, $g\mu_BH$. This contribution goes to zero when $k_BT \gg \mu_BH$ since both of the spin levels would be equally populated, and there would be only a few transitions between them. It also goes to zero when $k_BT \ll \mu_BH$ since only the level with the lower energy would be populated (see Fig. 1.8). In the intermediate temperatures there would be transitions between these levels and hence a significant contribution to the specific heat. Therefore the Schottky contribution shows up as a hump in the C vs T at constant H, or C vs H at constant T (only the temperature dependence is shown in Fig. 1.8, but the field dependence looks the same as temperature dependence). For the electronic Schottky effect the peak of this hump usually occurs around 1-2 K, and in most experiments the high temperature tail of this contribution is observed at the measurements above 2 K. This high

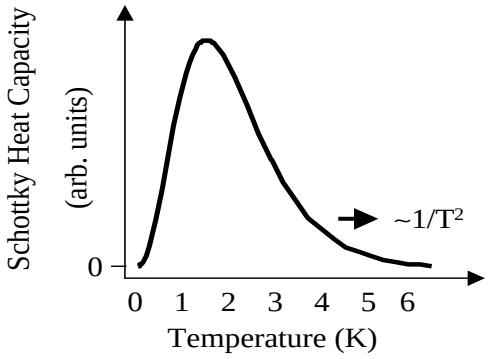

Figure 1.8: Temperature dependence (at a constant field) of a typical Schottky heat capacity [61].

temperature tail shows a $1/T^2$ type temperature dependence. The nuclear Schottky effect has a peak below 1K (see Fig. 3.8 for an example of nuclear Schottky effect in a PCCO crystal). For a detailed discussion of the Schottky heat capacity see Ref. [61].

One last contribution to the specific heat in cuprates is a zero-field residual specific heat that has a linear temperature dependence $\gamma(0)T$. The origin of this contribution is not known, however there have been several suggestions: a band of normal state-like excitations within the nodal regions of the gap created by impurity scattering [45], gapless superconductivity [62], or contributions from non-superconducting regions in the sample [63]. However, none of these explanations has been experimentally proven and has attained broad acceptance yet. This residual specific heat is highly sample dependent and its magnitude has gradually decreased as the sample quality improved, however, even in the highest quality samples it has not gone below 1 mJ/mole-K^2. It has also been observed that the magnitude of this contribution significantly decreases in YBCO upon detwinning and upon oxygenation [64]. Since twins and oxygen vacancies act as scattering centers, this observation was interpreted as a connection between impurity scattering and the zero field residual

specific heat [45].

1.3 Pseudogap and the Nernst effect

Gap symmetry is an important ingredient of any model attempting to explain the mechanism of high temperature superconductivity, however in the last several years the normal state properties as a precursor to the superconductivity have become the focus of research in the cuprates. These efforts have resulted in the discovery of a pseudogap in the normal state. The origin of pseudogap and its connection with the superconducting gap are some of most intensively studied topics of current research in the cuprates [65].

One of the possible explanations of the pseudogap is superconducting fluctuations above the transition temperature. Superconducting fluctuations in their simplest form are due to small regions of normal material becoming superconducting by releasing some of their thermal energy to their vicinity (for reviews of superconducting fluctuations in conventional superconductors see Ref. [66, 67, 68, 69] and for superconducting fluctuations in cuprates see Ref. [70, 71, 72, 73, 74]). For this to be possible the temperature should be close to the transition temperature, and the limit for closeness is set by the energy required to create Cooper pairs. Since the superconducting region can not be smaller than the size of a Cooper pair (ξ, the coherence length), the minimum required energy to create a superconducting fluctuation is proportional to ξ^2, the area of the region becoming superconducting (2D fluctuations are considered). The coherence length of the cuprates is in turn very small, usually two orders of magnitude smaller than in the conventional superconductors. In addition, the transition temperature T_c is much higher in the cuprates which makes fluctuations in the thermal energy larger. For a comparison of the fluctuation regime in the conventional superconductors and high temperature superconductors see Ref. [70]. Therefore, it is much easier to create superconducting

fluctuations in cuprates compared to the conventional superconductors, and hence the superconducting fluctuations occur over a much broader temperature region in cuprates compared to conventional superconductors.

One of the sensitive probes of superconducting fluctuations is the Nernst effect. The Nernst effect is a thermomagnetic effect, in which a transverse potential difference is induced in the presence of a longitudinal thermal gradient and a perpendicular magnetic field [75]. The sensitivity of the Nernst effect is due to the negligibly small Nernst effect of normal carriers and the relatively large vortex Nernst signal characteristic of the mixed state in a superconductor [76]. Therefore, at temperatures above T_c and in the presence of a large enough magnetic field, the superconducting fluctuations would have vortices in them, and hence would have a much larger Nernst effect compared to the normal part of the material. In the early years of high-T_c superconductivity this large Nernst signal was used to determine the fluctuation region in the cuprates. For example, in optimally-doped YBCO for example a Nernst signal due to superconducting fluctuations was observed at temperatures as high as 10K above T_c [77, 78, 79]. However, most of the prior Nernst effect studies were made on the optimally-doped compounds.

Recent Nernst effect measurements [80, 81, 82, 83] on hole-doped cuprates have shown very surprising results. Especially in the under-doped regime of these cuprates, an anomalous Nernst signal has been observed to persist to temperatures up to 50-100 K above T_c, and to magnetic fields much larger than the resistive H_{c2} (see Fig. 4.2 and Section 4.3 for a more detailed discussion of this anomalous Nernst effect). The authors have interpreted this anomalous signal above the conventional T_c or H_{c2} (the T_c or H_{c2} of resistivity and magnetization) as evidence for vortex-like excitations above T_c or H_{c2}. The onset temperature of the anomalous Nernst effect, T_ν, has been defined as the onset of Cooper pair formation. In this picture there is a temperature (or field) at which the Cooper pairs start to form, and another temperature(or field) below which the Cooper pairs attain phase coherence throughout

the sample. Therefore, the T_c (or H_{c2}) of resistivity measurements corresponds to the temperature (or field) that coherence has been obtained, whereas the onset of the anomalous Nernst signal corresponds to the temperature (or field) of the Cooper pair formation. This qualitatively agrees with the phase fluctuation model proposed for HTSC [84].

The onset temperature of this anomalous Nernst effect increases as the doping is reduced, which is analogous to the doping dependence of the onset temperature of the pseudogap, T^*, in these compounds (see Fig. 4.2). However, T_ν is significantly less than T^*. In addition unlike T^* which continues to increase as the doping is reduced (T^* continues to increase down to x≈0.03 in LSCO), T_ν peaks at a certain doping (for example the peak of T_ν is at x≈0.1 for LSCO) [81]. T_ν goes to zero at the lowest doping that superconductivity is observed (see Fig. 9 in Ref. [81]). The similarity between the doping dependence of the pseudogap onset temperature T^* and the onset temperature of anomalous Nernst signal T_ν has been proposed as evidence for a relation between the phase fluctuations and the pseudogap. However, the difference in the magnitude of T_ν and T^* clearly rules out the possibility of the pseudogap being due to phase fluctuations. For an extensive review on the pseudogap see Ref. [65].

Electron-doped cuprates have shown two different pseudogaps. Tunnelling spectroscopy experiments have shown a low energy gap comparable in size to superconducting gap when the superconducting state is suppressed with magnetic field [85, 37]. On the other hand optical conductivity ($T^* > 292$ K [86] to T^*=110 K [87]), photoemission [88], and Raman spectroscopy [89] (T^*=220 K) experiments have shown evidence for a high energy gap similar to the pseudogap in the hole-doped cuprates. Since the previous Nernst effect studies of the electron-doped cuprates concentrated on temperatures below T_c or at temperatures much higher than T_c, we decided to study the Nernst effect of the electron-doped cuprates on an extended temperature, field, and doping range with the question of pseudogap and the extent

of the superconducting fluctuations in mind. In this chapter a brief introduction will be made to the Nernst effect in normal metals, superconductors, and in a metal with two bands of conduction with carriers of different sign. A detailed description of the Nernst effect using Boltzmann transport theory is given in Appendix-A. A report of our Nernst effect data and its implications is given in Chapter 4.

1.4 The Nernst effect

As mentioned before the Nernst effect is a thermomagnetic effect, in which a transverse potential difference is induced in the presence of a longitudinal thermal gradient and a perpendicular magnetic field. In a normal metal the charge carriers moving along a thermal gradient accumulate on the cold side of the sample and they induce an electric field opposing the thermal force. This electric field in turn induces an electric current in the opposite direction to the thermal current. In steady state these two currents are equal in magnitude and opposite in sign, so that J_x=0(assuming the thermal gradient is in the $\hat{\mathbf{x}}$ direction). In the presence of a magnetic field along $\hat{\mathbf{z}}$ direction, the carriers moving in $+\hat{\mathbf{x}}$ and $-\hat{\mathbf{x}}$ directions will be deflected to opposite sides along the y-axis. In the simplest case of a spherical Fermi surface and one type of carrier, these two currents will be equal to each other, and no transverse voltage will be induced. However, in general the two currents will not cancel out exactly because of the energy dependence of the scattering time [90] (the significance of the energy dependence of the scattering time will become more clear at the end of this section). In order to satisfy the boundary condition of J_y=0 (since it is an open circuit), a transverse potential has to be induced, which is the Nernst voltage. The Nernst effect is usually defined in terms of the transverse electric field, E_y, instead of the transverse voltage V_y in order to eliminate the geometry dependence. In this thesis the Nernst effect is presented in terms of the the quantity $e_y = E_y/|\partial_x T|$. The standard way of representing the Nernst effect in metals is by

the Nernst coefficient, Q, which is $Q = e_y/H$. Using Q instead of e_y does not cause any confusion for a normal metal due to the linear magnetic field dependence of the transverse electric field (Lorentz force gives $q\mathbf{E} = -\mathbf{v} \times \mathbf{B}$). However in the mixed state of a superconductor the field dependence of the Nernst effect is not linear, and hence a linear scaling with the magnetic does not have any meaning. In order to keep a consistent notation in the normal and superconducting states, **the Nernst effect is represented with e_y rather than Q, and e_y is referred to as the Nernst signal.**

The Nernst effect measurements were made on thin film PCCO samples. In order to establish a temperature gradient, the sample is attached on one-side to a thermal sink, and on the other side it is free (like a diving board). A small heater is attached on the free side of the sample, and two thermometers are attached on the hot and cold side of the sample in order to monitor the temperature gradient. The transverse voltage (the Nernst voltage) is measured by a voltmeter with nanovolt sensitivity (Keithley 2182). For a schematic of the setup see Fig. 1.9.

1.5 Nernst effect in superconductors

For superconductors the thermomagnetic effects have a different mechanism. In the Meissner state at T=0 the superconducting condensate has a uniform entropy, and there are no single charge carriers like electrons or holes. Therefore, applying a thermal gradient does not induce any flow. For T>0 there are quasiparticles which experience a thermal force and a pinning force. In the case of thermal force overcoming the pinning force these quasiparticles flow along the thermal gradient. In the mixed state there are vortices and flux lines that carry additional entropy compared to the superconducting condensate around them. Vortices also experience a pinning force, $\mathbf{f}_p$, which prevents them from flowing. In the case of an applied thermal gradient, the flux lines carrying a transport entropy per unit length of $\mathbf{S}_\phi$

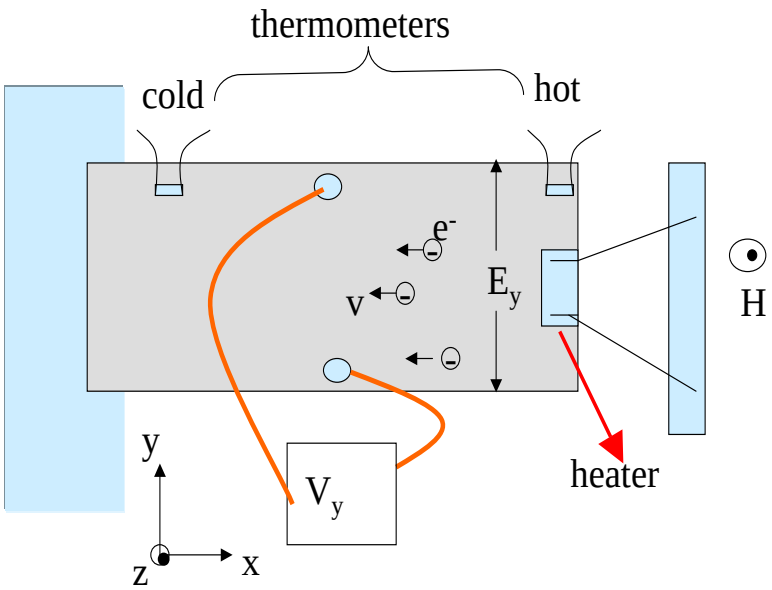

Figure 1.9: Schematic diagram of the Nernst effect measurement technique.

experience a thermal force per unit length of:

$$\vec{f}_{th} = -S_\phi \vec{\nabla} T \tag{1.7}$$

In the absence of pinning this force induces a vortex flow, with velocity $\mathbf{v}_\phi$, opposite to the thermal gradient. This in turn causes dissipation and balances the thermal force:

$$\eta \vec{v}_\phi = -S_\phi \vec{\nabla} T, \tag{1.8}$$

where η is the damping coefficient. This vortex flow induces a transverse electric field $q\vec{E} = -\vec{v}_\phi \times \vec{B}$ [91]. If there is pinning, the viscous flow of vortices is observed when the thermal gradient and the magnetic field are large enough for the thermal force to overcome the pinning force. This flow can be represented by:

$$\eta \vec{v}_\phi = -(\vec{f}_p + S_\phi \vec{\nabla} T) \tag{1.9}$$

Unlike the single carrier Nernst effect, the vortex Nernst effect is not small, and it is the dominant thermomagnetic effect in the superconducting state. The vortex

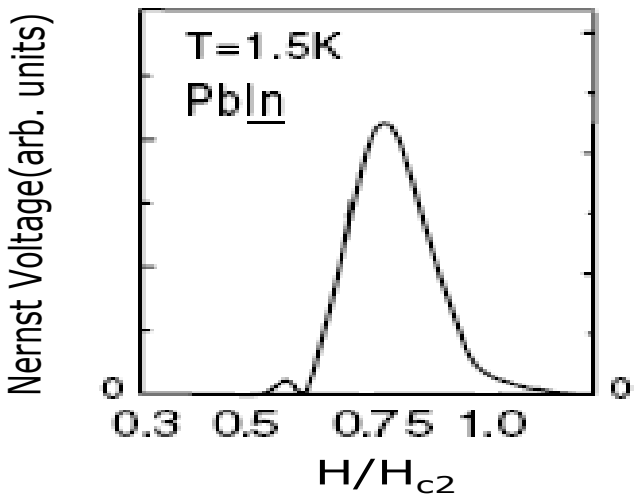

Figure 1.10: The Nernst effect of a conventional low-T_c superconductor PbIn as a function of magnetic field. The large peak is the vortex-Nernst peak which diminishes very quickly to zero above H_{c2}. The small peak is not related to our discussion in this thesis. The figure is from Ref. [92].

Nernst effect has a very different magnetic field dependence than the linear field dependence of the normal state Nernst effect. The vortex Nernst effect is zero until a certain depinning field in which the vortex lattice transforms to a vortex liquid and vortices become mobile. With increasing field both the number of vortices and their mobility increases, and hence the vortex Nernst signal. Above a certain field the vortex Nernst signal starts to decrease since the mobility of the vortices decreases due to enhanced vortex-vortex interactions and this dominates the increase in their number. Therefore the vortex Nernst signal peaks at a certain field and decreases afterwards, reaching zero at a field close to H_{c2} (see Fig. 1.10 for Nernst effect on a conventional superconductor PbIn). It is in principle easy to separate the vortex Nernst signal and the normal state Nernst signal because of this very different field dependence and also because of the large difference between the magnitude of these signals.

Chapter 2

Samples and Experimental Setup

2.1 Sample preparation

The specific heat measurements were made on single crystals of PCCO, whereas the Nernst effect measurements were made on thin film samples. The details of the crystal growth and sample characterization can be found in original papers written by our group [93], therefore only a summary of crystal growth and some details regarding the crystal annealing are given here. However, considerable time and effort were spent by the author on crystal growth since having high-quality, well-characterized crystals was crucial for the experiments to be described later. In particular growing high-quality crystals large enough for specific heat measurements was one of the major contributions of this work. Another contribution of the author in terms of crystal growth was to grow over-doped PCCO crystals. The original crystal growth work on PCCO had concentrated on the optimally-doped compound, and there were no over-doped crystals. Single crystal PCCO of x=0.16 and x=0.17 concentration have been grown and made superconducting as a result of our work. In addition to growing crystals with CeO_2 as the cerium source, as was used by our group in the past, crystals using a new cerium source, $(NH_4)_2Ce(NO_3)_6$, have been grown (the advantages of this cerium source are discussed below).

Single crystals of PCCO are grown using a high temperature directional solidifi-

cation technique. In this technique a CuO flux is mixed with the reaction powders in a ceramic crucible and placed in a furnace. The mixture is heated above the melting point of CuO and the reaction powders form a uniform mixture in liquid CuO environment. A temperature gradient is created across the crucible when the furnace temperature is slowly reduced since the the lower parts of the crucible cool faster than the upper parts (the heating filaments are on the top side of the furnace). Crystal growth starts when the furnace temperature reduces below the melting point of the mixture.

Before the crystal growth is started, the powders that will be used are dried (in air) to remove any water vapor they might have. This is done to get the weight of the powders more accurately. Pr_6O_{11} is dried at 950 ^{o}C for 12 hours, and $(NH_4)_2Ce(NO_3)_6$ is dried at 110 ^{o}C for 2-3 hours. Then the powders are weighed in the correct amounts and a solid-state mixture of Pr_6O_{11}, CeO_2 or $(NH_4)_2Ce(NO_3)_6$, and CuO powders is prepared. If $(NH_4)_2Ce(NO_3)_6$ is used for Ce, the mixture is stirred in acetone for about 45 minutes in order to dissolve and separate the ammonium from cerium oxide, and obtain smaller particle size for cerium oxide. Smaller particle size is important in order to get a better mixture, and hence more homogeneous samples. If CeO_2 is used as the cerium source then a solid state mix is enough. Usually better mixtures of powders are obtained by stirring them in a ball-milling machine for several hours.

Next the mixtures are filled into a crucible. Whichever size crucible one uses it is important to have the crucible around 80-90 % full. This is because molten flux creeps out of the crucible and a significant portion of it is lost. Therefore it is important to have some material left behind that will form the crystals. The initial work on different crucibles (Al_2O_3, ZrO_2, and Pt) showed that all crucibles were corroded to a certain extent from the melt at high temperatures. The Al_2O_3 crucibles were the least corroded and therefore Al_2O_3 crucibles were preferred for the crystal growth.

The high melting temperature of the powders require the inclusion of the flux which reduces the melting point of the compound. The amount of CuO used in the starting material is chosen to be 4 to 6 times more than the amount needed by just calculating from the chemical formula. The melting temperature of the compound decreases as the amount of CuO powder in the mixture is increased and the melting point of the compound can be changed between 1100^{o}C to 1500^{o}C. In the particular case of the most common growth conditions used in our group the growth temperature when 4 times the amount of CuO in the composition of PCCO is used as flux is roughly 100 K above the growth temperature when 6 times the amount of CuO in the composition of PCCO is used as the flux.

The most frequently used crucible is the Al_2O_3 crucible from Coors ceramic company (CH50, catalog number 65504). The crucible volume is enough to hold 80-85 grams of PCCO mixture. Therefore roughly 70 grams of mixture is usually used for a single growth. The initial studies on NCCO crystals [93] showed that in order to get x=0.15 of Ce in $Nd_{2-x}Ce_xCuO_4$ the initial mixture $Nd_{2-y}Ce_yCuO_4$ should have y=0.08 of Ce and hence 2-y=1.92 of Nd. This is due to the different solubilities of Nd and Ce in CuO. Similar ratios between the starting composition and the end composition are also valid for PCCO. Considering all these issues a typical growth of PCCO x=0.15 has the following amounts of starting material in the mixture: 40.00±0.01 grams CuO , 27.11±0.01 grams Pr_6O_{11}, 1.44±0.01 grams CeO_2.

In order to have a good thermal contact between the crucible and the furnace, the crucible is inserted in a high-temperature brick, carved in a way as to cover the crucible except at the top-most 1/3 of the crucible. This is also important to protect the bottom of the furnace from the creeping flux. Also a lid of the same high temperature brick is placed on top of the crucible cap to prevent the cap from falling when the flux creeps out (see Fig. 2.1). This lid protects the mixture from impurities that might fall from the top of the oven. However this lid should not be

Figure 2.1: The crucible and the high temperature bricks for crystal growth.

too heavy, since in that case the extra flux would not be able to creep out, and it might stick to the surface of the crystals. This would require mechanical cleaning of the crystal surface from this flux after the growth. In a typical growth the crystal surfaces have a small amount of this flux, and better crystals are mostly clean of this flux.

The crystals grow in platelet-like structures. The growth starts when the temperature is slowly decreased after the mixture is soaked about an hour at the highest temperature. The slow cool down introduces a temperature gradient across the mixture and the growth happens from bottom up as the temperature reduces below the melting point. This gradient is important in order to have a slow and uniform crystal growth. However, the magnitude of the temperature gradient established across the mixture also depends on the position of the crucible in the furnace. Usually the position of the crucible is off center, and in the particular case of Lindberg Type

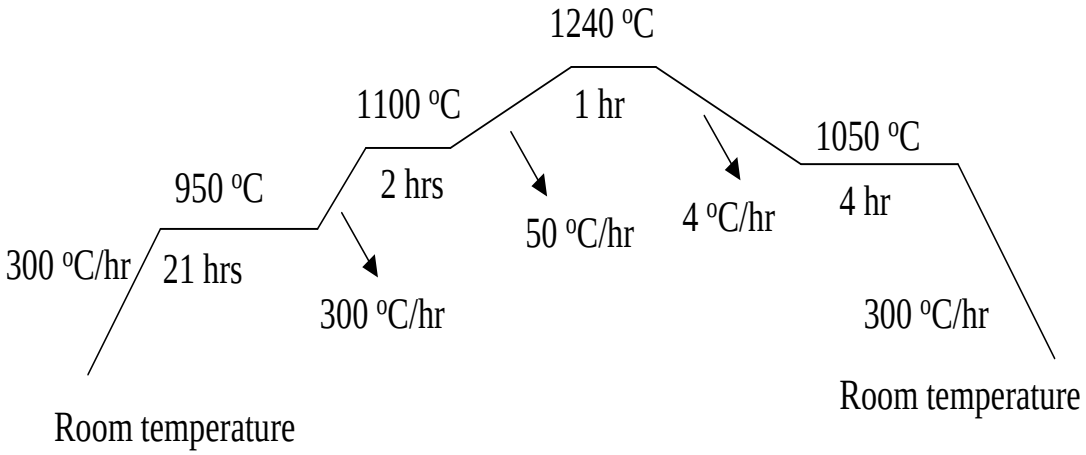

Figure 2.2: A typical crystal growth sequence.

51333 furnace(furnace with a maximum temperature of 1500^{o}C) used in our group, the crucible is placed 12.5 cm from the front and 2.5 cm from the left side of the furnace. The best crystal growth occurs when a gradient of 20 K/cm is established across the mixture. To get such a gradient a cool down of 4-5 K/hr is required. A typical growth (in air) follows the procedure shown in Fig. 2.2. This procedure follows previous work and was developed empirically.

After the crystals are grown big crystals at the top surface are picked up with tweezers. Otherwise the crucible is broken in order to make extraction of the crystals easier. After the crystals are selected they must be annealed in order to make them superconducting. The annealing reduces the oxygen content of the crystals. The as grown crystals are semiconducting, and reducing the oxygen content changes the carrier density.

Due to the difficulty of removing oxygen from the T' structure of PCCO (see

Fig. 1.3), the annealing (reduction) is made at quite high temperatures (850 ^{o}C-900 ^{o}C), and a very slow flow of argon gas (or any other inert gas) is maintained. The best annealing results were accomplished by the following sequence: warm up from room temperature to 900 ^{o}C at 5 ^{o}C/min, anneal the crystals at 900 ^{o}C for 48 hours, cool down to 700 ^{o}C at 1.8 ^{o}C/min, and then a natural cool down to room temperature (usually at 5 ^{o}C/min). Depending on the thickness of the crystals the annealing time could be more than 48 hours. This is because of the longer time needed for the oxygen to diffuse through the crystal. The diffusion constant of oxygen in PCCO has not been measured, therefore we are not able to say if 48 hours is enough time to anneal a thick crystal (thickness >30 μm). However no significant difference in T_c or ΔT_chas been observed at longer annealing times even for crystals as thick as 50-60 μm. Crystals thicker than this need to be annealed between 5-8 days at 900 ^{o}C. Magnetization measurements (using a Quantum Design SQUID magnetometer) have shown that crystals thicker than 30 μm tend to have broader superconducting transitions. This is an indication that oxygen is not uniformly reduced for these thick crystals. Since specific heat measurements usually require thick crystals (larger mass), considerable effort was devoted to getting as uniform a reduction as possible even for thick crystals.

As mentioned before, the annealing furnace has to be sealed to air. However this is not very easy at such high temperatures. Even though a continuous flow of argon is maintained, there will still be some air, and therefore some oxygen, leaking into the system. In order to further reduce this oxygen a small amount of titanium is kept in a separate alumina boat next to the sample boat. Titanium is very reactive with oxygen, and it has a high tendency to form TiO_2 at such high temperatures. Therefore, Ti acts like an oxygen sink (getter). Because of such harsh conditions of annealing, the crystals have to be protected from the non-uniform annealing that could result from the top surface of a crystal being closer to Ti, or rapidly changing oxygen partial pressure around the crystal. This is accomplished by placing the

crystals between two PCCO pellets, and also by covering these pellets with PCCO powder [94]. After the annealing procedure is over, usually the top layer of the PCCO powder is seen to be heavily reduced and it changes color. The color of this layer becomes brownish, unlike the bottom layers which are still black, similar to the original powder before the annealing is made.

Thermogravimetric analysis (TGA) has shown that the oxygen starts to leave the sample at 770 ^{o}C. Therefore, the annealing temperature should be at least 770 ^{o}C. However, since the reduction would be very slow at this temperature usually higher temperatures are used. On the other hand, the temperature should not be very high either, because of two important reasons: crystal dephasing and Cu and Ce ion migration from the crystal surface. The phase stability temperature of electron-doped cuprates decreases as the partial oxygen pressure increases [95]. Therefore, it is very important to seal the furnace very well, and minimize the amount of air leaking into it.

As discussed later, X-ray measurements show that the crystals are single phase. However, prior wavelength dispersive spectroscopy (WDX) measurements have shown that the crystal surface becomes Cu deficient after the oxygen reduction if the annealing time is too long or temperature is too high. Crystals annealed under the conditions outlined in this section do not have these problems.

2.2 Preparation of polycrystallane samples

As mentioned above, the powders are dried before they are weighed. Pr_6O_{11} is dried at 950 ^{o}C for 12 hours and $(NH_4)_2Ce(NO_3)_6$ is dried at 110 ^{o}C for 2-3 hours. Unlike the single crystal growth every oxide is added in the same proportion as in the final product, i.e. for an optimally doped polycrystal Pr is 1.85, Ce 0.15, and Cu 1 in the starting mixture. For example if a pulsed laser deposition (PLD) target is prepared the following amounts are used:

12.60±0.01 grams of Pr_6O_{11}

3.29±0.01 grams of $(NH_4)_2Ce(NO_3)_6$,

3.18±0.01 grams of CuO.

The weighed amounts of the oxides are put in an agate mortar, and 25 ml of acetone is added to the mixture. If CeO_2 is used as the Ce source then a solid state mixture with ball-milling machine is enough, and no mixing with acetone is necessary. The acetone and powder mixture are stirred slowly until the acetone evaporates. In order to get a better mixture usually another 25 ml of acetone is added, and the mixture is again stirred until the acetone dries. This mixture, after it dries completely, could then be mixed in the ball milling machine for several hours if the amount of material is large enough (larger than about 30 grams).

After this mixing procedure the powders are transferred to the alumina crucibles. The first heating of the mixture is made at 900 ^{o}C for 24 hours. Since temperature gradients are not desirable for polycrystal sample growth, the powders are placed in the center of the furnace where the temperature is supposed to be more uniform. The temperature is ramped up at 100 ^{o}C/hr, and the cool down is at 300 ^{o}C/hr.

After the temperature cools down to room temperature, the powders are usually hardened to a solid piece. This solid piece is grounded as finely as possible. Then the mixture is heated up to 1050 ^{o}C with a ramp up rate of 300 ^{o}C/hr, and cool down rate of 300 ^{o}C/hr. The mixture is kept at 1050 ^{o}C for 24 hours.

After the material cools down, it is usually even harder than it was after the first heating. This solid piece is again grounded very finely. It is very important at this stage to get the powder as fine and as uniform as possible, otherwise it is inevitable that the polycrystalline sample or the target made out of this powder would crack. After the grinding the fine powder is pressed into pellets. The pressing is made at 20-25 ktons, and the sample is kept at this pressure for a few minutes. Once the pressure drops down to 10 ktons or so the pressure is increased to 20 ktons again and kept there for a few minutes. This procedure is repeated at least three times.

These pellets are then sintered at 1100 ^{o}C for 24 hours. Both the ramp up rate and the cool down rate are 300 ^{o}C/hr. In order to make the as grown samples superconducting the samples should be annealed at 900 ^{o}C for 4-10 hours in argon flow with a ramp up rate of 300 ^{o}C/hr, and cool down rate of 100 ^{o}C/hr. If the samples are pulsed laser deposition targets no annealing is necessary.

These procedures, both for single crystal growth and polycrystalline sample preparation, have been developed empirically. Different procedures have been tested and the conditions described in this section are the conditions that produced the best samples.

2.3 Characterizing the samples

There are certain measurements that must be done before a sample can be used in any of the experiments discussed in this research. Depending on the type of the sample, the characterization techniques that are used vary. In the first years of electron-doped cuprate crystal growth in our group, extensive studies have been made to characterize the samples. For a complete account of these studies see Ref [93]. However some of these measurements have been repeated for the crystals that were used in our experiments, and therefore we will summarize these experiments.

For a single crystal, the first check made before the sample is used in any experiment is to measure magnetization vs temperature of the sample with a SQUID magnetometer (see Fig. 2.3). As is well known superconductors have a strong diamagnetic signal at $T < T_c$, and above T_c there is a weak paramagnetic signal. This measurement is a quick and non-destructive way of determining T_c and ΔT_c. In case of a thin-film sample, the T_c and ΔT_c are determined by measuring the ac-susceptibility of the sample. It is usually the imaginary part of the ac-susceptibility that determines these parameters. The imaginary part of ac-susceptibility shows a

peak during the normal-to-superconducting transition. The mid-point of this peak is the T_c and the full-width at half maximum determines ΔT_c. The magnetization measurements can in principle be used to calculate the volume fraction of superconductivity. Dividing the saturation value of the magnetic moment to the volume of the sample and the magnetic field should result in -1/4π for a sample that is 100% superconducting. The volume of the sample can be accurately calculated as follows: multiplying the number of moles (mass/molecular weight) of the sample by Avogadro's number (6.02×10^{23}) results in the number of unit cells our sample contains, and multiplying this number of unit cells with the volume of a unit cell results in the volume of our sample. However, certain conditions have to be satisfied in order to obtain a reliable estimate for the volume fraction of superconductivity in the sample. The sample should be cooled in zero field, even a few Oersted of magnetic field trapped in the magnet could change the saturation magnetization significantly (for PCCO the magnetization of a sample field-cooled at 5 Oe can be 10-20 % that of the zero-field cooled magnetization of the same sample). In addition the field in the magnet should be known accurately, i.e. having 5 Oe instead of 4 Oe in the magnet would result in 25 % error in the volume fraction of superconductivity. The sample should be placed such that the demagnetization factor would be minimal, and small enough magnetic fields should be applied such that only a negligible portion of the superconducting sample becomes normal because of the applied field.

X-ray diffraction is used to check whether any dephasing has occurred during the growth or the annealing of the crystals. Both powder samples and single crystals are studied using a Siemens four-circle x-ray machine. In the case of single crystals the sample is aligned using the most prominent peak along the 001 direction, the 006 peak. Data for a typical PCCO x=0.15 single crystal is shown in Fig. 2.4. The absence of any extra peaks shows that the sample has a single-phase.

Another technique used in sample characterization is wavelength dispersive x-ray spectroscopy (both WDX and WDS are used in the literature). WDS is a technique

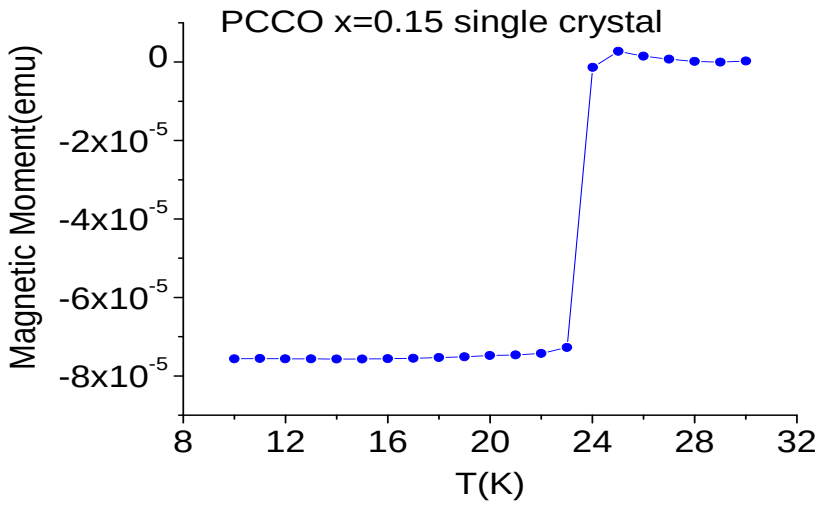

Figure 2.3: Magnetization vs temperature of an optimally doped PCCO single crystal measured at H= 1 Oe.

used to determine the concentration of each element in the sample (for a general discussion of this technique see Ref. [96]). It works best for elements heavier than oxygen. In our case this technique is mainly used to determine the cerium doping and doping uniformity of the crystals. Both WDS and EDS require a clean surface for accurate measurements. The measurements were made in a JEOL JXA-8900 superProbe machine. This machine has up to 5 wavelength dispersive spectrometers and an energy dispersive spectrometer (EDS). WDS rather than EDS has been used in our measurements because of the necessity of high resolution required to differentiate between Ce and Pr. Due to the close proximity of the energy level spacings of Pr and Ce (K_α and K_β energies), the resolution of EDS is not enough to differentiate between them (the resolution of EDS is 150 eV compared to 5 eV of WDS). Another advantage of WDS over EDS is the low detection limit (0.01 wt % in WDS compared to 0.1-1.0 wt % in EDS). However, EDS also has its advantages like fast qualitative analysis that could check for any type of impurity in the samples, such as Al impurities from the crucibles.

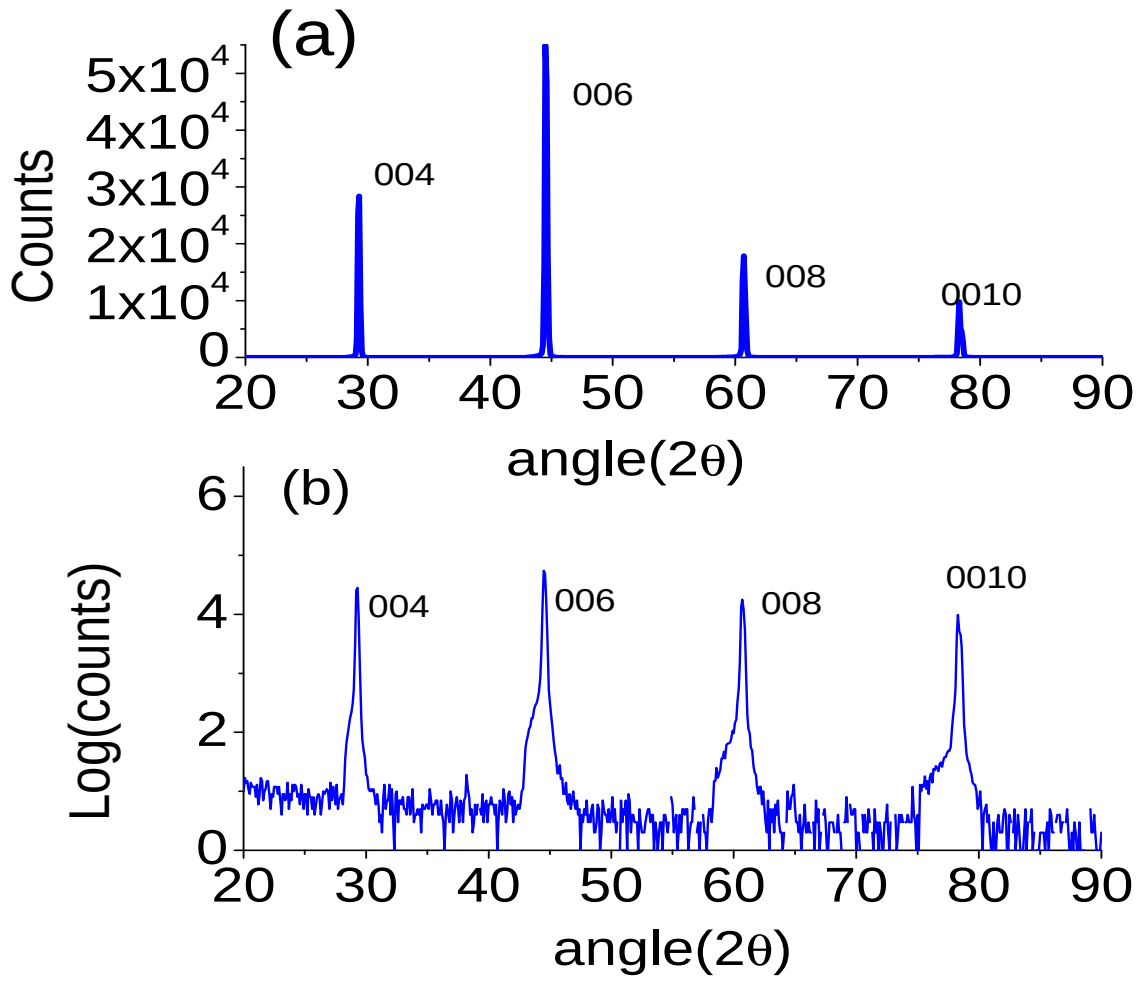

Figure 2.4: X-ray spectroscopy of an optimally doped PCCO single crystal on (a)-normal, (b)-logarithmic scale. The absence of any unaccounted peaks shows that the crystal is single phase.

The beam diameter in our WDS measurements was 2 μm (but the beam actually expands while penetrating the sample) and the acceleration voltage was 15 kV. The beam penetrates about 5 μm into the sample and an average concentration of approximately 50 μm^3 of a volume of the sample is obtained. Due to the narrow beam diameter both the uniformity in the ab-plane and along the c-axis could be studied. Our measurements have shown that the cerium concentration changed by 3-5 % between randomly selected points in the ab-plane for the optimally-doped and over-doped crystals. However, the variation of cerium concentration along the c-axis for thick crystals (thickness>30μm) has been measured to be larger [97, 93]. For most of our work we use crystals less than 30 μm thick which have uniform cerium concentration. For optimum doping different crystals of any batch have Ce concentrations that varied between $0.145 - 0.155$. In addition using Pr_2CuO_4 as the standard for Pr, and $CePO_4$ as the standard for Ce produced the most reliable results in terms of Ce concentration.

Another point that should be mentioned about the WDS measurements is the sample preparation when Ce concentration along the c-axis is measured. Due to the size of the crystals along the c-axis (10-30 μm), it is not easy to make sure that the crystals will not move when they are hit by high energy electron beam (the crystals have to sit on their thin side in order to study the c-axis uniformity). In particular if the crystals are fixed by just a conducting tape, they would vibrate when they are hit by the electron beam since the tape holding the crystal would melt. Therefore, the crystals were inserted in a low viscosity epoxy (from Buehler, resin part number 20-8140-032 and hardener part number 20-8142-016) and then the epoxy was polished so that the surface of the crystal would be exposed to the electron beam. Using low viscosity epoxy is important to assure that the epoxy would diffuse thoroughly around the crystal. The polishing was made with diamond polishing compound of various particle sizes changing from 6 μm to 0.25 μm again from Buehler(part number 40-6249 for 6 μm, part number 40-6246 for 3 μm, part

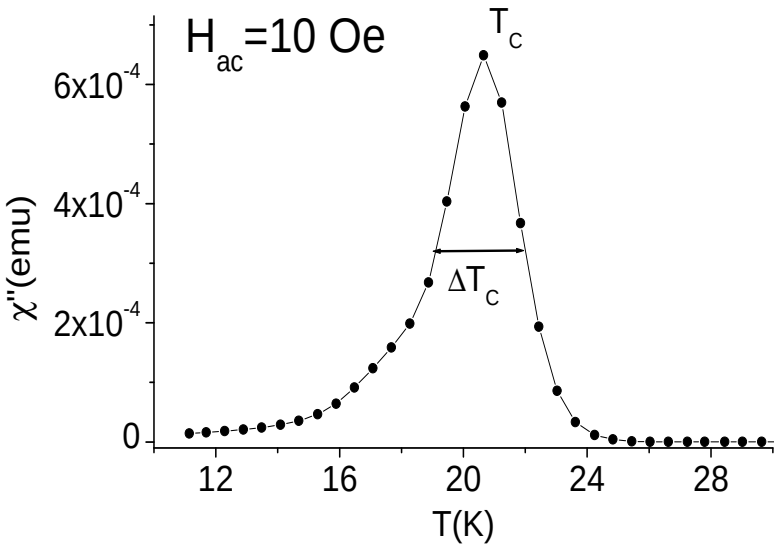

Figure 2.5: ac susceptibility vs temperature for a PCCO x=0.15 crystal.

number 40-6122 for 1 μm and 40-6102 for 0.25 μm). The polishing cloth was also from Buehler (part number 40-7112).

Ac susceptibility is another non-destructive technique used to characterize the single crystal samples. Susceptibility, χ, is defined as the derivative of the magnetization with respect to the applied magnetic field: χ=dM/dH, where M is magnetization and H is the applied magnetic field. Depending on the type of the applied magnetic field the susceptibility is called ac or dc susceptibility. At very low frequencies samples in general have similar responses to the ac and dc magnetic fields. However, at higher frequencies usually there is a phase difference, ϕ, between response of the sample (in terms of magnetic moment) and the phase of the applied ac magnetic field. This is mainly due to dynamic effects in the sample. Hence, the ac susceptibility in general is defined to have two components to represent this phase difference between the sample moment and the applied field: the in phase component $\chi' = \chi cos(\phi)$ and the out of phase component $\chi'' = \chi sin(\phi)$. At low

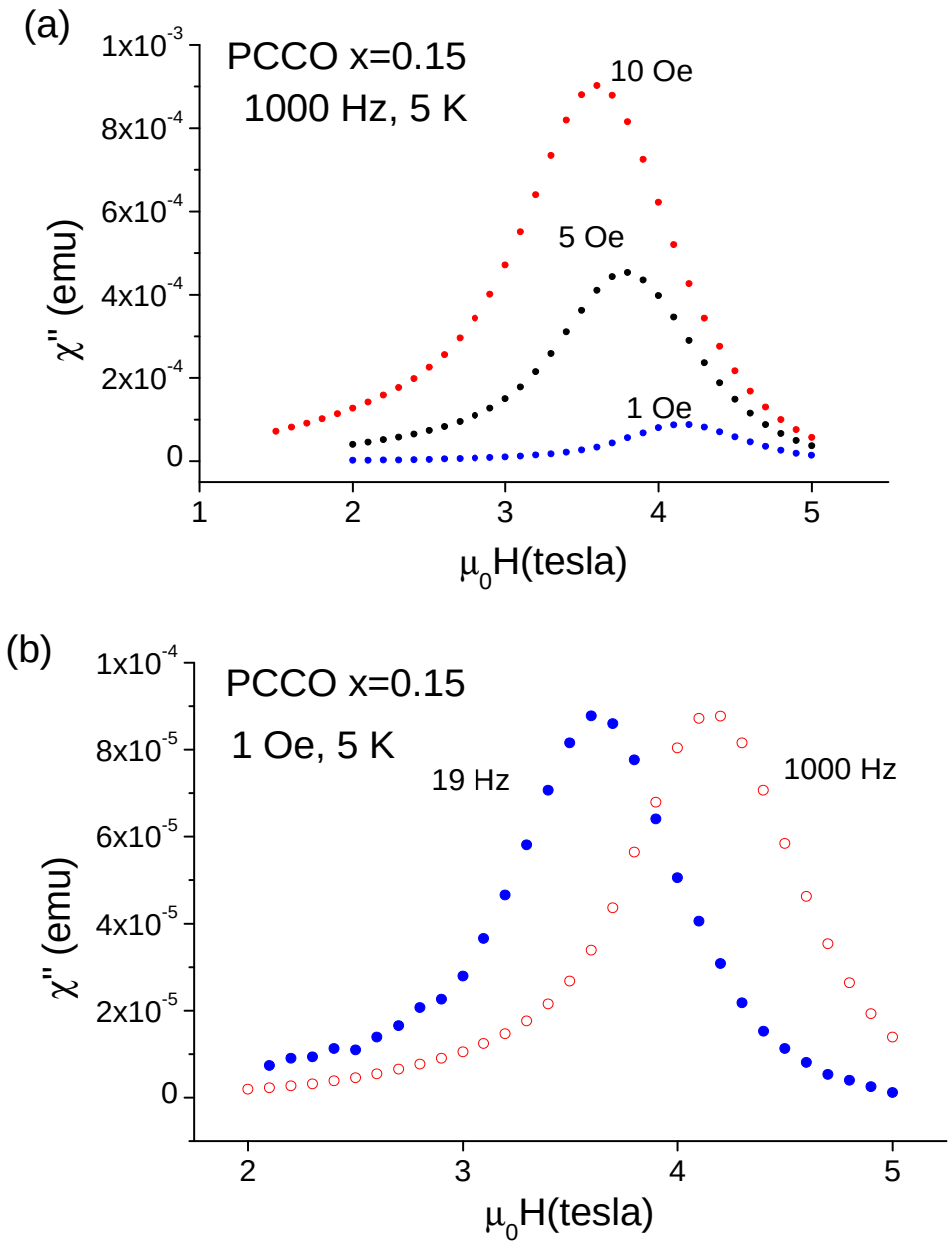

Figure 2.6: (a) ac susceptibility vs field at different ac field amplitude (b) ac susceptibility vs field at different frequencies for a PCCO x=0.15 crystal.

frequencies χ' is basically equal to χ and it is the slope of the M-H curve. A non-zero χ'' is an indicative of dissipative processes in the sample [98].

In the case of superconductors χ' $\approx$0 in the normal state and χ' $\approx$-1 in the superconducting state (since superconductors are perfect diamagnets). χ'' becomes non-zero slightly below the superconducting transition temperature since the applied ac field creates vortices in the superconducting sample, which in turn cause dissipation. The dissipation depends on the number of vortices and their mobility [76]. The mobility of vortices is high close to T_c, and at lower temperatures the vortices get pinned, hence their mobility is reduced. Therefore a peak like structure is observed in χ''.

The dependence of ac susceptibility on the frequency and magnitude of the applied ac magnetic field has been used to extract a wealth of information including the critical temperature, the irreversibility line [98], the critical current [99], and the nature of superconductivity in the weak links between the grains of granular superconductors [100].

In our case χ'' is just used to determine T_c and ΔT_c of our crystals. A Quantum Design PPMS ac susceptibility probe is used to study the crystals and a home-made ac susceptibility setup is used to study the thin films. The midpoint of χ'' is taken as the T_c and the FWHM of this peak is taken as ΔT_c (see Fig. 2.5). However one should be careful when using this technique since the results of the measurements strongly depend on the frequency and amplitude of the ac signal used for the measurements. In particular the amplitude of the ac signal should be kept as small as possible for most accurate results. See Fig. 2.6 for the dependence of H_{c2} on frequency and amplitude (the T_c also has a similar dependence). The location of the peak reduces to lower temperatures (fields) when the amplitude of the signal is increased, since at higher amplitudes the pinning becomes effective at lower temperatures (fields). The frequency dependence is also due to a similar mechanism. The peak in χ'' appears when the applied ac field fully penetrates the sample as the vortices move from the

boundaries of the sample towards the center of the sample. As the frequency of the applied field is increased less time is available for the vortices reach the center, and hence a weaker pinning is enough to prevent the vortices from reaching the center of the sample. Hence higher transition temperatures are observed at higher frequencies [101, 102]

Resistivity was rarely used to characterize the single crystal samples in this work since the crystals used for resistivity measurements are usually not usable for any other measurement (due to the electrical contacts on the crystal). Therefore, it is generally the last experiment done on a crystal for characterization purposes. All the thin film samples on the other hand were characterized by measuring their resistivity prior to the Nernst effect measurements. Four electrical contacts are placed on the crystal or the thin film sample for this measurement. The outer two contacts are used for current contacts and the inner two are used for the voltage contacts. In the case of crystal samples it is important to connect the current contacts to the side of the crystal in order to get a uniform current distribution. Silver paint is used for the contacts on the crystals (Leitsilber 200 silver paint from TedPella Inc, part number 16035). The contacts have to be annealed at 500 C for about 1 hour in order to get contact resistance of about 1 Ω. The contacts on the thin film samples on the other hand are soldered on them (Ag-In is used to make the contacts).

Both c-axis and ab-plane resistivity have been studied for the optimally-doped and over-doped crystals (see Fig. 2.8 for a typical c-axis resistivity of an optimally doped crystal) and ab-plane resistivity has been used to characterize the thin film samples (see Fig. 2.7). For characterization purposes there are several parameters that are important to check in order to get an idea about the quality of a sample. The first two are obviously the T_c and ΔT_c. In addition the value of the residual resistivity before the sample goes through the superconducting transition is an important parameter. This resistivity shows the impurity concentration in the sample, and the smaller it is the better. An optimally doped sample with less than 30 $\mu\Omega$-

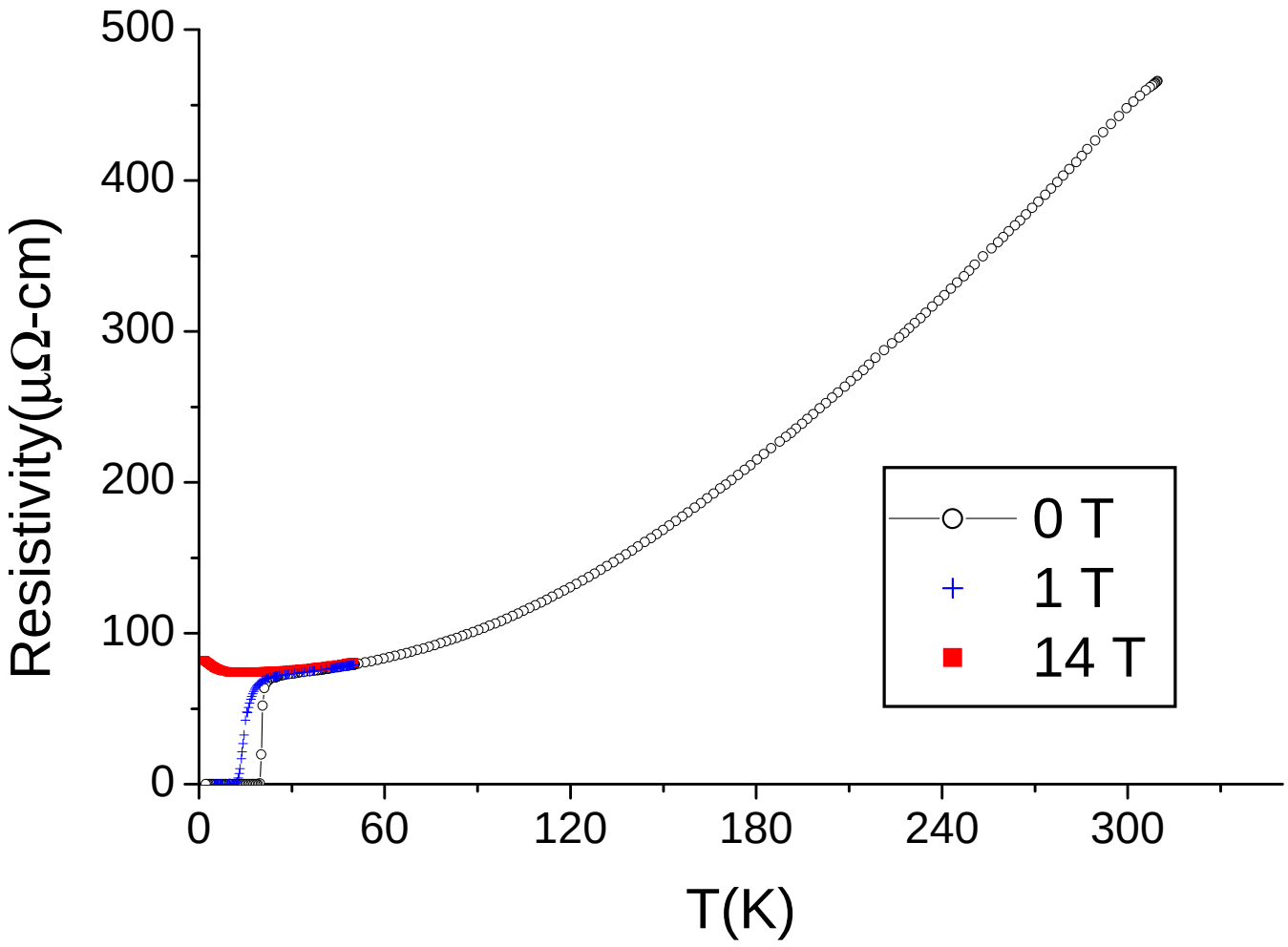

Figure 2.7: ab-plane resistivity of a PCCO x=0.15 thin film.

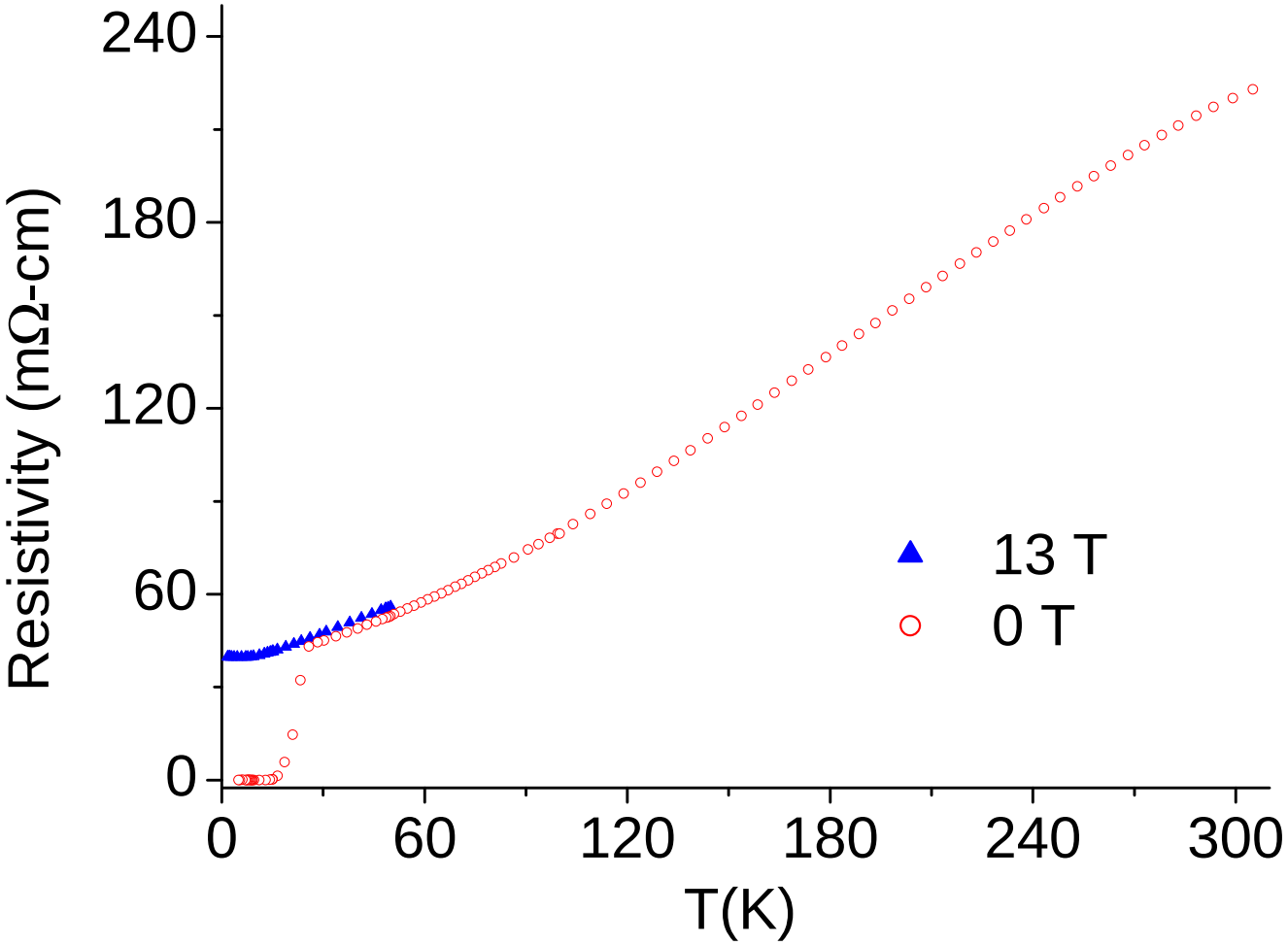

Figure 2.8: c-axis resistivity of a PCCO x=0.15 single crystal.

cm residual resistivity can be considered a good sample, which suggests that the thin film shown in Fig. 2.7 is a typical sample rather than a good sample. Another parameter to check is the ratio of the room temperature resistivity to the residual resistivity. This ratio gives an idea about how successfully the annealing has been done. An annealing procedure resulting in a ratio of 5-6 is considered be a successful annealing.

2.4 Experimental apparatus

Two systems were used for the experiments reported in this thesis: an Oxford Research cryostat with a home-made probe and related electronics and a Quantum Design Physical Property Measurement System (PPMS).

The Oxford cryostat has a 9T superconducting magnet, in which the magnetic field could be increased up to 11T by pumping on the lambda plate. This system does not have a nitrogen jacket, instead the liquid helium bath is isolated from the environment by vacuum jackets and a super insulation layer. Cooling below 4.2K is achieved by collecting liquid helium into the variable temperature insert and reducing the pressure on it by pumping with a mechanical pump. The probe for this system is home-made, and small changes on the probe design have been made by the author in order to reduce the thermal load on the sample by better thermalizing the wires before they make contact with the sample and also by establishing better thermal contact of the sample with the cold parts of the probe. In addition, the wiring of the probe has been modified in order to reduce the cross-talk between the wires by passing the wires through grounded stainless steel tubing. The temperature of the probe is monitored by a Lakeshore cernox thermometer (cx-1050) and controlled by a Lakeshore temperature controller (93-CA). Keithley 2182 and 182 nanovoltmeters, and Keithley 220 and 224 current sources are used for the various experiments performed in this system.

The other system used was the Quantum Design Physical Property Measurement System (PPMS). Fig. 2.9 shows the sample holder and the sample space for this system (the pictures are from the Quantum Design's PPMS brochure). The system has multiple thermometers and heaters to monitor and control the temperature. There are two thermometers at the bottom of the probe close to the sample, and one thermometer in the top region of the probe close to the neck. The temperature is monitored by a platinum thermometer above 80 K and by a Lakeshore cernox-1050 thermometer below 100 K. These thermometers are at the bottom of the probe close to the sample puck connections. The average of the two thermometers is used in the crossover region 80 K - 100 K. The thermometer close to the neck of the probe (Lakeshore cernox 1080) is used to monitor the thermal gradients along the probe. Unlike most home-made cryostats, the PPMS has a cooling annulus around the sample space. This annulus is the active region of temperature control. The cooling of the sample space is achieved by continuously drawing helium gas through the annulus by pumping on it with a mechanical pump. The sample puck is in contact with this annulus and also the sample space is kept at a pressure of a few torr in order to have thermal contact with the cold walls of the sample space (except when high vacuum is necessary).

This design, continuous low temperature control (CLTC), has some advantages over the conventional method of temperature control, but also some disadvantages. In order to cool down the sample below 4.2 K it is not necessary to fill the sample space with helium and pump on it. This is important since helium goes through two phase transitions at 4.2 K and 2.2 K, and these phase transitions could make temperature control difficult around these temperatures. In a CLTC system these phase transitions are avoided by not letting "liquid" helium into the cooling annulus (by passing it through a highly restricted impedance tube).

Another advantage of this method of temperature control is that, in principle, temperatures below 4.2 K can be maintained indefinitely. In a system where the

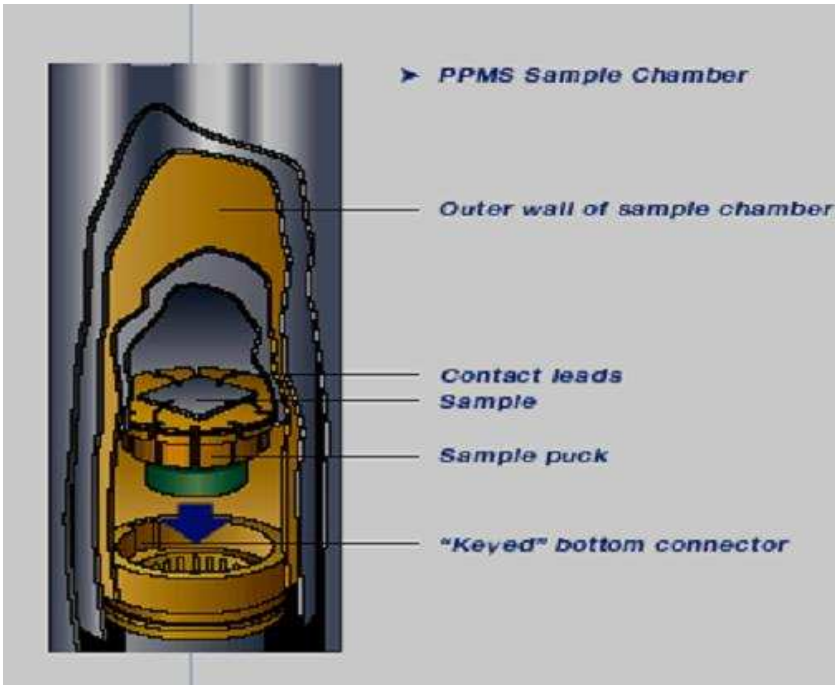

Figure 2.9: Picture of PPMS sample puck and connector. Different measurements have different pucks but the connections are the same. The picture is from Quantum Design Online PPMS Catalog.

cooling below 4.2 K is achieved by pumping on a liquid helium collected in the sample space, it is usually necessary to refill with liquid helium every hour or so. If longer times are necessary one needs to refill the pot and pump on it again. However, in the PPMS CLTC method since no liquid helium is collected in the annulus there is no such a limit on the time the system could stay below 4.2 K.

Helium condensation on the sample is sometimes a problem for the PPMS (see Quantum Design web-site for an example). In order to minimize this condensation problem, it is important to pump out all the exchange gas in the sample space before cooling down, preferably around or above 300 K. In addition, there is a charcoal bar provided with the system which should be inserted before every measurement that is performed in high vacuum. The charcoal bar is placed close to the sample, and acts as a helium sink.

Particularly for samples of a few mg mass and hence small heat capacity it is essential to use a backing pump in addition to the PPMS turbo pump. Otherwise helium accumulation on the sample around 4.2K gives rise to superfluous effects on the data, like humps around 4.2K. These humps can extend from 3.5K to 5.5K where helium is absorbed if the sample is cooled down or desorbed if it is warmed up, hence hysteresis like features appear between warming up and cooling down of the sample. Such features are completely eliminated if the PPMS Varian turbo pump is backed up by another mechanical pump-turbo pump assembly.

Even when the PPMS turbo pump is backed up by another turbo pump, there could be a small helium accumulation if the sample is kept below 4.2 K for several hours. In that case, the sample should be heated up to 20-30 K and cooled back down. As a final alternative if the problem is still not solved, the system should be taken up to room temperature and cooled back down. In some cases it might be necessary to heat the charcoal bar to several hundred degree Celsius in order to recharge it. However, we did not encounter any helium condensation problems after we backed up the PPMS turbo pump with another turbo pump.

More details regarding the experimental techniques will be given in Chapter 3 and Chapter 4.

Chapter 3

Specific Heat of $Pr_{2-x}Ce_xCuO_4$

This chapter is a review of our specific heat measurements on optimally-doped and over-doped PCCO crystals. In addition to the superconducting state, the specific heat of the normal state (before annealing) is also measured, and the effects of annealing on the bulk properties are studied. Before presenting our data different methods of measuring specific heat are explained, and a brief introduction is made to the dirty d-wave symmetry which was not discussed in Chapter 1.

3.1 Different methods of measuring specific heat

The most common techniques used to measure heat capacity are adiabatic calorimetry [103], thermal relaxation calorimetry [104], and ac thermal relaxation [105]. In all the methods that are described in this section the specific heat at a constant pressure is measured, and this specific heat will be represented by C instead of the more frequently used C_P. The simplest of these methods is adiabatic calorimetry, in which a pulse of heat, ΔQ is applied to a thermally isolated sample, and the temperature rise is monitored. The heat capacity is just the ratio of the heat applied to the temperature rise:

$$C = \Delta Q/\Delta T \quad as \quad \Delta T \rightarrow 0. \tag{3.1}$$

In adiabatic calorimetry it is very important to thermally isolate the sample from the environment, but have some electrical link between the sample and the environment so that the temperature can be monitored. However, this is not easy to achieve for small samples of a few milligram mass. Instead relaxation calorimetry and ac temperature calorimetry are the preferred methods for this type of small samples.

It was shown in 1968 by Sullivan and Seidel [105] that if an ac current of frequency $\frac{w}{2}$ is passed through a heater attached to a sample, both of which are weakly linked to a constant temperature heat bath, the temperature of the stage which includes the sample and the addenda (the components of the measuring stage other than the sample are called addenda and the addenda includes a thermometer, a heater, wires, and thermal grease) in turn oscillates around a temperature slightly above the bath temperature with a frequency w and amplitude T_{ac} given by:

$$T_{ac} = \frac{P}{2wC}(1 + \frac{1}{(w\tau_1)^2} + (w\tau_2)^2 + const)^{1/2}, \tag{3.2}$$

where P is the power applied to the heater, τ_1 is the sample to bath relaxation time, τ_2 is the thermal response time of the sample and the addenda to the applied heat, and C is the total heat capacity of the sample and the addenda. If the internal thermal response of the sample and addenda, τ_2, is much shorter than $1/w$ ($\tau_2 \ll 1/w$), and if the sample to bath relaxation, τ_1, is much longer than $1/w$ ($\tau_1 \gg 1/w$) the oscillation in the temperature can be reduced to:

$$\begin{aligned} T_{ac} &= \frac{P}{2wC}(1 + const)^{1/2} \\ \Rightarrow C &= \frac{P}{2wT_{ac}}(1 + const)^{1/2}, \end{aligned} \tag{3.3}$$

where the constant is $2\mathrm{K}_b/3\mathrm{K}_s$, K_b is the sample to bath thermal conductance and K_s is the sample thermal conductance. If $\mathrm{K}_b \ll \mathrm{K}_s$ then the heat capacity is just $C = \frac{P}{2wT_{ac}}$.

The main advantage of ac calorimetry is that it provides the capability of measuring very small changes in the heat capacity by using the sensitivity of a lock-in-

amplifier to detect small oscillations in the temperature. T_{ac} of the size of a few millikelvins is detectable with this method.

In order to satisfy the conditions $1/w \gg \tau_2$, small samples with good internal thermal conductivity are needed, and also low-frequencies are used in the measurement. The other condition, $\tau_1 \gg 1/w$, requires a lower bound to the frequency. In the ac heat capacity measurements usually frequencies of the order of f=$w/2\pi \approx$1Hz are used. Today many of the ac heat capacity apparatus use a laser or a diode in order to heat the sample. Even though this method reduces the addenda by eliminating the heater, it introduces an uncertainty in determining the amount of power applied to the sample. There is also a minor error that could come from neglecting $2K_b/3K_s$ in Eq. 3.3. Due to such problems, it is not easy to measure the absolute value of the heat capacity in this method. Therefore, this technique is most frequently used for measuring physical phenomena like phase transitions in which the change in the specific heat is more important than its absolute value. For a general review of the ac calorimetry techniques see Ref. [106].

The other method used for measuring the heat capacity of small samples is thermal relaxation calorimetry. The setup is the same as for ac calorimetry but a dc power is used to heat the sample. When the power is removed the temperature of the sample relaxes to the reservoir temperature exponentially, and the heat capacity of the sample is given by $C = k \times \tau_1$, where τ_1 is the relaxation time constant and k is the thermal conductance of the weak link between the sample and the reservoir. Since the heat capacity is determined through the relaxation time of an exponential decay rather than oscillations in temperature as in ac temperature calorimetry, τ_1 is the important time scale rather than $1/w$. The requirement of having temperature uniformity at time scales less than $1/w$, which is required in the ac calorimetry, is not essential anymore. The important time scale is rather the relaxation time to the environment, and the internal time constants should be much less than this time scale. This property makes thermal relaxation calorimetry particularly useful, compared

to ac calorimetry, for polycrystalline samples which might have relatively poor internal thermal conductance. Thermal relaxation calorimetry is often preferred over ac temperature calorimetry for small samples since it is possible to determine the absolute value of the heat capacity.

We used thermal relaxation calorimetry in our measurements. The sample is linked to an external heat reservoir through a weak thermal link which in our case is a Au-7%Cu wire (see Fig. 3.1). The temperature of the sample is raised above the temperature of the heat reservoir by passing current through a heater that is part of the addenda. The temperature change of the sample is monitored during warm up and cool down. By measuring the temperature many times during the relaxation process, a relaxation time constant can be found.

Now we will summarize the relaxation method using heat flow equations. The applied power creates a temperature gradient across the thermal link, and raises the temperature of the sample by $\Delta T = T_s - T_0$:

$$P(t) = k\Delta T + C(T)\frac{\partial \Delta T}{\partial t}, \tag{3.4}$$

where k is the total thermal conductance of the four wires. After steady state is reached, i.e. a constant ΔT is established, the applied power will only create a temperature gradient across the wires,

$$P(t) = k\Delta T. \tag{3.5}$$

Using this relation the thermal conductance of the wires can be measured. If the power is turned off after the steady state is reached the heat transfer equation becomes:

$$\frac{\partial \Delta T}{\partial t} = -\frac{k\Delta T}{C(T)}. \tag{3.6}$$

Therefore the sample temperature relaxes exponentially to the base temperature and the time constant for this relaxation is given by $\tau = \frac{C}{k}$. By measuring the thermal relaxation time constant τ, and the thermal conductance of the weak link

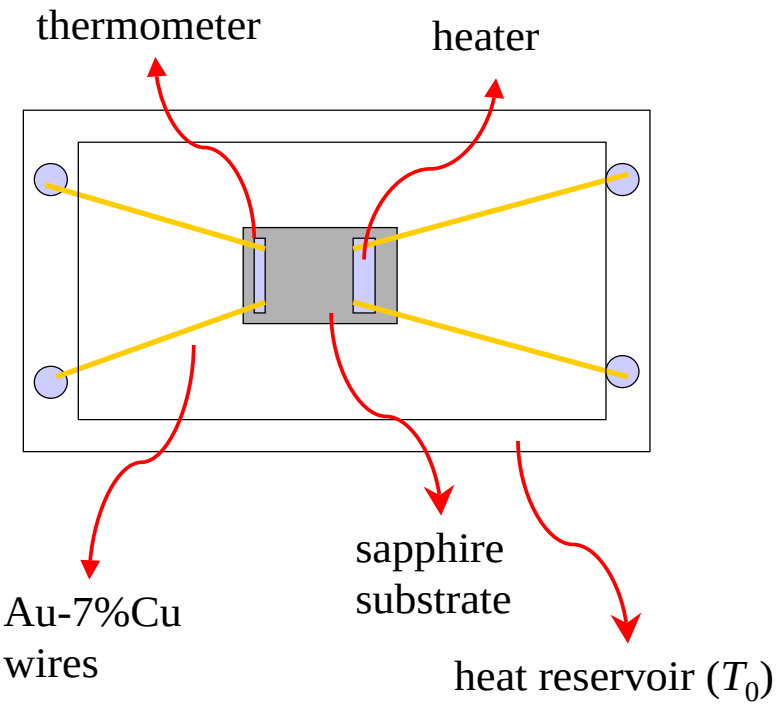

Figure 3.1: Schematic diagram of the specific heat setup. The four Au-7%Cu wires (each of length 6 mm) which are electrically connected to the thermometer and heater also act as a weak thermal link between the sample and the heat reservoir. The diameter of the wires varied between 1-3 mil.

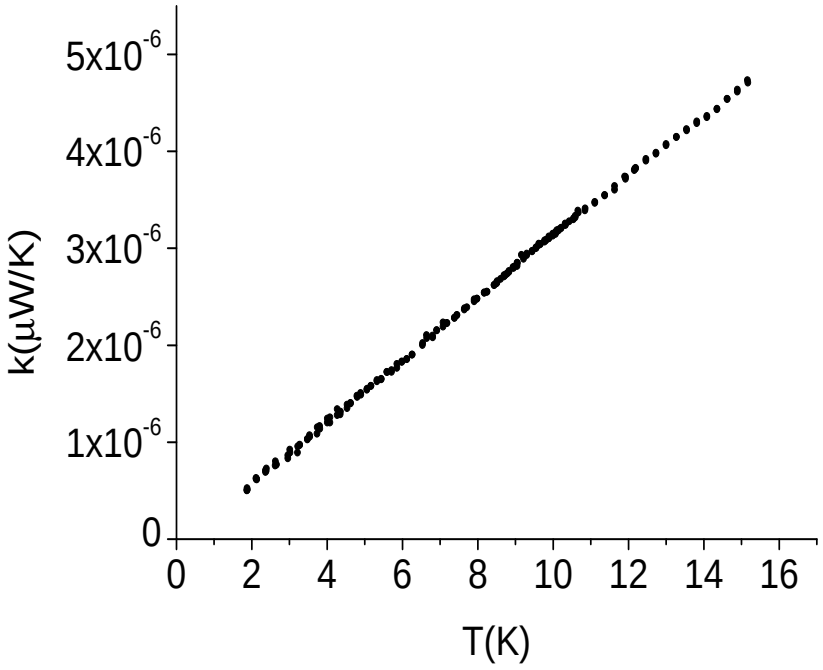

Figure 3.2: Total thermal conductance of four Au-7%Cu wires with 1 mil diameter. The length of each wire is approximately 6 mm.

the heat capacity of the sample can be found. However, the thermal conductance of the weak link is temperature dependent and it has to be characterized (for some wires it could also be magnetic field dependent). In our case the the weak link is a Au-7%Cu wire and the thermal conductance of the wire is measured at every field and temperature that the sample specific heat is measured (see Fig. 3.2 for typical thermal conductance of the 1 mil thick Au-7%Cu wires).

It is important to have good thermal contact between the sample and the addenda and to have all the internal relaxation times related to the addenda and the sample to be much less than the relaxation time to the heat reservoir. When this condition is not satisfied there will be two relaxations instead of one, and a fit consisting of two time constants, two-τ, should be used instead of one time constant. In our setup every data point is fitted to a two-τ type relaxation, and we make sure

that the second relaxation time constant is small enough to be neglected. For a review of the two-τ effect see Ref. [107].

3.2 Experimental setup

A home-made specific heat apparatus was used for some of the early measurements. However, soon it was realized that the Quantum Design PPMS could be improved to measure smaller samples down to lower temperatures. Therefore, a QD PPMS commercial chip was modified to enable measurement of smaller samples and to avoid the magnetic field dependence of the polycrystalline alumina substrate which is part of the commercial chip.

We have built several chips suitable for use at different temperature ranges and different sample masses. The chip that was used for the smallest samples($\sim$ 1 mg mass) consists of a 3mm $\times$ 3mm $\times$ 0.125 mm single crystal sapphire piece, a specially thinned cernox 1030 thermometer (substrate thickness approximately 0.130 mm), a NiCr thin film heater (resistance about 100 Ω), and four 1 mil diameter Au-7%Cu wires each of approximately 6 mm length. The chips designed for heavier samples had thicker wires (3 mils) and a regular Cernox 1030 bare chip thermometer. A very thin layer of GE 7031 varnish has been used to attach the thermometer to the substrate. Wakefield thermal compound or Apiezon N grease have been used to attach the sample to the sapphire substrate.

It is important to know the heat capacity of the addenda accurately, since what is measured when the sample is mounted is the total heat capacity of the addenda and the sample. Therefore, before measuring each sample the addenda (including the grease used to attach the sample) heat capacity is measured and this heat capacity is subtracted from the total heat capacity (sample plus addenda). It is essential to minimize the addenda heat capacity in order to minimize the inaccuracy of the sample heat capacity. Therefore, every component on our setup is a miniature

version of what is used in commercial setups.

There is a problem in minimizing the addenda too much. When the addenda is made small, the relaxation time (τ) of the addenda becomes very short at low temperatures. The relaxation time constant of the addenda should be at least an order of magnitude larger than the fastest possible sampling rate of the temperature in order to be able to make a reasonably good exponential decay fit to the relaxation data. The easiest way to solve this problem is to make the thermal link between the chip and the reservoir weak enough to get long relaxation times, yet short enough to be able to take data in reasonable times. Therefore, usually alloys of good metals are used as weak links. For example, Au-7%Cu wire has a thermal conductivity roughly two orders of magnitude smaller than pure Au wire around 4 K. By reducing the diameter of these wires the relaxation times can be significantly increased. It has been shown [104] that roughly one-third of the wire is also part of the addenda. Therefore, it is clear that using as thin a wire as possible is very important, especially for measuring small samples. The PPMS uses an ADC card that can read data every 2.5 ms, and the smallest time constants we get at 2 K are around 200 ms when 1 mil Au-7%Cu wire is used as the thermal link. For a typical relaxation time data of 2 mg PCCO sample see the Fig. 3.3.

Another important issue is the magnetic field dependence of the addenda. There could be field dependence in the addenda because of magnetic impurities in the components of the heat capacity chip. If the addenda and the sample have comparable heat capacities, then any field dependence in the addenda could be significant and this has to be taken into account. Therefore, it is very important to use single crystal substrates with high purity when a chip is prepared for specific heat measurements. Our heat capacity setup does not have a field dependence within the resolution of our measurements (see Fig. 3.4).

One last point regarding our specific heat setup is the magnetoresistance of the thermometers on the chip. If the field dependence of the sample heat capacity is

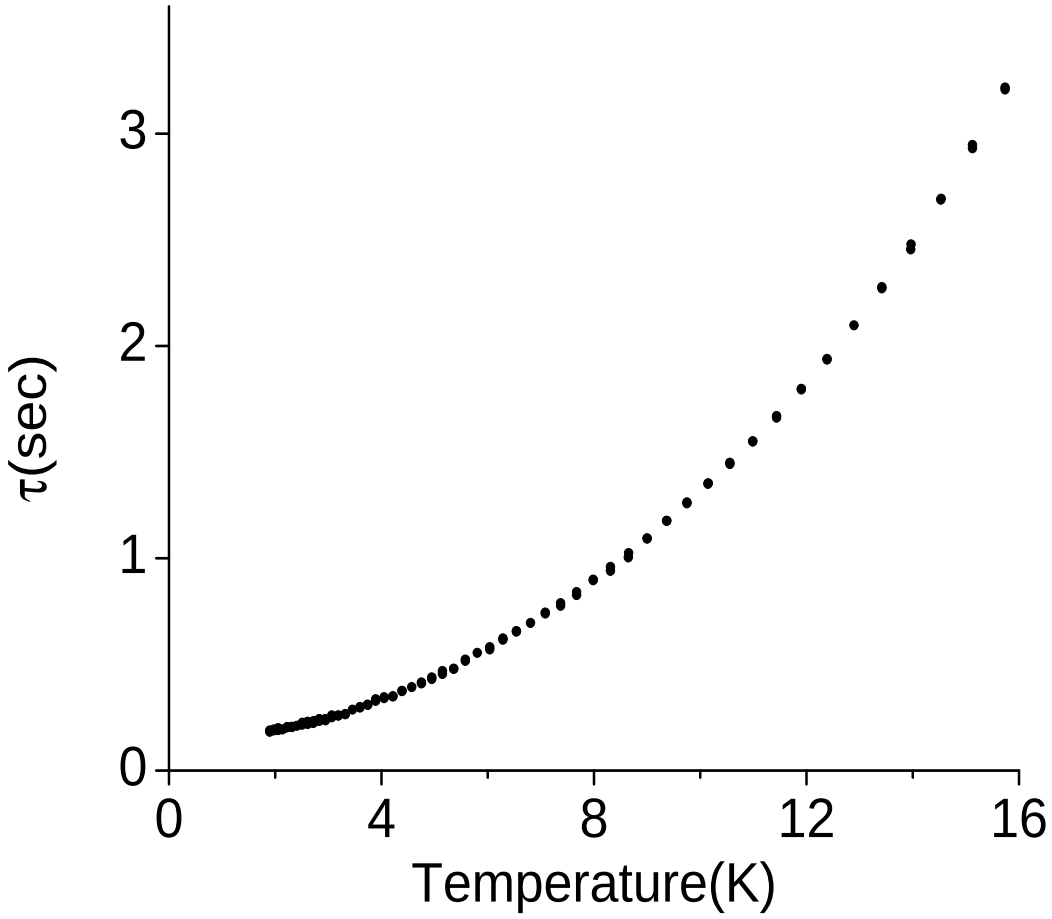

Figure 3.3: Typical relaxation time of a 2 mg PCCO crystal using 1 mil diameter Au-7%Cu wires.

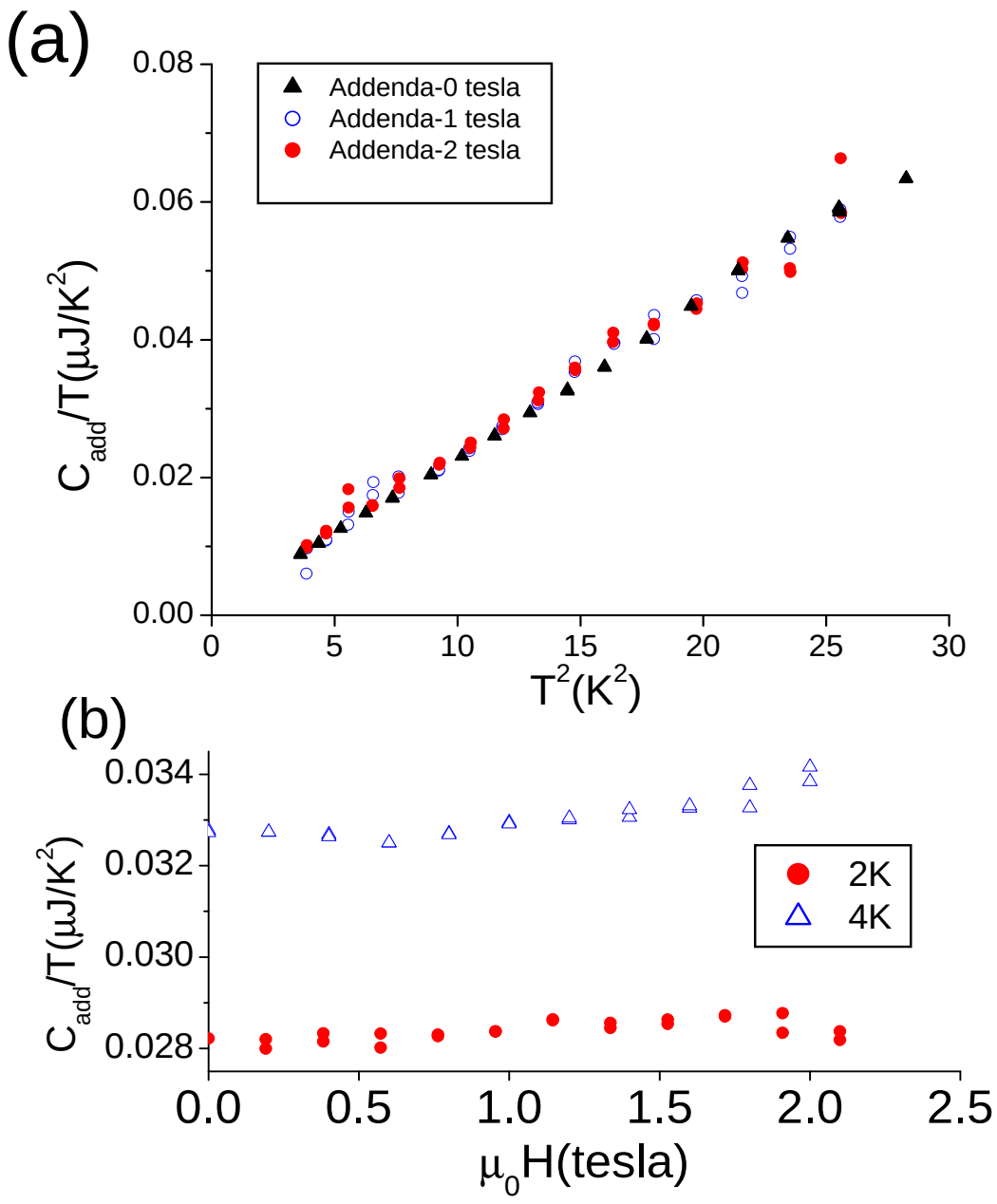

Figure 3.4: (a) C/T vs T^2 for the addenda at 0, 1, 2 T magnetic field, (b) addenda heat capacity vs field at 2 K and 4 K. The 4 K data and the 2 K are from different addenda measurements (they have different amounts of thermal grease). The 4K data is from the same addenda measurement shown in (a).

important, it is essential to have a consistent temperature at different magnetic fields. The magnetoresistance of the Lakeshore cernox thermometers is known to be small even at fields as high as 20 tesla. At 2 K the resistance at 10 tesla is usually a few percent more than that of the zero field resistance. The most important magnetic field range in our measurements is between 0-2T, and our chip thermometers are calibrated every 0.5 T in this field range, and every 2 T between 2-12 T. The PPMS software has an option of calibrating the thermometers automatically at the desired field. For the home-made system the calibration is made by measuring the resistance of the thermometers between 2-20 K with respect to a commercially calibrated cernox thermometer. The temperature range between 2-20 K is divided into three regions. Each region overlaps with the other one across a temperature interval of approximately 1 K to make sure that there is no kink in the fit. Then each region is fitted with a Chebychev polynomial of order 9: $T = \sum_{i=0}^{9} A_i \cos(i \arccos x)$ where $x = \frac{\lg(R)}{\lg(R_{max})-\lg(R_{min})} - \frac{\lg(R_{max})+\lg(R_{min})}{\lg(R_{max})-\lg(R_{min})}$, R is the value of the thermometer resistance, R_{max} is the largest value of the resistance in the region, and R_{min} is the smallest value of the resistance in the region.

As a final test of our setup the specific heat of a conventional superconductor (niobium), and of a high purity copper piece has been measured. A copper sample of 3 mg mass and 99.999 % purity has been measured down to 2 K, and compared to the standard data from the CRC Handbook. The comparison is shown in Fig. 3.5. The two data are consistent within 5 percent, however there seem to be a slight systematic deviation between the two curves. The reason for this may be a purity difference between our sample and the sample of the standard data, or a small change in the thermometer calibration which affects the higher temperature data more seriously (since the sensitivity of the thermometers decreases as the temperature is increased).

The Nb wire that was measured had a mass of 3.2 mg (see Fig. 3.6). Nb has an upper critical field, $H_{c2} \approx 4000$ Oe, and a critical temperature $T_c \approx 9.2$ K. Fig. 3.6 shows the downward shift of the T_c with magnetic field, and the vanishing of the

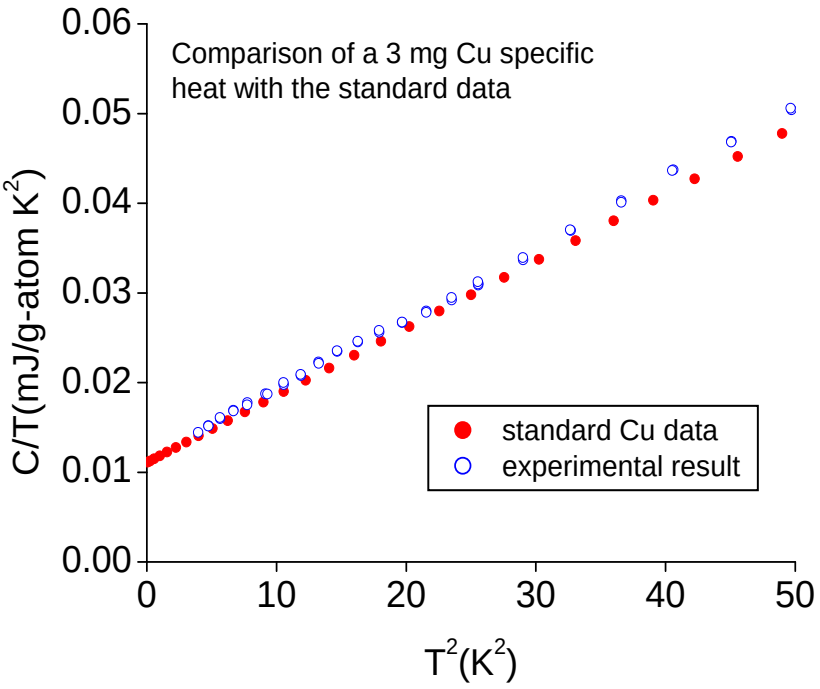

Figure 3.5: Specific heat of a 3 mg copper sample at ambient field.

jump at T_c around H = 4000 Oe. The jump at T_c in zero field is related to γ_n by the relation $\Delta C = 1.43\ \gamma_n\ T_c$. If γ_n=8.8 mJ/mole K^2, and $\Delta C/T_c$=10.9 mJ/mole K^2, from the zero field data, are used, $\Delta C = 1.24 \pm 0.2\ \gamma_n\ T_c$ is obtained. The error results from the uncertainty in determining the magnitude of the jump and the T_c. These tests on small pieces of copper and niobium show that our specific heat setup is capable of measurements with an absolute accuracy of ±5%, and relative accuracy of ±1%.

Before presenting our data, the dirty d-wave symmetry which was not discussed in Chapter 1 should be briefly explained.

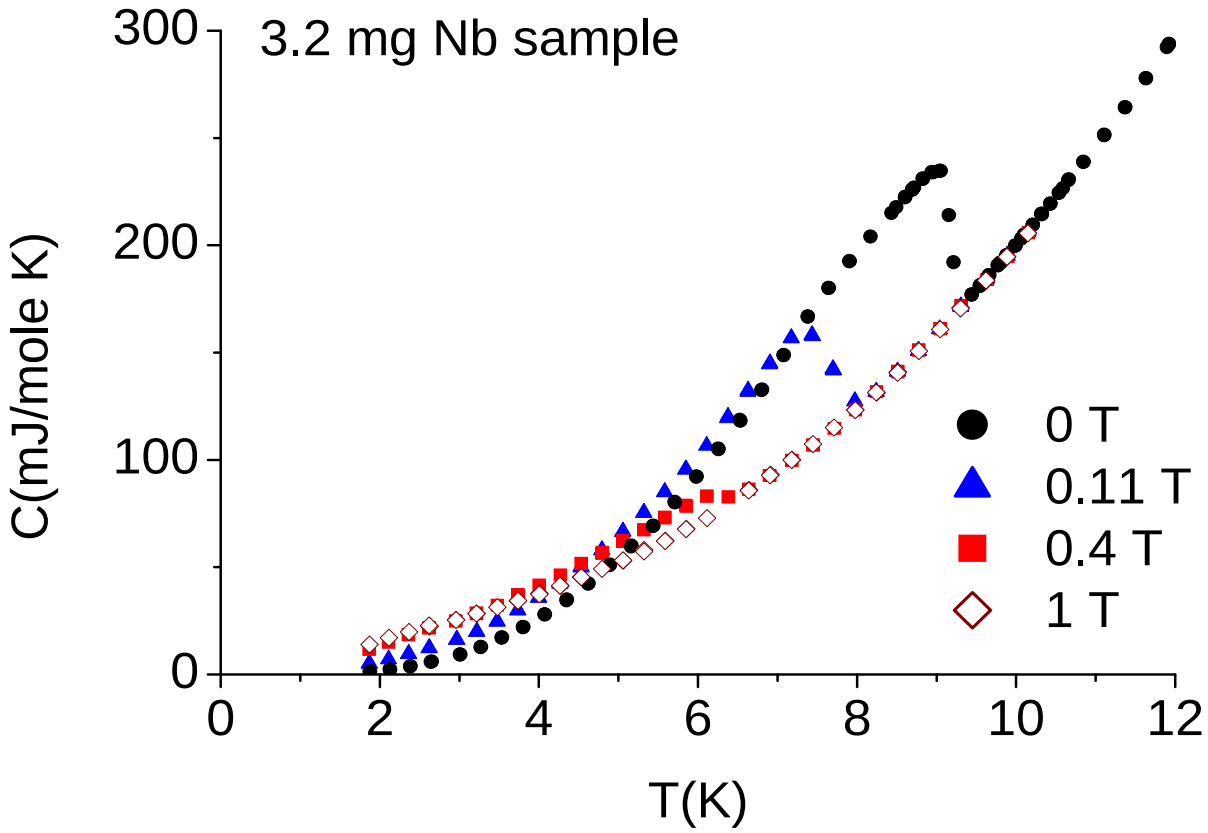

Figure 3.6: Specific heat of a 3.2 mg niobium wire at different magnetic fields.

3.3 Dirty d-wave model

In the presence of a magnetic field the quasiparticle spectrum in a superconductor will be Doppler shifted by the supercurrent flow around the vortex cores. In a nodal superconductor the Doppler shift of the quasiparticle energy becomes comparable to the gap magnitude close to the nodes. Therefore, a residual density of quasiparticle states is created at the Fermi level due to this effect. The limit in which the Doppler shift is the dominant mechanism of quasiparticle excitation is called the clean d-wave limit.

On the other hand in the presence of impurities there will be impurity states created in the superconducting gap, and unlike the case in semiconductors these states are not localized. If there are enough impurities in the system these non-localized states form a band of impurity states. Close to the nodes, this impurity band will set the energy threshold for the quasiparticles to be excited to the single particle states above the Fermi-level. In the limit where this impurity band is larger than the Doppler shift energy (particularly at low fields where the Doppler shift is small), the quasiparticles cannot be excited above the superconducting gap as was the case in the clean d-wave case. Hence the clean d-wave limit is not valid anymore. This limit is called the dirty d-wave limit. Mathematically the dirty limit is expressed as $k_B T << (H/H_{c2})\Delta_0 << \gamma_0 << \Delta_0$, where Δ_0 is the gap maximum and γ_0 is the impurity band width.

The $\sqrt{H}$-like magnetic field dependence of the electronic specific heat, discussed in Section 1.2, is a characteristic of d-wave symmetry in the clean limit. This magnetic field dependence is modified in the dirty limit, and an $H \log H$ type field dependence is predicted [108]. However the difference between the electronic specific heat in the clean and dirty limit is usually smaller than the experimental accuracy, and the experimental data can usually be fit equally well by both models. For example the YBCO data in Ref. [40] is well-explained by clean d-wave symmetry,

however Ref. [108] shows that the same data is also consistent with dirty d-wave symmetry. The situation is not different for LSCO where both clean d-wave and dirty d-wave model could explain the experimental data [109, 45].

Our specific heat data on PCCO also does not agree significantly better with any of the two limits of the d-wave symmetry, therefore in the rest of this chapter only clean d-wave limit is considered. However, one should keep in mind that the dirty d-wave symmetry is as equally valid as the clean d-wave symmetry. Now we can start discussing our data.

3.4 Specific heat measurements on the optimally-doped $Pr_{1.85}Ce_{0.15}CuO_4$ crystals

The specific heat of several crystals of optimal or near optimal doping has been measured. The mid-point of the superconducting transition temperature was between 21-24 K for various crystals, with a transition width that changed between $\pm$1K to $\pm$3K. The size of the crystals varied from 1 mg to 7-8 mg. Even though it is possible to grow larger crystals, the width of the transition usually increased with increasing crystal size. Since the signal-to-noise ratio was good enough for a few mg size crystals, the size of the crystals we studied was generally less than 5 mg.

The crystal shown in Fig. 3.7 has a T_c=22$\pm$2K, so it is near optimal doping (it might be slightly over-doped since some of our other optimally-doped crystals had T_c's as high as 25K). Fig. 3.7-a shows temperature dependence of the specific heat at six different fields, 0 T, 1 T, 2 T, 3T, 8 T and 10 T applied perpendicular to the ab-plane of the crystal, and Fig. 3.7-b shows the 0T and 10T data in a smaller scale from which $\gamma(0)$, γ_n and β were extracted. As Fig. 3.7-a shows the heat capacity has already saturated to the field-independent normal-state heat capacity at 8T, which means that $H_{c2} \leq$8 T in the optimally-doped crystal.

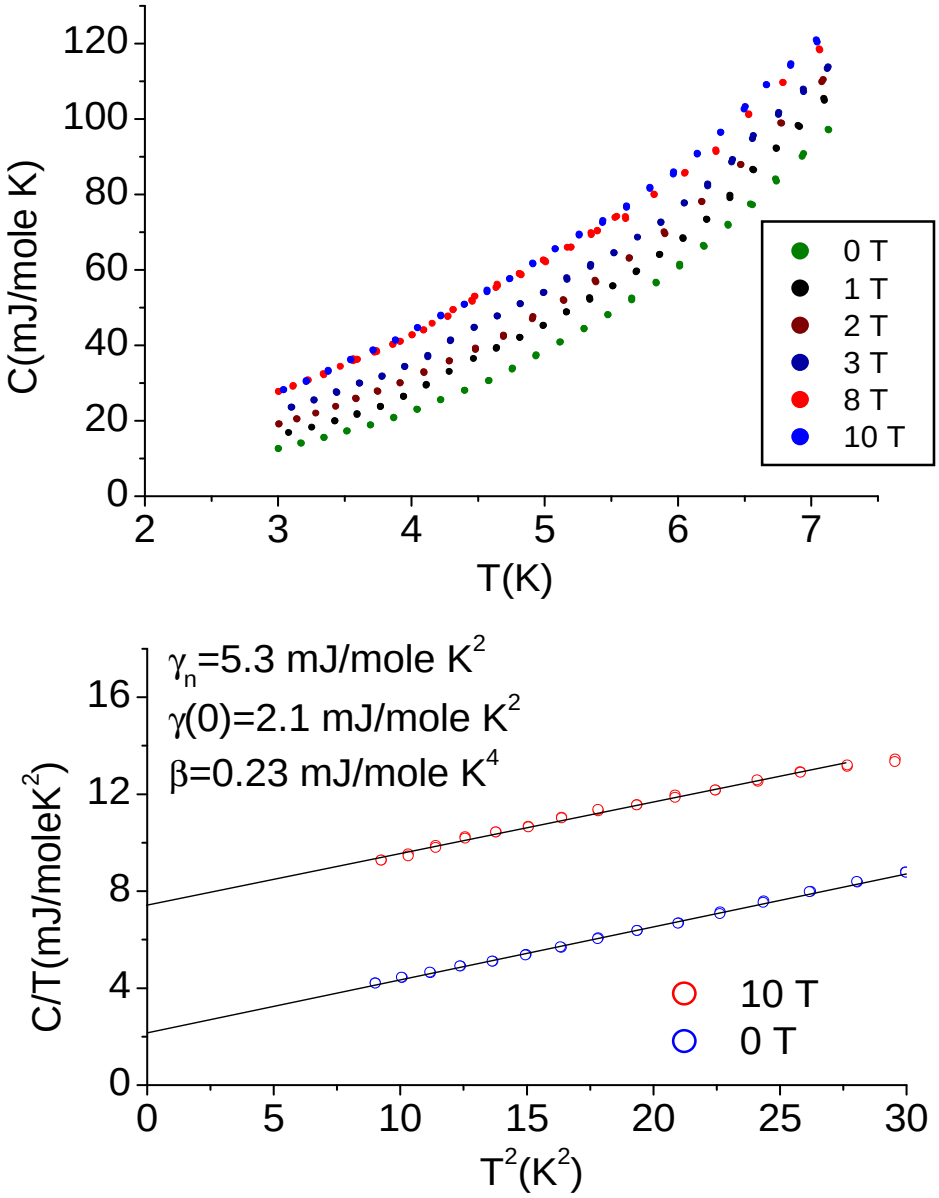

Figure 3.7: (a)-Specific heat of an annealed PCCO x=0.15 crystal with T_c=22±2K as a function of temperature at different magnetic fields (applied perpendicular to the ab-plane). (b)- The 10 T and 0 T data is plotted as C/T vs T^2 in order to show how β, $\gamma(0)$, and γ_n are extracted from the temperature dependence of the specific heat. γ_n is the difference of the intercepts of 10 T and 0 T data (7.4-2.1=5.3 mJ/moleK^2).

An important parameter to extract from this data is γ_n, which can be obtained from the difference of the intercepts of 10T and 0T data (see Fig. 3.7-b). A global fit, which assumes the phonon coefficient, β, constant for all fields and coefficient of electronic contribution, γ(H), variable for different fields has been used to analyze the data. The intercept of the 0T data is $\gamma(0)$=2.1 $\pm$0.2mJ/moleK^2 and the intercept of the 10T data is 7.4 $\pm$0.2mJ/moleK^2. The Sommerfeld constant γ_n, which is the difference between these two intercepts, is obtained to be γ_n=5.3 $\pm$0.3mJ/moleK^2.

These values are consistent with measurements performed on different optimally-doped crystals with similar H_{c2}. However, optimally cerium-doped crystals which had smaller H_{c2} than the crystal in Fig. 3.7-b had smaller γ_n values. For example the optimally cerium-doped crystal shown in Fig. 3.25 has $\gamma(0)$=2.0 $\pm$0.2mJ/moleK^2 and γ_n=4.1$\pm$0.3 mJ/moleK^2. As will be discussed later $\gamma(0)$ is not sensitive to oxygen content, but γ_n strongly depends on both cerium and oxygen content of the crystal. Therefore, variation in γ_n in optimally cerium-doped samples is indicative of different oxygen dopings in different crystals.

Another intrinsic parameter β was determined from the slope of the global linear fit to be β=0.23$\pm$0.2 mJ/moleK^4(see Fig. 3.7-b). Measurements performed on other crystals yield β values similar to β=0.23$\pm$0.2mJ/moleK^4 for optimally-doped PCCO (for another example see Fig. 3.25 which has β=0.24$\pm$0.2mJ/moleK^4). Using β=0.23$\pm$0.2mJ/moleK^4 results in a Debye temperature of θ_D=390$\pm$15K. These values are in reasonable agreement with the other published data in the literature(β = 0.244 mJ/mole K^4, and θ_D = 382 K in Ref. [110]). We should also note that the values of $\gamma(0)$ we find for PCCO are similar to the $\gamma(0)$ values found in the hole-doped superconductors($\gamma(0) \approx 1-2$ mJ/mole-K^2 for YBCO [40, 41, 42]).

Another common measurement used to characterize the samples in specific heat measurements is to measure the jump in the specific heat at T_c, which is due to the more ordered (less entropy) nature of the superconducting state compared to the normal state. The broad superconducting transitions in the electron-doped cuprates

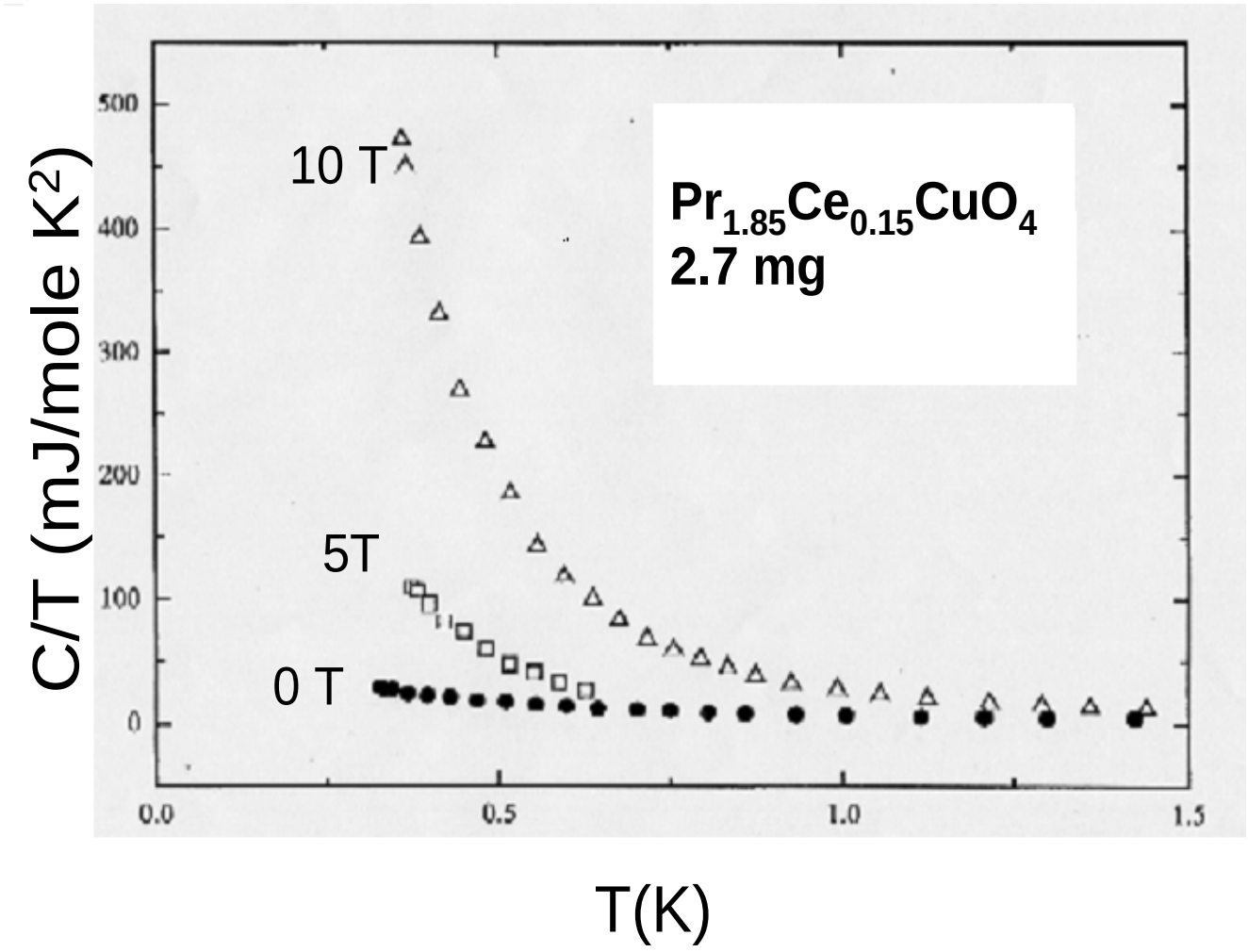

Figure 3.8: Specific heat of one of our annealed PCCO x=0.15 crystals shows a nuclear Schottky upturn at T<1.5K. The specific heat was measured by G.Stewart et al. at the University of Florida. The magnetic field is applied perpendicular to the ab-plane.

have made it very difficult to observe this jump by just analyzing the zero-field data (the jump is most prominent at zero-field). Instead we took advantage of the low H_{c2} of PCCO to measure the entropy difference between the normal state and the superconducting state. Fig. 3.9 shows the difference in the specific heat between 5 T (where the sample is almost completely normal in the measured temperature range) and 0T. For this measurement two crystals from the same batch with the same T_c are used. The total mass of the crystals is 5.1 mg, and T_c=22±3K (from magnetization measurements). The peak of the jump is at 19K which is consistent with the lower end of the transition from magnetization measurements, at which point the samples should be completely superconducting. We measured γ_n=4.2±0.2 mJ/mole K^2 and $\Delta C/T_c$=6.1±0.3 mJ/moleK^2 for these crystals (considering the peak temperature as the T_c). This results in $\Delta C/\gamma_n T_c$=1.4±0.2. As a reference we can compare this number by the BCS prediction for s-wave superconductors which is $\Delta C/\gamma_n T_c$=1.43.

Prior attempts to measure the anomaly at T_c for electron-doped cuprates were mostly unsuccessful due to the difficulty of observing the anomaly by just analyzing the zero-field data [111] (unlike our case where the phonon and residual electronic contributions are subtracted out by taking the difference between the zero field and 5 T data). In the studies in which the electronic contribution have been extracted by some subtraction method, the magnitude of the jump is much smaller than ours (less than half of what we observe) which is most likely do to the higher volume fraction of superconductivity in our samples [112]. Similar measurements on hole-doped cuprates showed different results. The magnitude of the jump is similar to BCS prediction for LSCO [113, 114], but not in YBCO. For example in Ref [42], $\Delta C/\gamma_n T_c$=4.1±0.8 has been found for YBCO, which is significantly higher than the BCS result. The commonly cited BCS result of $\Delta C/\gamma_n T_c$=1.43 is actually for the case of weak coupling between the electrons through electron-phonon interaction. The unusually large $\Delta C/\gamma_n T_c$ ratio in YBCO is attributed to strong coupling effects of unknown origin.

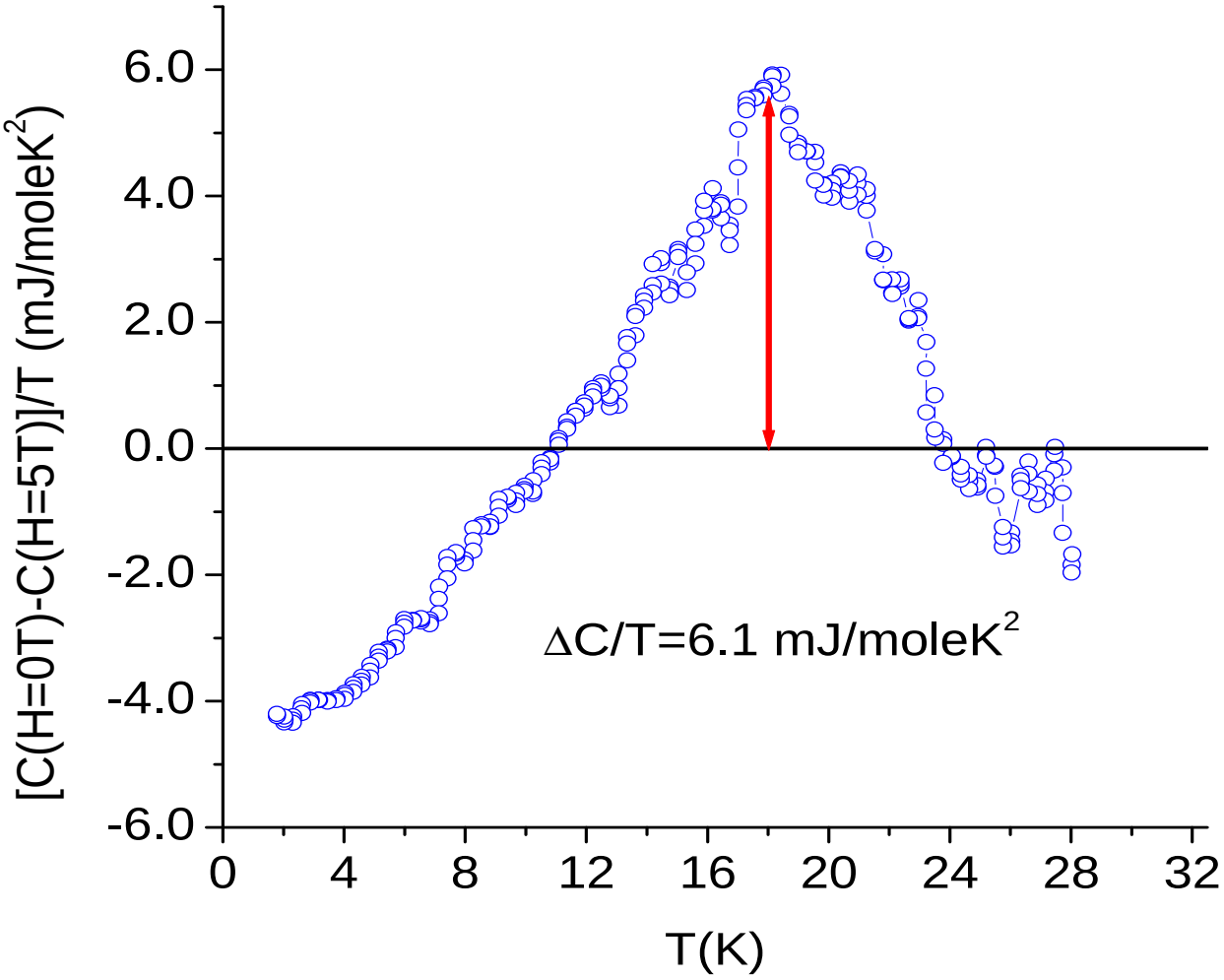

Figure 3.9: Difference between the specific heat in the normal state and the superconducting state for optimally-doped PCCO.

From Fig. 3.9 we can also calculate the entropy difference between the superconducting state and the normal state. The difference between the superconducting state entropy (S_s) and the normal state entropy (S_n) is defined as:

$$S_n(T) - S_s(T) = \int_0^T \frac{C_s - C_n}{T} dT. \tag{3.7}$$

By integrating the area under the curve of Fig. 3.9, the entropy difference between the superconducting and normal states can be calculated (see Fig. 3.10).

Another important parameter that can be calculated from this data is the condensation energy, which is the difference between the free energies of the superconducting and the normal states. This energy is basically the area under the curve in Fig. 3.10, and by definition it is equal to $U_0 = \frac{H_c^2}{8\pi}$, where H_c is the thermodynamic critical field:

$$U_0 = \int_0^T (S_n - S_s) dT = \frac{H_c^2}{8\pi}. \tag{3.8}$$

Fig. 3.11 shows the temperature dependence of the condensation energy (obtained by integrating the area under the curve of Fig. 3.10). The units of the condensation energy are taken as mJ/mole to be consistent with the rest of the thesis. The condensation energy can also be compared with a simple d-wave BCS prediction [115]:

$$U_0 = \alpha N(0) \Delta_0^2/2 \approx 2.1 \times 10^{-5} \alpha \gamma_n \Delta_0^2/2, \tag{3.9}$$

where N(0) is the DOS at the Fermi level, which can be written in terms of γ_n, $\alpha \approx 0.4$ for d-wave superconductors, γ_n=4.2 mJ/mole K^2, and $\Delta \approx 4$ meV for optimally-doped PCCO. Substituting these numbers yields $U_0 \approx 800$ mJ/mole for the BCS d-wave superconductivity prediction for optimally-doped PCCO. In order to calculate the BCS s-wave condensation energy, α= 1 should be substituted in Eq. 3.9, which results in $U_0 \approx 2000$ mJ/mole. The experimental value of U_0=568 mJ/mole is in much better consistency with BCS d-wave prediction, however, it is still significantly lower than the theoretical value. Similar discrepancies between experimental and theoretical values for condensation energy are also observed for hole doped cuprates

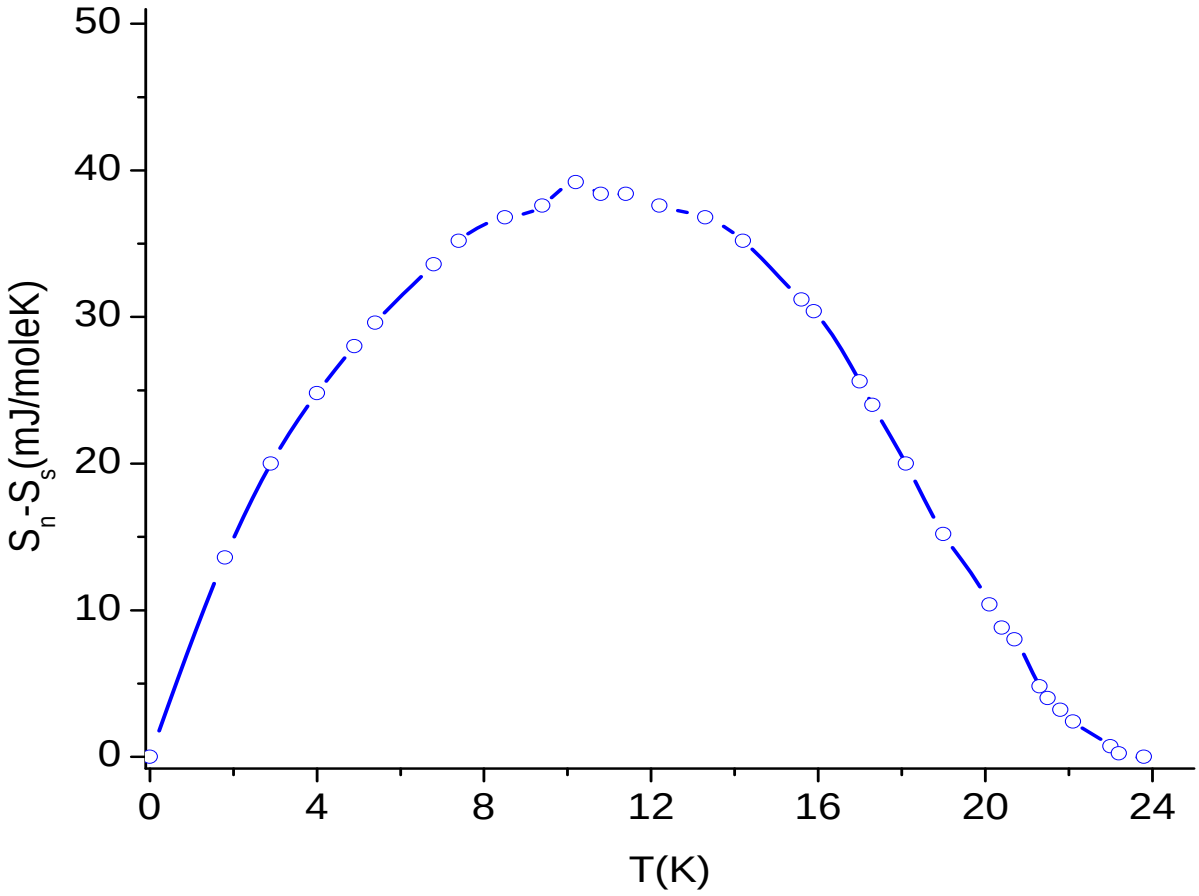

Figure 3.10: Entropy difference between the superconducting and normal states for optimally-doped PCCO. The first point (0,0) is added to the data (both of the superconducting and normal state entropies have to be zero at zero temperature) to enable further analysis.

(see for example Ref. [113] for data on LSCO). These discrepancies are most likely due to less than 100% volume fraction of superconductivity in the samples.

Fig. 3.12 shows the temperature dependence of the thermodynamic critical field, which is calculated by using Eq. 3.8. In order to calculate H_c, the condensation energy should be converted into erg/mole, which is 10^{-4} mJ/mole. In addition, $H_c^2/8\pi$ should be multiplied by the molar volume of PCCO, which is 114 cm^3. This calculation yields a thermodynamic critical field of 1116 Oe which is in reasonable agreement with the rough estimate of $H_c \approx \sqrt{H_{c1}H_{c2}} \approx \sqrt{100 \times 60000}$ ≈2450 Oe [47], where $H_{c1} \approx 100$ Oe and H_{c2} ≈60000 Oe for these samples. The line in Fig. 3.12 shows a simple BCS fit of the form $H_c(T) = H_c(0)[1 - (\frac{T}{T_c})^2]$ [47], by using $H_c(0)$=1116 Oe, and T_c=20K (a point between the specific heat peak temperature and where the experimental H_c goes to zero). As is clear from the figure there is a deviation between the data and the simple BCS relation, particularly close to T_c where fluctuation effects, which are not included in the BCS relation, are dominating the physics. Another possible reason for the deviation is the spread in the superconducting transition temperature between the different parts of the sample.

As mentioned before, the field dependence of the electronic specific heat can be used to differentiate between different pairing (gap) symmetries. In our study, measuring the field dependence of the electronic specific heat is particularly advantageous since the PCCO crystals that we used in our study do not have an electronic or nuclear Schottky contribution in the temperature (T>2K) and field range of our study (unlike another popular n-doped cuprate NCCO that has a large Schottky contribution below ∼5K). However, a nuclear Schottky contribution has been observed in one of our PCCO x=0.15 superconducting samples at T<1.5K in the measurements made by G.Stewart *et al.* at the University of Florida, Gainesville(see Fig. 3.8, this data is not published). This Schottky contribution, which is due to the nuclear moments of praseodymium and copper, limits the ideal range of field dependent specific heat measurements to T>2K.

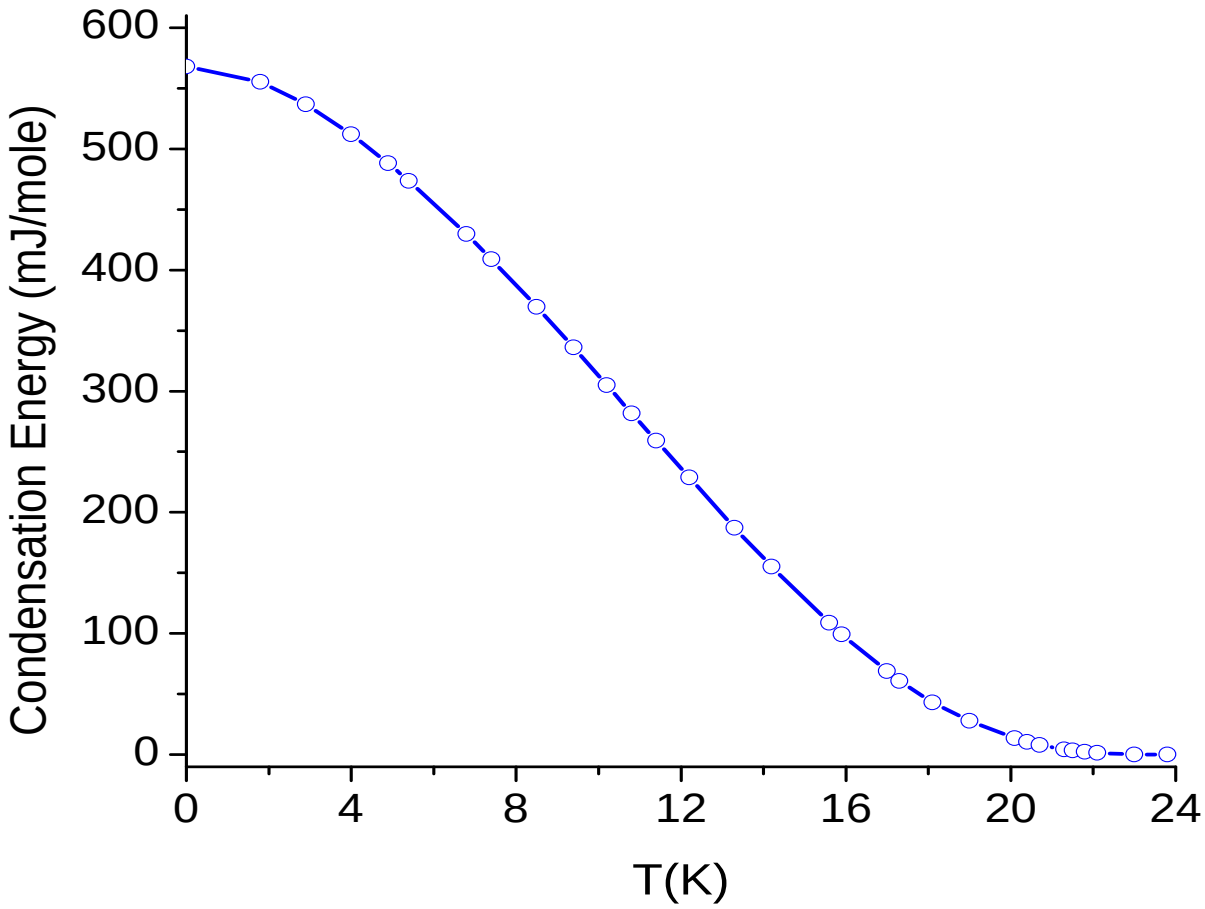

Figure 3.11: Temperature dependence of the superconducting condensation energy.

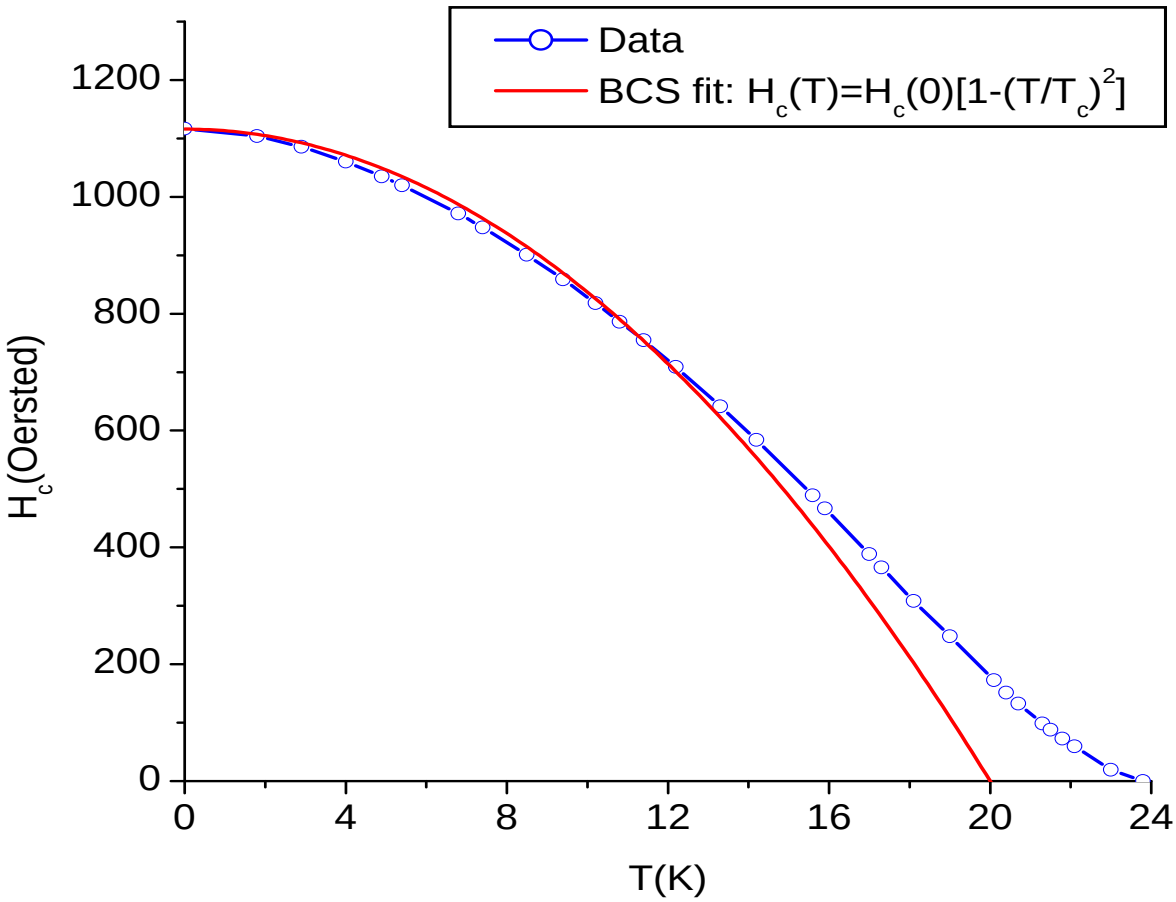

Figure 3.12: Temperature dependence of the thermodynamic critical field. The line is a d-wave fit by using $H_c(0)$=1116 Oe, and T_c=20 K.

Since our addenda does not have a field dependence, the only field-dependent part in our measurements is the electronic specific heat (also confirmed by our specific heat vs temperature at constant field measurements). Subtracting the zero field specific heat from the specific heat at other fields gives the field-dependent part of the electronic specific heat. Therefore our measurements were mostly taken at a constant temperature (zero field cooled) while the magnetic field was ramped up.

Fig. 3.13 shows theoretical fits to the 3.4 K data in the field range 0 - 2 T. Only the field-dependent part of the electronic specific heat is shown in Fig. 3.13 since the zero-field specific heat, which includes phonon contribution and the zero field residual heat capacity, is subtracted out. The low field part is important because the theoretical work on d-wave symmetry(clean or dirty) has focused on the dilute vortex limit($H_{c1} << H << H_{c2}$) to be able to ignore vortex-vortex interactions, so both Eq. 3.10 and Eq. 3.11 are valid in this limit [51, 55]. The clean d-wave fit is calculated using the equation [42]:

$$C_{el} = \gamma_n T \left(\frac{8}{\pi}\right)^{1/2} \left(\frac{H}{H_{c2}/a^2}\right)^{1/2} for \left(\frac{T H_{c2}^{1/2}}{T_c H^{1/2}}\right) \ll 1 \tag{3.10}$$

where $\gamma_n = 5.3$ mJ/mole K^2, $H_{c2} = 8$T, and $a = 0.7$ are used(a is a geometrical factor that depends on the vortex lattice geometry, and the value 0.7 was found experimentally for YBCO [40]). The dirty d-wave fit is calculated using the Eq. 3.11 with the same parameter values (except for the geometrical constant a which is defined differently in the dirty d-wave formalism) used for the clean d-wave fit:

$$C_{el}(H) = \gamma_n T \left(\frac{\Delta_0}{8\hbar\gamma_0}\right) \left(\frac{H}{H_{c2}/a^2}\right) log \left(\frac{\pi H_{c2}}{2a^2 H}\right), \tag{3.11}$$

where $\hbar\gamma_0$ is the impurity band width, Δ_0 is the superconducting gap maximum (determined from tunnelling spectroscopy experiments [37]), and a is a geometrical factor taken equal to 1 in dirty d-wave case. In the strong scattering limit (unitarity limit), γ_0 is given by $\gamma_0 \approx 0.61\sqrt{\Delta_0 \Gamma}$, where Γ is an impurity scattering rate which can be determined from penetration depth experiments. The clean d-wave fit is

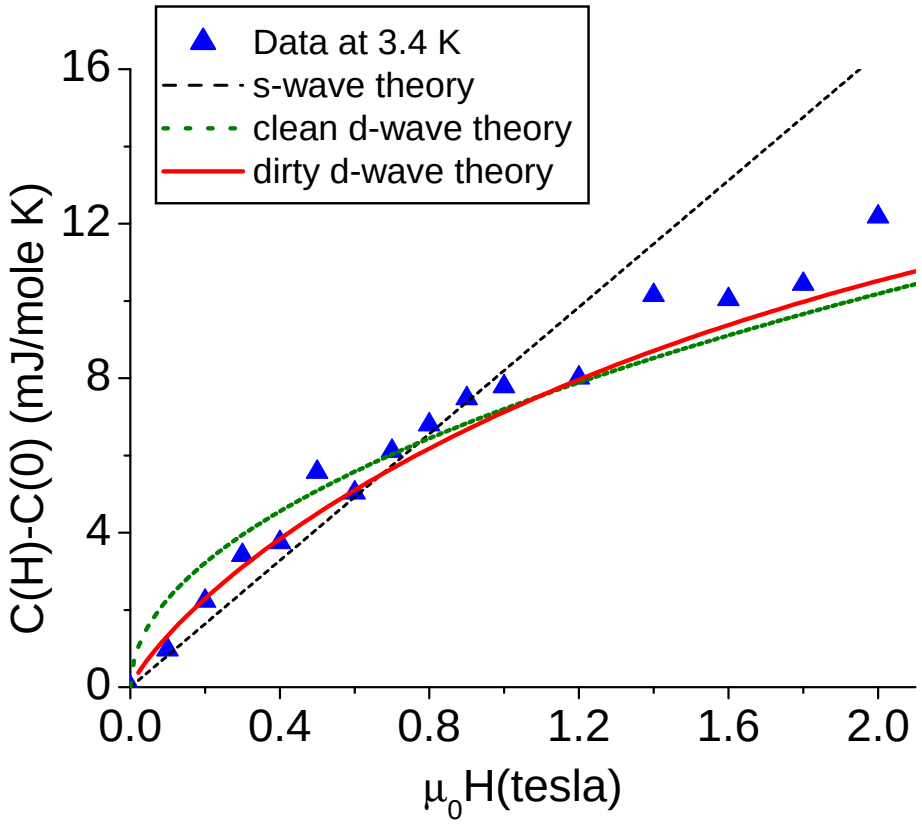

Figure 3.13: Field dependence of the electronic specific heat at 3.4 K for PCCO x=0.15 crystal. The magnetic field is applied perpendicular to the ab-plane.

clearly better than the linear s-wave fit. Given the scatter in our data it is difficult to differentiate between the clean d-wave and dirty d-wave fits. Therefore, we refer to the symmetry as d-wave without making a distinction between the clean limit and the dirty limit.

Based on this analysis it would seem that the optimally-doped PCCO has a d-wave symmetry. However, measurements performed on crystals of similar dopings at lower temperatures showed quite interesting results. Fig. 3.14 shows the field dependence of an optimally-doped crystal (x=0.15, T_c=23±3K, mass=3.4 mg) in the temperature range 2-4.5 K. A non-linear field dependence is quite clear in this crystal down to 3.5K, however, a dramatic change in the field dependence is observed when the temperature is reduced below 3K (see Fig. 3.15-a for a comparison of 2K and 3.5K data). The 3.5K and 4.5 K data can be very well fit by a d-wave form $C_{el} = AH^{1/2}$ where $A = \gamma_n T(\frac{8}{\pi})^{1/2}\frac{a}{\sqrt{H_{c2}}}$. On the other hand the electronic specific heat has a linear magnetic field dependence consistent with s-wave symmetry at T=2K.

Before comparing our data with different theoretical models, we should mention how the parameters used in the fits are determined. We need to determine γ_n and H_{c2} of the sample in order to estimate the specific heat for different symmetries. γ_n is determined in two different ways which produced consistent results. The first way to determine γ_n is to take the difference between the intercepts of C(H)/T vs T^2 data for $H>H_{c2}$ and H=0. An example of this was shown in Fig. 3.7-b. In addition to this method, there is also a method which results in a good estimate of γ_n (consistent with the results of the first method). At $T \ll T_c$ where the bulk of the sample is superconducting at zero field, γ_n can be determined by suppressing superconductivity with a large enough magnetic field ($H>H_{c2}$) and using the relation $C(T,H>H_{c2})-C(T,H=0)=\gamma_n T$.

Fig. 3.15-c shows a d-wave fit to the 4.5 K data. In calculating A, the coefficient of the $H^{1/2}$ term, γ_n=4.2 mJ/mole K^2, $H_{c2}(0)$=7T, and a=0.7 were used. As seen

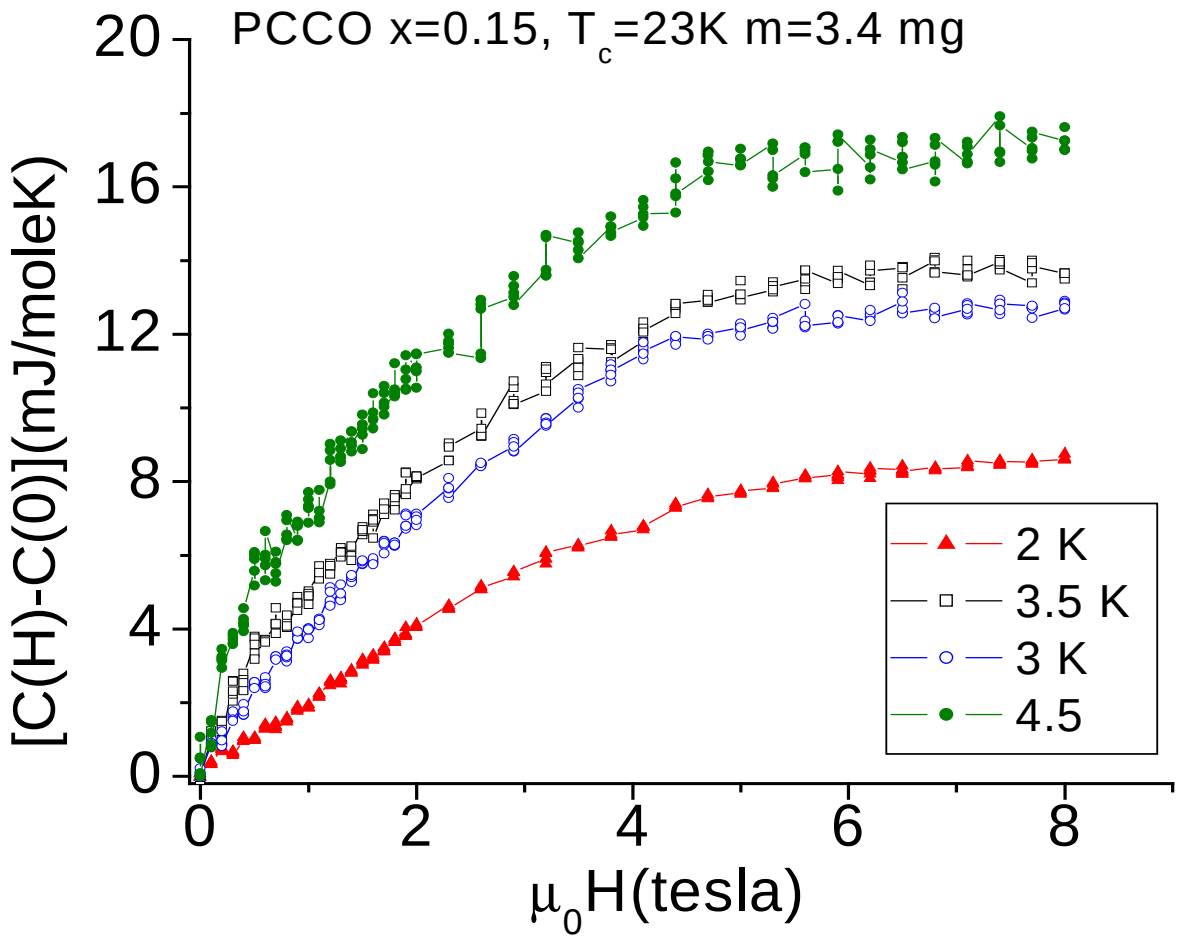

Figure 3.14: Specific heat of a PCCO x=0.15 crystal at different temperatures between 2K-4.5K. The change in the field dependence from non-linear at T≥3K to linear at T=2K is very unusual. The magnetic field is applied perpendicular to the ab-plane.

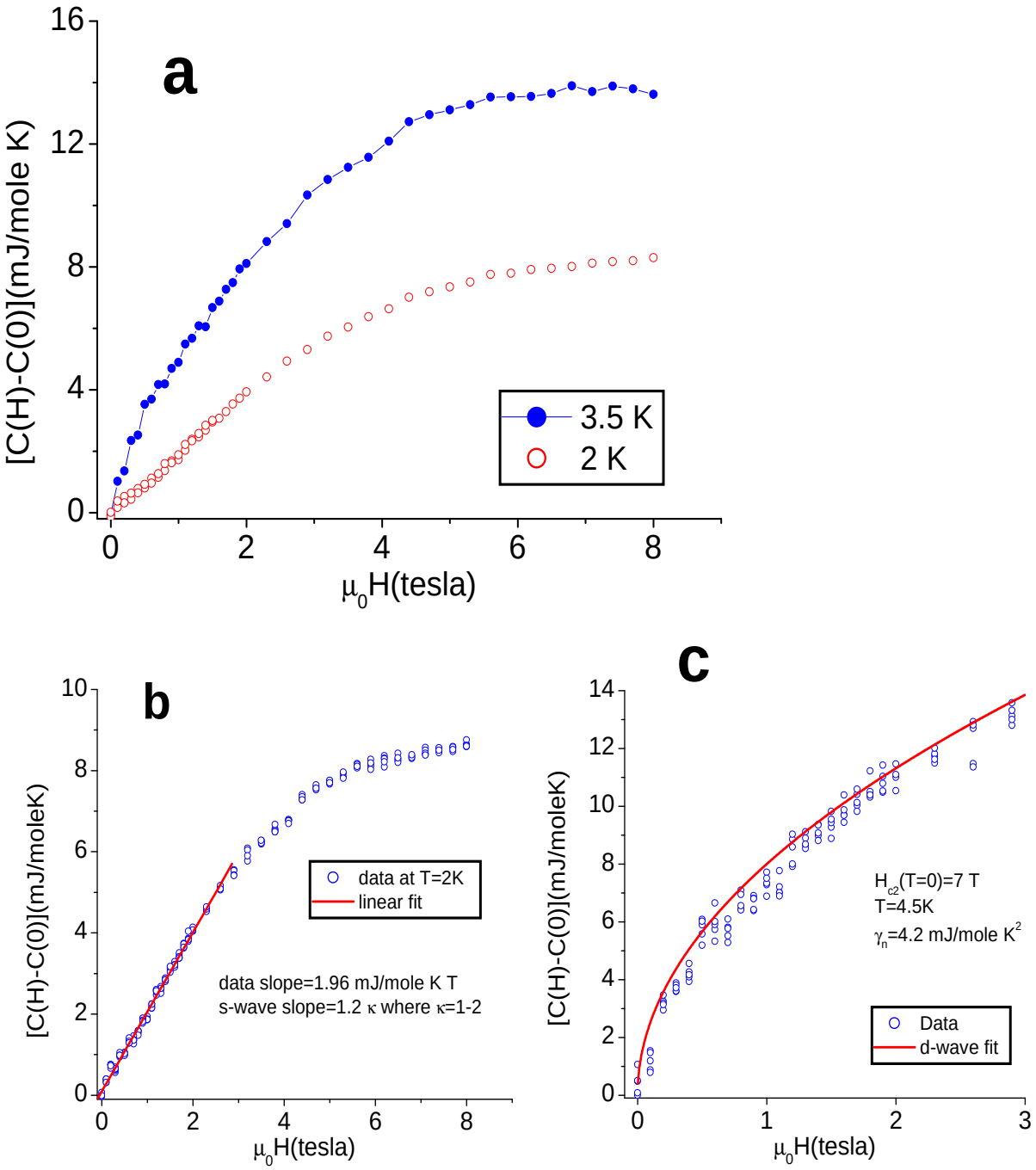

Figure 3.15: (a)-Field dependence of a PCCO x=0.15 crystal at 2K and 3.5K shows a drastic change within a very narrow temperature range. (b)- The line is a linear fit to the 2 K data. (c)-The line is a d-wave fit to the 4.5 K data which is shown with the circles.

in Fig. 3.15-c a reasonably good fit is obtained to our data at T=4.5 K. On the other hand, the slope of the linear field dependence observed at T=2 K is consistent with a gapped order parameter, $C_{el} = \kappa\gamma_n TH/H_{c2}(T)$. Using γ_n=4.2 mJ/mole K^2 and $H_{c2} = 7T$ at T=2 K yield $C_{el} = 1.2\kappa H$. On the other hand a linear fit to our data yields $C_{el} = 2.0H$. Since κ is a geometrical factor between 1-2, our data at T=2K is consistent with s-wave symmetry. This analysis would estimate κ=1.7 for optimally-doped PCCO.

This type of field dependence, non-linear at high temperatures and linear at lower temperatures, has been observed on different crystals. The data on two other crystals will be presented with more emphasis on the qualitative behavior of the field dependence at low temperature versus higher temperature field scans. A detailed discussion regarding the possible explanations of this behavior follows the presentation of the data.

Fig. 3.16 shows the field dependence of a PCCO x=0.15 crystal with a T_c=22±3K and a mass of 2.7 mg. The specific heat saturates to the normal state value at a lower magnetic field in this crystal compared to the sample shown in Fig. 3.14, which suggests that the oxygen content of this crystal is different from that of the other crystal. However, similar to the other crystal there is a change in the field dependence of the electronic specific heat between 3.5 K and 2 K. The field dependence at 3.5K is definitively non-linear, while the 2K data shows a linear field dependence up to at least 2T.

Fig. 3.17 shows another optimally doped crystal with a T_c=23±3K and a mass of 2.4 mg. The critical field in this crystal is H_{c2} ≈7 T at T=2K, and the linear field dependence in this sample persists up to T≈3K. However, at T=5 K again the field dependence becomes non-linear.

There are several possible scenarios to explain such an unusual change in the field dependence of the electronic specific heat: a phase transition in the symmetry of the order parameter from d-wave at high temperatures to a gapped order parameter at

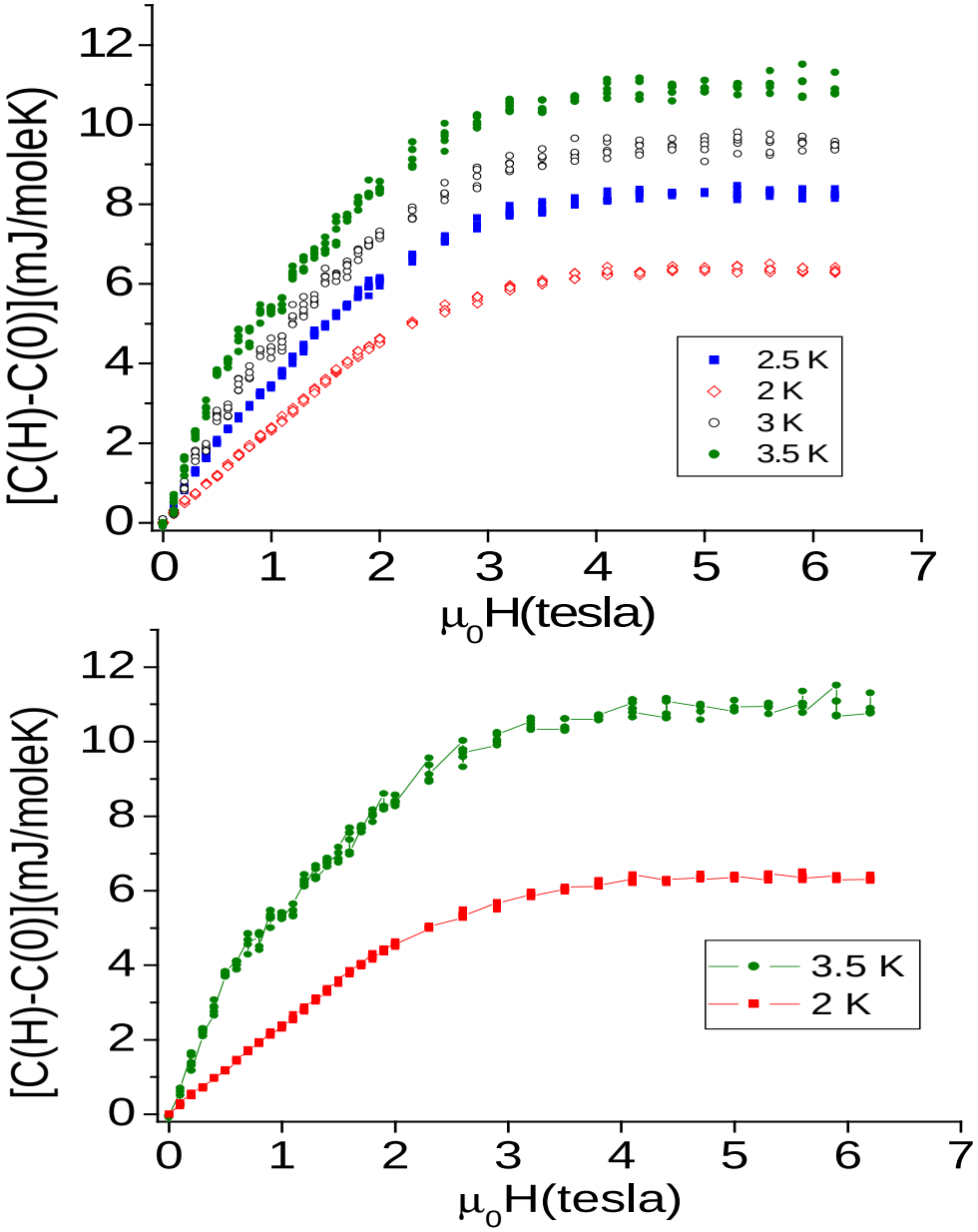

Figure 3.16: Field dependence of a different PCCO x=0.15 crystal between 2-3.5K.

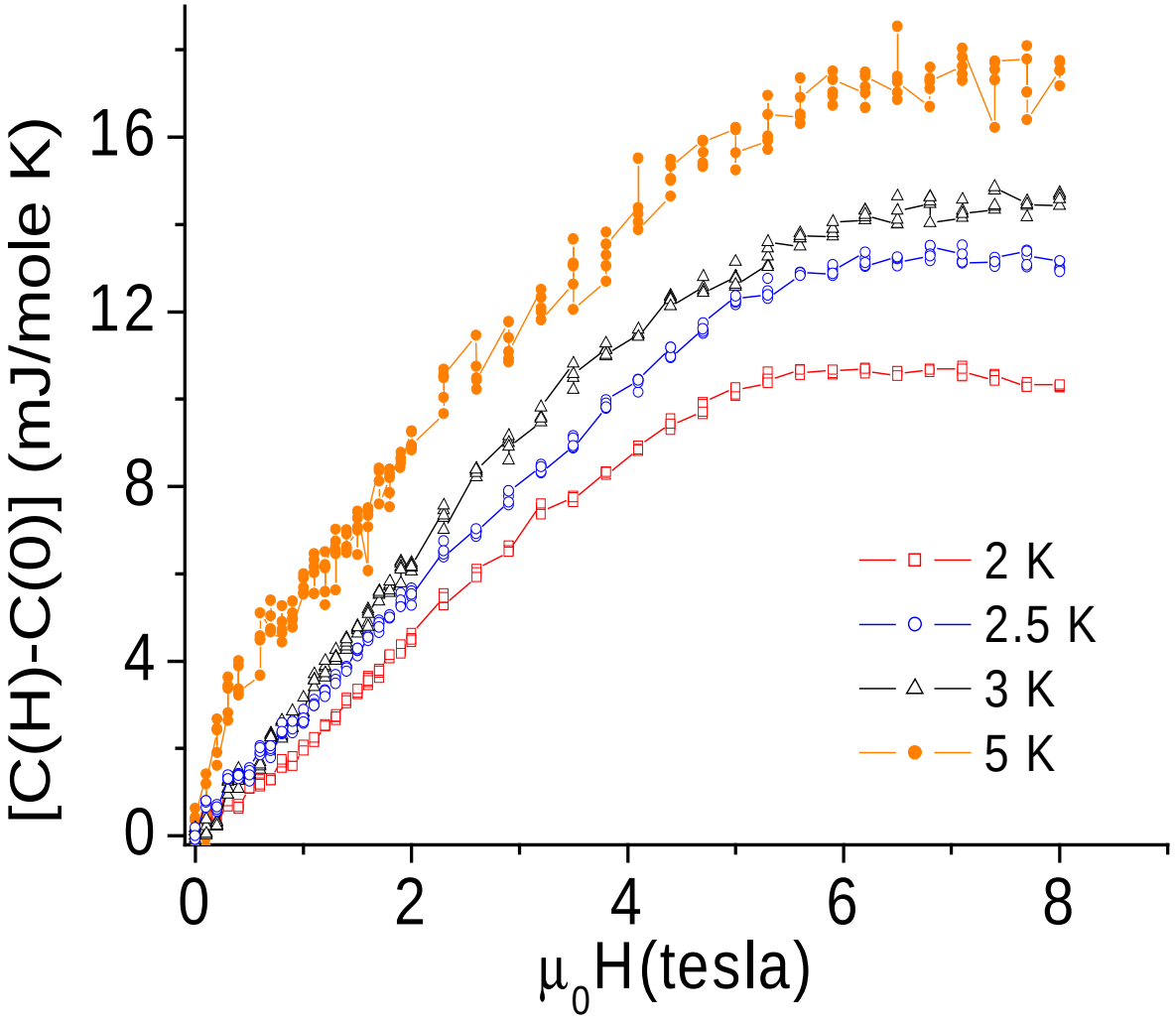

Figure 3.17: Field dependence of a different PCCO x=0.15 crystal between 2-5K.

low temperatures, an anisotropic s-wave gap which has a minimum around 3K, or some flux effect that is not related to the gap symmetry at all. Now we will discuss each of these scenarios in more detail. The discussion will be based mainly on the data shown in Fig. 3.14 with the data on the other crystals also taken into account.

In Fig. 3.18 we plot the data of Fig. 3.14 in the form [C(H)-C(0)]/T versus field. This shows that the change in the field dependence of the electronic specific heat is accompanied by a suppression of the specific heat, which means that the density of states is suppressed along with a change in the field dependence. This dramatic change could be due to opening of a gap on the Fermi surface as the temperature is reduced, which causes the field dependence to go from non-linear (nodes in the order parameter) to linear (fully-gapped order parameter). This scenario is also supported by the quantitative analysis of the data since the d-wave theory is quantitatively consistent with the 4.5K data and a gapped symmetry is quantitatively consistent with the 2K data.

A phase transition in the symmetry of the order parameter is an attractive possibility since it has the potential of reconciling the results of many conflicting experiments. The experiments that suggested d-wave symmetry in electron-doped cuprates are almost exclusive performed above 4 K. These experiments are the phase sensitive SQUID experiment (4.2 K, optimally-doped sample) [34], the Raman spectroscopy experiment (4.2 K, optimally-doped sample) [36], and the ARPES experiments (4.2 K, optimally-doped sample) [24]. On the other hand the experiments that suggested s-wave symmetry are performed at T$\leq$2 K. These experiments are penetration depth (0.4 K-all dopings) [39] and point contact tunnelling spectroscopy (1.8 K, optimally and over-doped samples did not show a ZBCP which is a signature of d-wave symmetry in a superconductor) [37]. However, there is one conflicting experiment with this picture- the penetration depth measurements of Kokales *et al.* and Prozorov *et al.* which showed d-wave symmetry for even T<2K [32, 33].

The phase transition suggested in this scenario is also compatible with a theo-

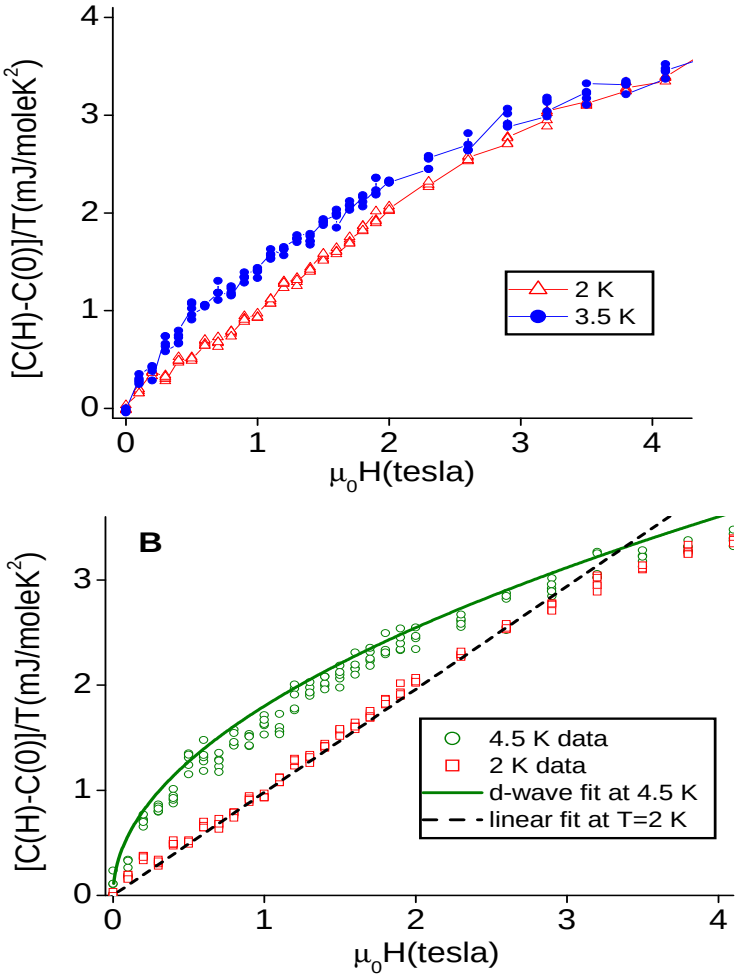

Figure 3.18: **a**-The change in the field dependence is accompanied by a suppression of the electronic specific heat as the temperature is reduced from 3.5 K to 2 K. **b**-the same suppression is also observed between 4.5 K and 2 K. The curved-line is a d-wave fit to 4.5 K data and the dashed line is an s-wave fit to the 2 K data.

retical model proposed by Khodel et al [116]. In their model as the electron-doped cuprates are doped beyond optimal doping, the hot spots, the intersecting regions of the magnetic Brillouin zone with the Fermi surface, which are responsible for the d-wave symmetry, approach each other. At a certain doping they become so close that it is no longer favorable to switch the sign of the pairing symmetry, as in d-wave symmetry, and a new fully-gapped order parameter emerges. According to this model in a certain narrow doping range the transition from d-wave symmetry to a gapped symmetry should also be observed with a decrease of temperature or magnetic field (see Fig. 3.19 for a phase diagram predicted by this model). However, we should also mention that Khodel *et al.* suggest that the gapped phase symmetry could be p-wave rather than s-wave. This assertion is not based on the model itself but rather on the strong doping dependence of the transition temperature in the over-doped range of the electron-doped cuprates which is unusual for an s-wave superconductor (for example T_c=22 K in our optimally-doped, x=0.15, crystal whereas T_c ≈15 K in the over-doped, x=0.17, crystal). In an s-wave superconductor the transition temperature should not change much with such small changes in the cerium doping since the phonon spectrum, and electron-phonon coupling do not change significantly in the corresponding doping range. We find these arguments very circumstantial and leave the type of the gapped-phase symmetry as an open question at this moment.

An anisotropic s-wave gap is another possible explanation for the change in the field dependence of the electronic specific heat as the temperature is reduced. This anisotropic gap should have a minimum amplitude of 2K (∼0.18 meV). Since the amplitude of the gap maximum is determined to be ∼ 4meV from tunnelling spectroscopy [37], the anisotropy in the magnitude of the gap ($\Delta_{max}/\Delta_{min}$) is around 20, which is very large. Most anisotropic s-wave superconductors have an anisotropy less than 2, except the recently measured borocarbide superconductor $LuNi_2B_2C$ [118] which has an anisotropy over 10.

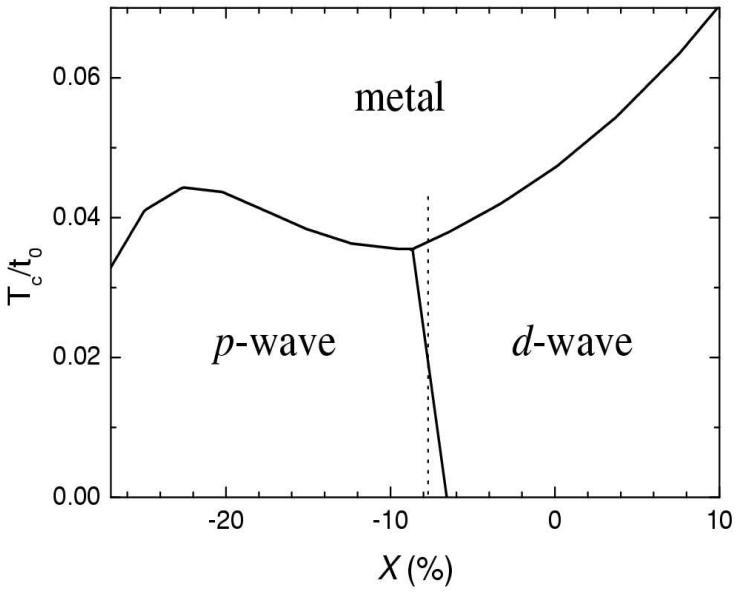

Figure 3.19: Phase diagram suggested by Khodel *et al.* which involves a transition in the symmetry of the order parameter [117].

This scenario has the advantage of being very simple. In addition, there are experiments that reported non-linear field dependence for the electronic specific heat in superconductors with an anisotropic s-wave symmetry [119], which could explain the non-linear field dependence we observe at high temperatures without the need for d-wave symmetry. Another support for this scenario comes from the recent penetration depth measurements performed on high-quality PCCO thin films [39] which showed a small gap, the magnitude of which is 1/3 the gap maximum, $\Delta_{max}/\Delta_{min}$ $\approx$3, observed in tunnelling measurements, at low temperatures. Hence, the anisotropy is much less than that observed in our data.

However there is a problem in explaining the linear field dependence of the electronic specific heat at 2K at such high fields as 2-3T (depending on the H_{c2} of the sample). In the case of an anisotropic s-wave gap the effect of increasing the magnetic field should be similar to increasing the temperature, since increasing the magnetic field increases the Doppler shift of the quasiparticles and excites them across the gap (just like thermal energy). The energy of the quasiparticles is shifted by an amount $\approx \Delta_{max}\sqrt{H/H_{c2}}$ in a magnetic field H. This energy corresponds to several kelvins at 1T (assuming Δ_{max}=4 meV, and H_{c2}=8 T). Hence, given the non-linear field dependence even at very low magnetic fields (H>0.1T) at 3.5K, the field dependence at 2K should not have continued to remain linear to such high fields as 2-3T.

As a final alternative we consider a vortex-vortex interaction induced change in the field dependence of the electronic specific heat (C_{el}). Vortices can interact with each other via quasiparticle (QP) transfer between their cores. At high magnetic fields (large number of vortices) or high temperatures (larger vortex-core size) the quasiparticle wavefunctions in the core of one vortex overlap with the quasiparticle wavefunctions in neighboring vortices, and hence inter-vortex quasiparticle transfer becomes possible. These inter-vortex QP transfers result in a shrinking of the vortex cores [120]. This in turn gives rise to non-linear magnetic field dependence in the

electronic specific heat. The calculations of Ichioka *et al.* [121], which took into account these vortex-lattice effects, showed that $C_{el} \propto H^{0.67}$ at $T=0.5T_c$ for an s-wave superconductors. Calculations of Miranovic *et al.* [122] at lower temperatures, where less overlap between vortex-cores reduces these effects and the size of the vortex-core is approximately constant for $H<0.5H_{c2}$, showed that $C_{el} \propto H$ for $H<0.5H_{c2}$ at T=0.1Tc.

These ideas were experimentally supported by the non-linear field dependence of the electronic specific heat observed in some s-wave superconductors, e.g. V_3Si [123], $NbSe_2$ [124], and $CeRu_2$ [125] (see Fig. 3.20 for an example in V_3Si). Despite some complications that were discovered after the original work, a vortex-lattice transformation in V_3Si [126] and anisotropic gap in $NbSe_2$ [118], the fundamental mechanism of vortex-core shrinking due to vortex-vortex interaction is still consistent with the non-linear field dependence observed in these materials [126].

The change in the field dependence of the electronic specific heat in PCCO is in qualitative agreement with these theories for an s-wave superconductor. However, in PCCO the change in the field dependence occurs over a very narrow temperature range $C_{el} \propto H^{0.5}$ at $T \approx 0.2T_c$ and $C_{el} \propto H$ at $T \approx 0.1T_c$) compared to the gradual and slower change based on vortex-lattice effects predicted in Ref. [121, 122] for a conventional s-wave superconductor ($C_{el} \propto H^{0.67}$ at $T=0.5T_c$ and $C_{el} \propto H$ at $T=0.1T_c$). Hence, it is very unlikely that the non-linear field dependence we observe in PCCO is due to a vortex lattice effect. On the other hand, the linear field dependence that we observe at T=2K is very similar to what is predicted by Ref. [122] for an s-wave superconductor (linear up to $0.5H_{c2}$ and non-linear at higher fields), which suggests that the symmetry of the order parameter is s-wave at T=2K.

Given the difficulty of completely ruling out any of the possible scenarios, at this stage it is not possible to make a definite conclusion about the reason for the change in the magnetic field dependence of the PCCO electronic specific heat. However, the consistent linear magnetic field dependence observed at the lowest temperature

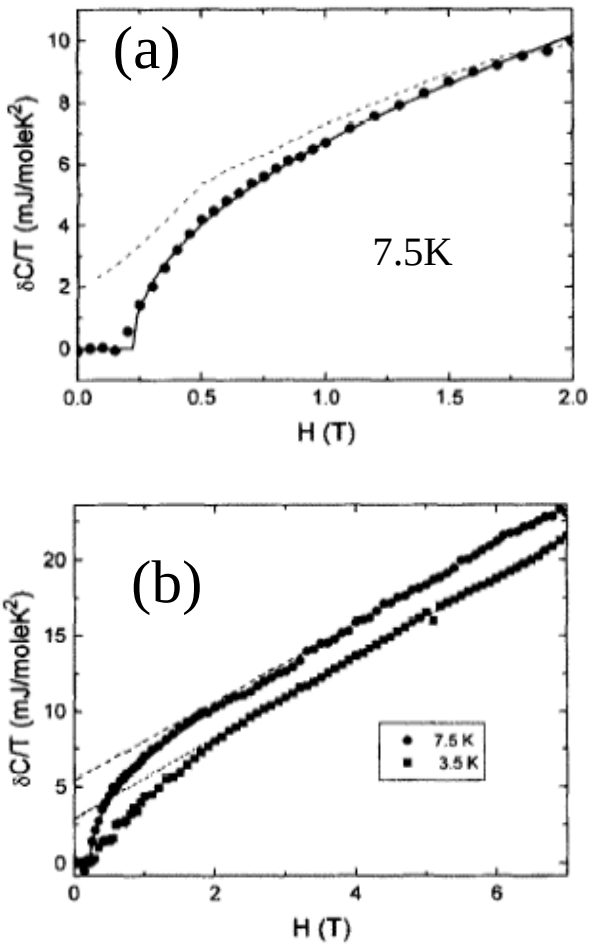

Figure 3.20: (a)-$\sqrt{H}$-like field dependence in a V_3Si polycrystal at 7.5K. The dashed line is taken while the field is ramped down. (b)- a comparison of the field dependence of specific heat at 3.5K and 7.5K. These two graphs are from Ref. [123].

(T∼2K) in the five crystals (see Fig. 3.27 for two other optimally cerium-doped crystals in addition to the three crystals presented above which show linear field dependence at T=2K) from different batches strongly suggests that **the symmetry of the order parameter at the lowest temperature is fully-gapped**. Even though vortex-vortex interaction or some strange flux effect can change a linear field dependence due to a gapped order parameter to a non-linear field dependence, it is not possible for a non-linear field dependence to look like linear due to any flux effect. Therefore the linear field dependence observed in our data means that the symmetry of the order parameter in the optimally-doped compound is fully-gapped.

3.5 Specific heat measurements on the over-doped $Pr_{1.83}Ce_{0.17}CuO_4$ crystals

This doping (x=0.17) is the highest over-doping we were able to get by the directional solidification technique. The mid point of the superconducting transition temperature for different crystals from this doping varied between 15 K to 12 K, usually with a transition width of ±1.5K (using the magnetization measurements). The amount of cerium in the start of the growth was enough to produce x=0.19 composition crystals, however after the growth WDX analysis showed that the composition of the crystals was $Pr_{1.83}Ce_{0.17}CuO_4$. The ab-plane resistivity of these crystals also did not show an upturn at low temperatures in the normal state ($H>H_{c2}$) consistent with the x=0.17 thin films.

The C/T vs T^2 data for a x=0.17 crystal at different fields applied perpendicular to the ab-plane is shown in Fig. 3.21. From this data γ_n=2.8±0.2 mJ/moleK^2 and $\gamma(0)$=4.0±0.2 mJ/moleK^2 are determined as done previously for the optimally-doped crystals. As done preciously for the optimally-doped crystals Fig. 3.21-b shows a linear fit to the 5 T data from which β=0.23±0.05 mJ/moleK^4, and hence

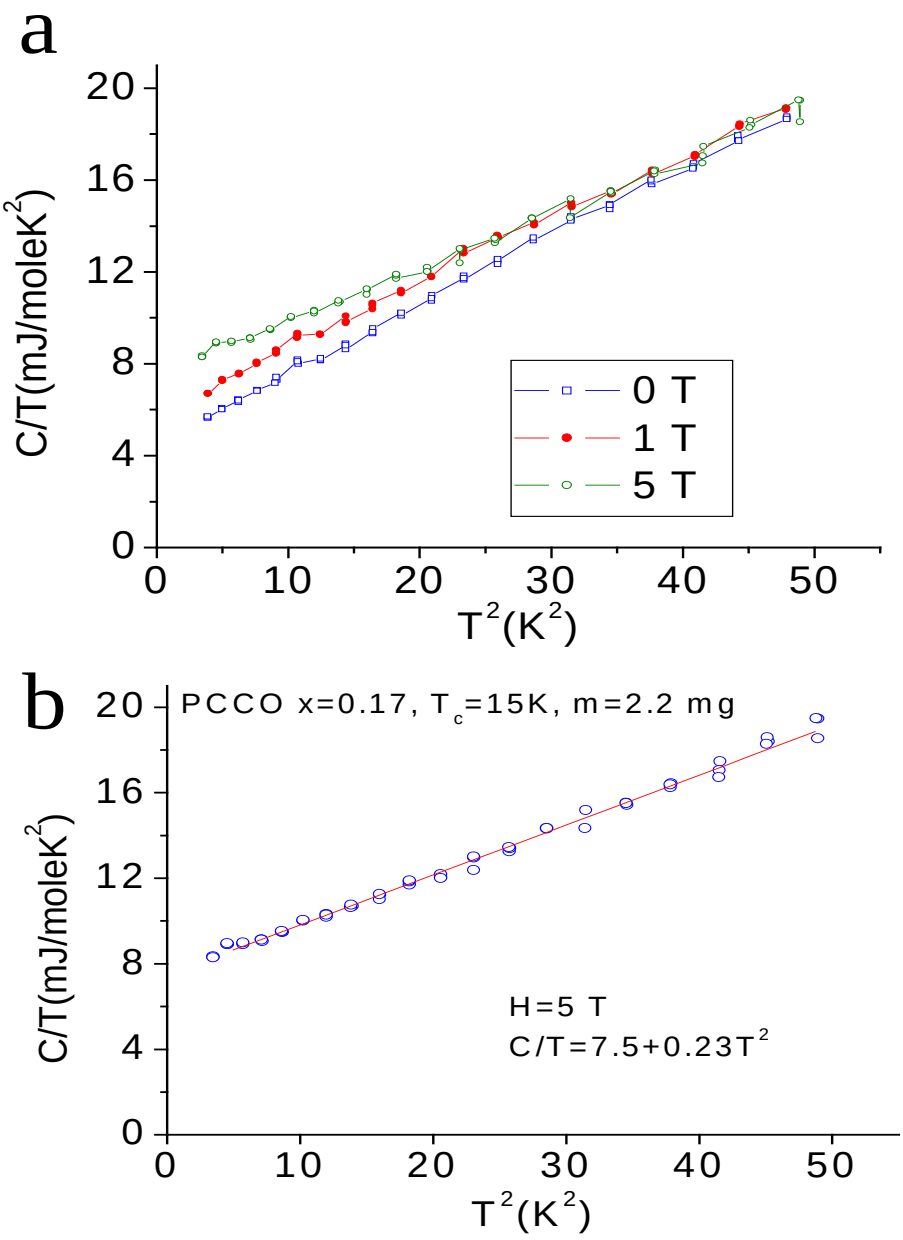

Figure 3.21: a-Specific heat of an annealed PCCO x=0.17 crystal as a function of temperature between 2-7K. The crossing between the data at different fields is due to the transition to the normal state. b- A linear fit to the 5 T data results in β=0.23 mJ/moleK^4 similar to the optimally-doped crystals.

Debye temperature θ_D=390±15K are determined.

The C/T vs T^2 data of these crystals show no Schottky upturn at any magnetic field. Therefore the only field-dependent contribution to the specific heat is the electronic specific heat. Fig. 3.22 shows the field dependence of the electronic specific heat at 2K, 2.5K, and 3K. γ_n can be extracted from Fig. 3.22 by $C(\mu_0 H = 5T, T = 2K) - C(\mu_0 H = 0T, T = 2K) = \gamma_n T = 2\gamma_n$ (this equation is valid only for T$\ll$T$_c$). $\gamma(0)$ can be extracted from $C(\mu_0 H = 0T, T = 2K) = \beta T^3 + \gamma(0)T = 8\beta + 2\gamma(0)$. If β=0.23 mJ/moleK^4 (from the temperature dependence in Fig. 3.21-b) is used, $\gamma(0)$ ≈4.0±0.2 mJ/moleK^2 is found.

Fig. 3.22 shows the field dependence of the electronic specific heat at 2K, 2.5K, and 3K. The electronic specific heat has a linear field dependence at T=2K. However, a very slight non-linearity is observed for T=2.5 K, and this non-linearity becomes more visible at T=3K.

Fig. 3.23 shows the data on the same sample for 2K, 3K, and 3.5K after the zero field specific heat is subtracted. Similar to the optimally-doped samples, this sample also shows a linear field dependence at low temperatures (T≈2 K) and at higher temperatures (T≈3 K) the field dependence becomes non-linear. Since the field range is quite narrow in this case no quantitative analysis was made to fit the data at 3.5 K to the d-wave theory. However the slope of the linear field dependence at 2 K data is consistent with a fully-gapped order parameter. A linear fit to the data yields a slope of 2.2 mJ/mole K T, and a s-wave theory predicts 1.4 κ for the slope (using γ_n=2.8±0.2 mJ/moleK^2 and H$_{c2}$=4 T). In this doping also κ is estimated to be 1.6 (same as the optimally-doped sample).

Our specific heat experiments are consistent with other experiments [127] which showed that the upper critical field H$_{c2}$ is smaller in the over-doped regime compared to the optimally-doped regime (H$_{c2}$ ≈ 4T at T=2K for x=0.17 whereas H$_{c2}$ ≈ 7T at T=2K for x=0.15).

There are some issues that require further study in order to be completely under-

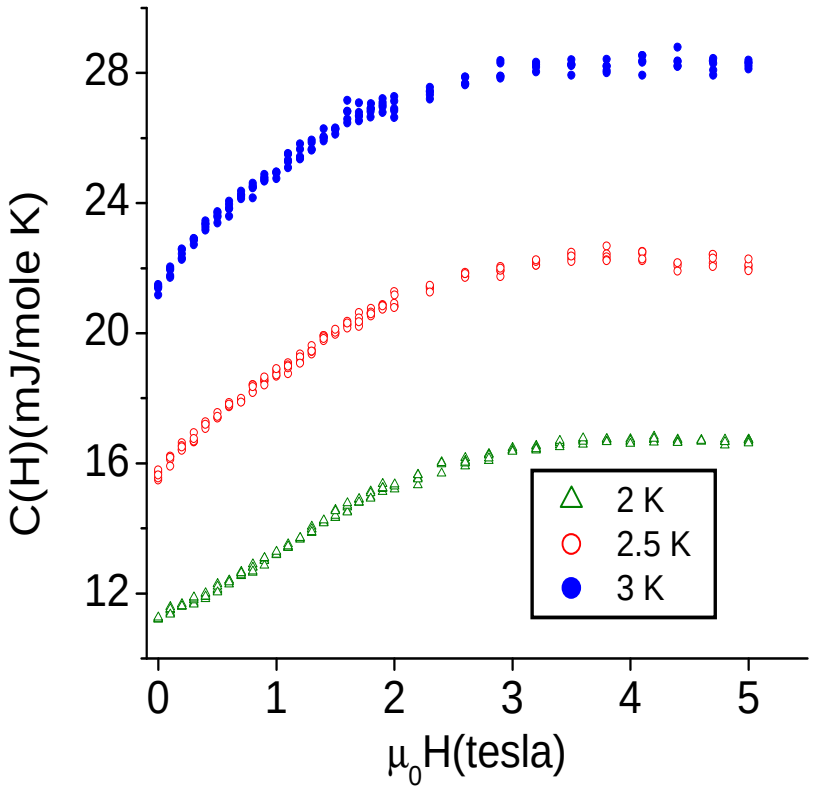

Figure 3.22: Field dependence of the electronic specific heat for a PCCO x=0.17 crystal at 2K, 2.5K and 3K. The magnetic field is applied perpendicular to the ab-plane.

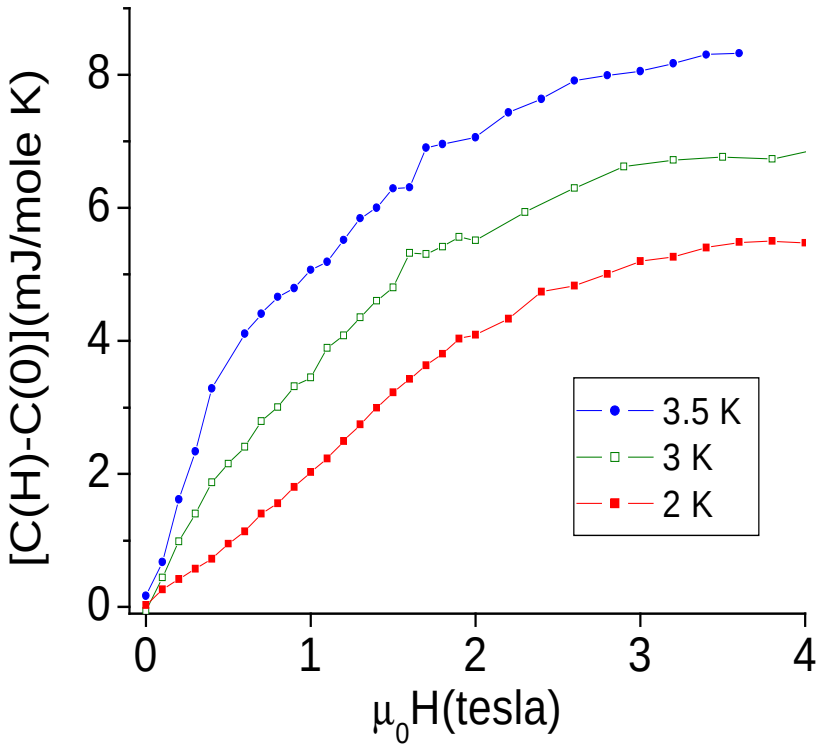

Figure 3.23: Field dependence of the electronic specific heat for a PCCO x=0.17 crystal at 2K, 3K and 3.5K after the zero field specific heat is subtracted.

stood. The first one is the fact that the exponential temperature dependence at low temperature, which is expected for a gapped superconductor, has not been observed in our crystals down to 2 K. If there were an isotropic s-wave gap throughout the Fermi surface large enough to produce a superconducting transition at 15 K, the exponential temperature dependence should have been observed below 4-5 K (when compared to conventional s-wave superconductors which show the exponential temperature dependence below roughly $T_c/3$ [48]). This observation combined with the penetration depth experiments on similar composition crystals [39], in which a gap much smaller than the conventional BCS gap is observed, imply that even if these crystals have an s-wave symmetry the gap is not isotropic throughout the Fermi surface and the minimum magnitude of the gap is several times smaller than the maximum amplitude of the gap. In order to completely understand this point, lower temperature measurements at zero field should be performed to search for the exponential temperature dependence.

Another point that requires further study is the large value of the residual zero field specific heat coefficient, $\gamma(0)$. $\gamma(0)$ was found to be 1-2 mJ/moleK^2 for the optimally-doped crystals, whereas in the x=0.17 crystals $\gamma(0)$=4.0$\pm$0.3 mJ/moleK^2. The reason for such a large value of $\gamma(0)$ is not understood at the moment. However, the fact that the value of $\gamma(0)$ has gone down in the hole-doped cuprates with improvements in the crystal quality imply that the over-doped $Pr_{2-x}Ce_xCuO_4$ crystals are not quite as high quality as the optimally-doped crystals. If we attribute the origin of this residual specific heat to the normal regions in the crystal, we would conclude that the concentration of these normal regions is higher in the over-doped crystals compared to the optimally-doped crystals. However, paramagnetic defects could also be the origin of $\gamma(0)$ as proposed for YBCO [63].

Another interesting issue that requires further study is the value of the normal state Sommerfeld coefficient, γ_n. γ_n is basically a measure of the density of states (see Eq. 4.11). Naively one might expect γ_n to increase as the doping is increased since

	Optimally-doped (x=0.15)	Over-doped (x=0.17)
β	0.23±0.02 mJ/mole K^4	0.23±0.02 mJ/mole K^4
θ_D	390±15 K	390±15 K
$\gamma(0)$	2.0±0.2 mJ/mole K^2	4.0±0.2 mJ/mole K^2
γ_n	5.3±0.3 mJ/mole K^2	2.8±0.2 mJ/mole K^2
$H_{c2}(0)$	8.0 ±0.5T	4.0±0.5 T

Table 3.1: Summary of our specific heat measurement results on optimally and over-doped PCCO.

more carriers are introduced into the system. However, γ_n=5.3 mJ/moleK^2 in the optimally doped crystals whereas for the x=0.17 crystals γ_n=2.8±0.2 mJ/moleK^2. This unusual behavior of γ_n can be understood in terms of the unusual Fermi surface of the electron-doped cuprates. ARPES studies have shown that electron-doped cuprates have a hole-like Fermi surface at optimal doping [128], and doping the parent compound with electrons (replacing Pr^{3+} with Ce^{4+} basically reduces the size of the Fermi surface, effectively reducing the density of states. Our data is qualitatively consistent with this picture, however, further studies are required to check if this model quantitatively agrees with our data.

For a summary of our results on the optimally-doped and over-doped samples see Table 3.1.

3.6 A study of oxygen reduction (annealing) with specific heat

The as-grown single crystals of electron-doped cuprates are not superconducting. The crystals have to be oxygen reduced in order to get superconductivity. The

oxygen reduction is achieved by annealing the crystals at $\sim 900^o$C for several days in an inert atmosphere. The early work in our group showed that $\approx$1% oxygen reduction is enough to make the semiconducting as-grown sample superconducting.

The effects of oxygen reduction on transport properties such as thermopower, Hall effect, resistivity have been studied by changing the annealing times and hence changing the oxygen content of thin film samples of optimally-doped PCCO and NCCO [129, 130]. In this section the effects of oxygen reduction on parameters such as the residual linear specific heat $\gamma(0)$, the phonon contribution β, and bulk H_{c2} will be presented by changing the annealing times of single crystals of optimally doped PCCO samples from the same batch.

The Debye temperature and the zero field residual heat capacity $\gamma(0)$ are two of the important parameters that are of interest for different experiments. Hence, we will start our discussion by presenting these parameters in an unannealed crystal. The Debye temperature is extracted from the low temperature phonon contribution to the specific heat βT^3 (see Eq. 1.5). Fig. 3.24 shows the specific heat of an unannealed crystal from 2-10K at 0T and 2T. Since the crystal is not superconducting there is no observable difference in the specific heat at the two fields. The intercept $\gamma(0)$=2 mJ/moleK^2 and the slope β=0.24$\pm$0.01 mJ/moleK^4 are found for the unannealed crystal. Hence the Debye temperature for the unannealed PCCO x=0.15 is 390$\pm$15K.

Now we start our discussion of comparing the bulk properties of a sample before and after annealing. Fig. 3.25 shows a comparison of C/T vs T^2 data for an optimally cerium-doped sample before and after annealing (the crystal shown in Fig. 3.24 is now annealed, and a comparison before and after annealing will be made). The sample is 6.8 mg, and it is annealed at 900^oC for two days. Fig. 3.25 shows that the slopes of the C/T vs T^2 data on the annealed sample at 10T and that of the non-annealed sample are the same. This means that the phonon contribution and hence the Debye temperatures are the same in the unannealed sample and the annealed

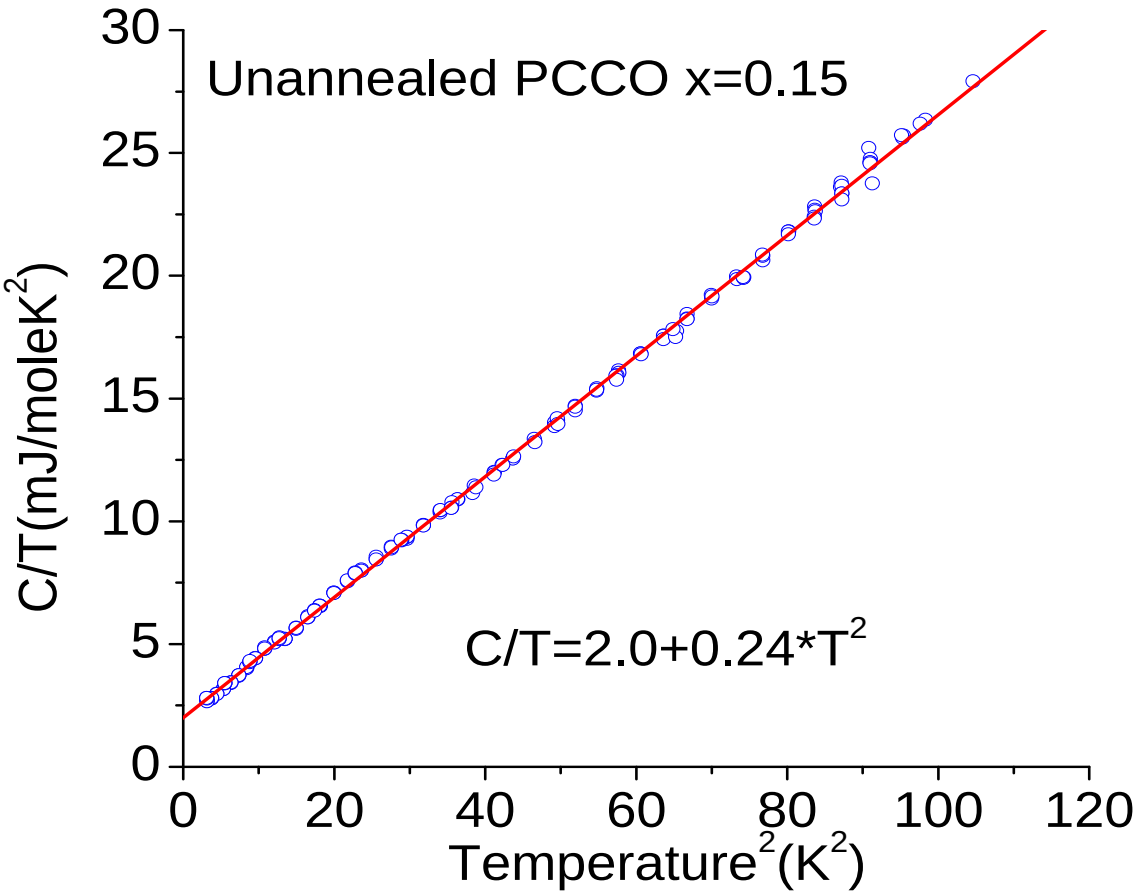

Figure 3.24: Specific heat of an unannealed PCCO x=0.15 crystal (non-superconducting).

sample in the normal state. Therefore, the effect of oxygen reduction on the phonon spectrum is small enough to be ignored. It is also interesting that the slope of the zero-field data on the annealed crystal starts to deviate from the other two curves at temperatures as low as 4K. This deviation is due to parts of the sample going through the superconducting to normal state transition as the temperature is increased. In other words the bulk of the sample becomes completely superconducting only at very low temperatures unlike what is observed in magnetization measurements in which the magnetic moment saturates at much higher temperatures (see the magnetization data on two day annealed sample in Fig. 3.26 for the magnetization data on this sample).

This broad superconducting transition of the electron-doped cuprate single crystals is the reason for the difficulty of observing the jump in the specific heat of these materials unlike the clear jump observed in Fig. 3.6 for niobium where the superconducting transition is very sharp. The fact that the effects of superconducting transition become significant at temperatures as low as 4K (at least for large crystals like this one) means that one should be careful when extracting the phonon contribution from the low field data, since just fitting a line to C/T vs T^2 data would result in an exaggerated phonon contribution, as is clear in Fig. 3.25.

Another important point to mention is the similarity, if not equality, of the $\gamma(0)$ term in the unannealed and annealed samples. As mentioned in Chapter 1 the origin of this term is not understood and there are several proposals to explain it: a band of normal state-like excitations within the nodal regions of the gap created by impurity scattering [45], gapless superconductivity [62], or contributions from non-superconducting but metallic regions in the sample [63]. Our data is most consistent with $\gamma(0)$ being due to non-superconducting regions in the sample. If there were a band of normal state-like excitations within the nodal regions of the gap created by impurity scattering in the superconducting state, the $\gamma(0)$ term should have become larger when the sample was made superconducting by reducing its oxygen

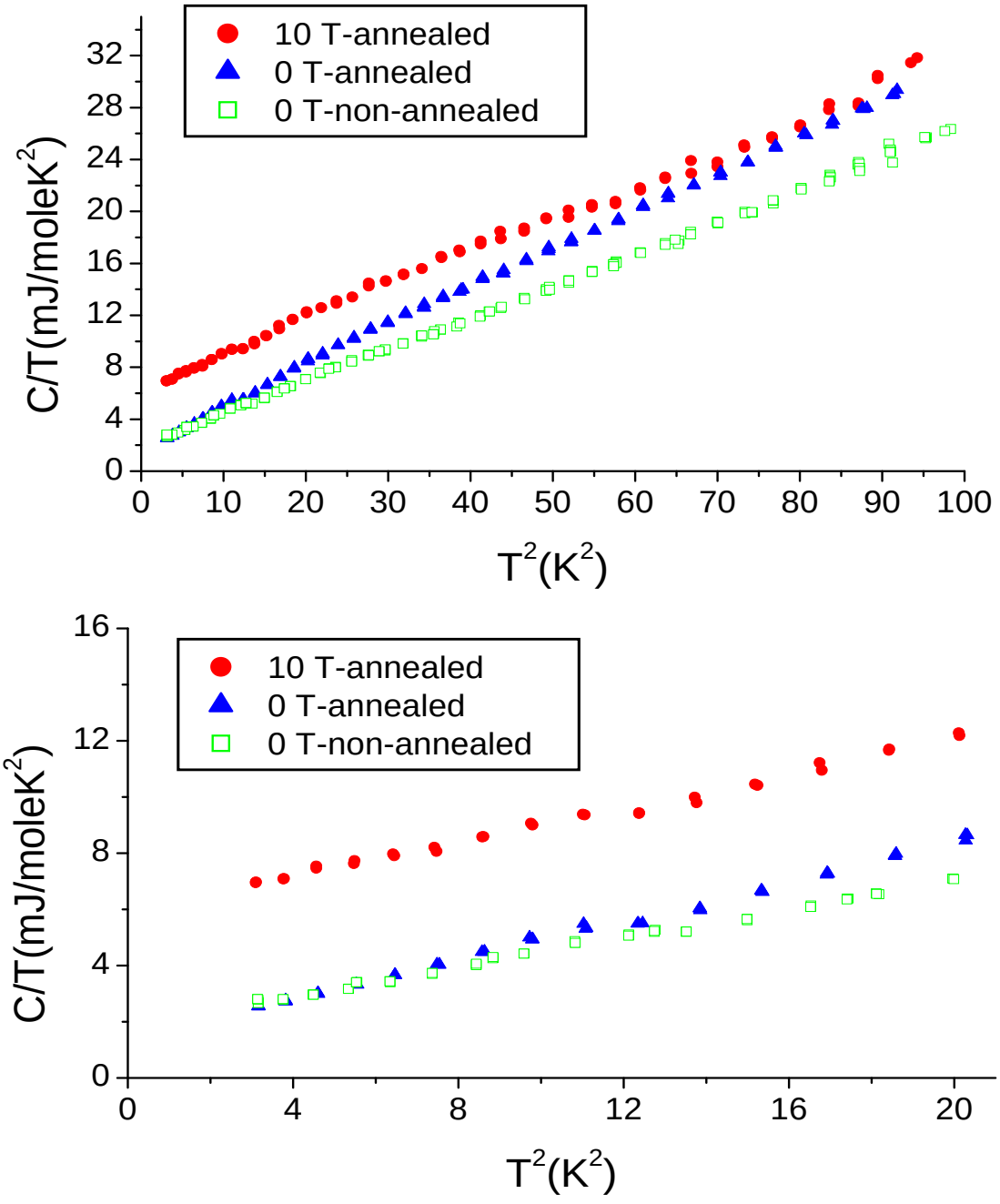

Figure 3.25: A comparison of specific heat of a sample before and after annealing.

content. However, there is no measurable difference in $\gamma(0)$ between the annealed or unannealed sample which means that the contribution to $\gamma(0)$ from normal regions created by impurity scattering is small or not existent. This is also consistent with a fully-gapped symmetry which is inferred from our field dependence data since such excitations would be suppressed due to the superconducting gap. Attributing $\gamma(0)$ to normal regions in the sample and the equality of $\gamma(0)$ before and after annealing imply that the normal (metallic) regions in the superconducting state also exist in the semiconducting unannealed samples. This contribution could be due to a metallic phase which does not become superconducting or change in concentration upon annealing. Such a phase has not been observed in X-ray spectroscopy (there are no extra peaks). Hence, if such a phase exists the concentration of it is less than the resolution of the X-ray measurements ($\approx 1\%$). Another possibility is that this phase is still PCCO but with a slightly different oxygen content. Such a phase would not be detected in X-Ray diffraction since it would have the same peaks as that of the superconducting phase.

It is also worth mentioning that such a residual contribution has not been observed in thermal conductivity measurements performed on crystals from our group [131]. The electronic contribution to thermal conductivity goes to a very small value (almost zero) when T$\rightarrow$0. This observation is also consistent with the non-existence of a delocalized band of normal state-like excitations within the nodal regions of the gap created by impurity scattering since such delocalized excitations would be expected to contribute to heat current and hence to thermal conductivity.

The effects of annealing on the bulk H_{c2} could also be studied with specific heat measurements. The electronic specific heat increases as the magnetic field is increased and at H_{c2} it saturates to the normal state specific heat, which does not change with further increase of the magnetic field. By studying crystals from the same batch but with different annealing times a correlation between the T_c of magnetization measurements, the oxygen content, and the bulk H_{c2} has been observed.

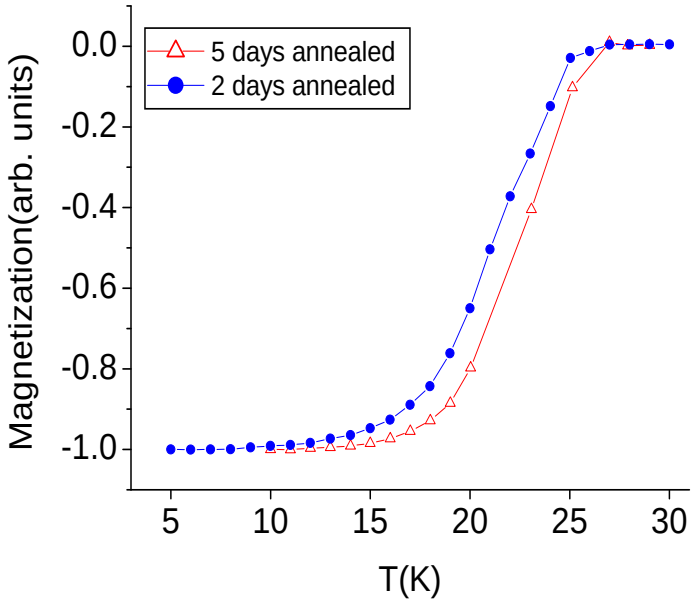

Figure 3.26: The superconducting transition of two PCCO x=0.15 crystals from the same batch annealed at 900^o for two days and five days (measured with a SQUID magnetometer). The magnetic moment is normalized to -1 at the low temperature saturation value in order to show the data on the two crystals on the same scale.

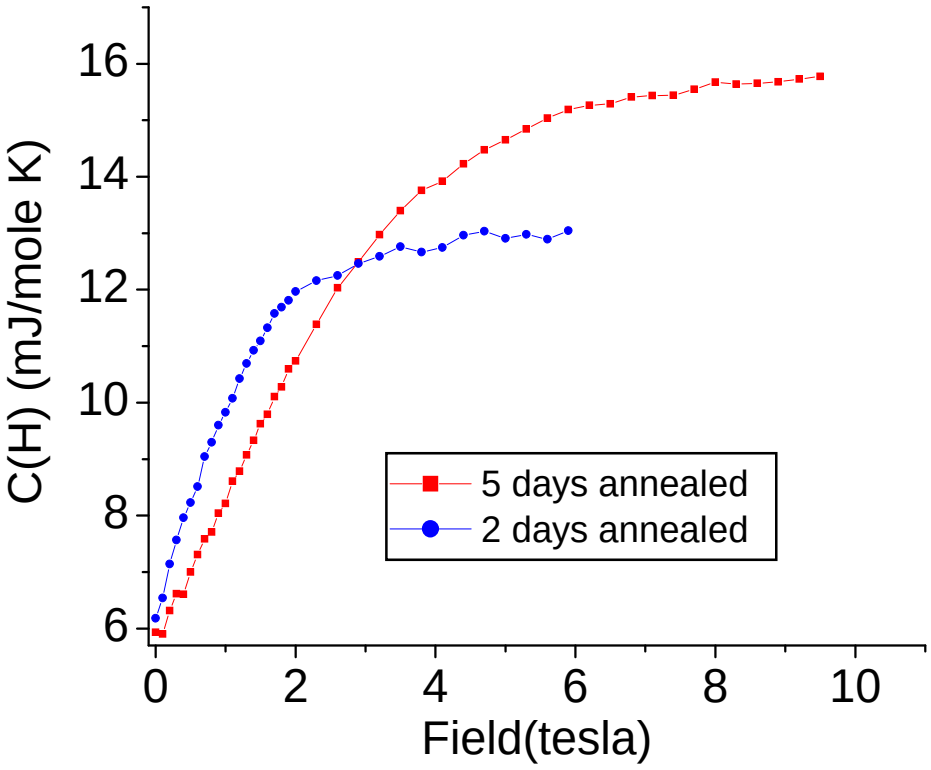

Figure 3.27: The field dependence of two PCCO x=0.15 crystals from the same batch annealed at 900^o for two days and five days. The temperature is 2K.

Fig. 3.26 shows T_c from magnetization measurements for two optimally cerium-doped crystals both of which were annealed at 900^oC but one for two days and the other for five days. The crystals from this batch (LH87) have been studied with WDX analysis and are known to have cerium variation between different crystals less than Δx=0.005. The size of the crystal which was annealed for two days is 6.9 mg, and the size of the crystal which was annealed five days is 2.9 mg. Fig. 3.26 shows that the T_c increases as the annealing time is increased, and the sample gets closer to optimum oxygen doping. In agreement with the magnetization measurements, the specific heat measurements also show a larger bulk H_{c2} for the crystal with longer annealing time. Fig. 3.27 shows the field dependence of the specific heat

of these two crystals. The measurement was performed at a constant temperature of 2K, and the magnetic field was ramped up after zero-field cooling.

It is also interesting to note that the specific heat of the crystals saturates at different values when driven into the normal state by applying a high enough magnetic field. The difference between the normal state specific heat values is mainly due to the electronic specific heat since we showed that annealing does not change the phonon contribution (see Fig. 3.25). The equality of the phonon contribution in the two crystals can also be seen from the equality of the zero field specific heat of these crystals in Fig. 3.27. A rough estimate of γ_n in the two crystals can be obtained by equating the change in the specific heat between 0T and 8T (or 6T in the case of the lower H_{c2} sample) to γ_nT. Then $\gamma_n \approx$4.6 mJ/moleK^2 for the five day annealed sample, and $\gamma_n \approx$3.1 mJ/moleK^2 for the two day annealed sample is obtained. $\gamma_n \approx$4.6 mJ/moleK^2 of the five day annealed sample is similar to γ_n=5.3 mJ/moleK^2 obtained on other optimally doped crystals (see Fig. 3.7-b), the small difference is due to different oxygen or cerium dopings, and also due to the approximate nature of extracting γ_n from a field scan at a non-zero temperature (γ_n=5.3 mJ/moleK^2 was obtained by extrapolating the linear dependence in the C/T vs T^2 plots at 10 T and 0 T to zero temperature).

These interesting results from H_{c2} and γ_n of crystals with same cerium doping but different oxygen content show that oxygen and cerium dopings have similar effects on the bulk properties of the crystal. Hence, it may be possible to extend the doping range accessible with cerium doping in the electron-doped cuprates by varying the oxygen content of the crystals.

3.7 Summary

Our specific heat measurements showed that the magnetic field dependence of the electronic specific heat is linear at the lowest temperatures in both optimal and over-doped crystals. At higher temperatures the field dependence is non-linear. However, the origin of this non-linearity is not clear at this moment. The possible explanations are d-wave symmetry at high temperatures, anisotropic s-wave symmetry, or some vortex effect independent of gap symmetry. The simplest of these explanations is the highly anisotropic (gap maximum approximately 15 times the gap minimum) s-wave gap. However, it is difficult to explain the persistence of the linear field dependence at 2K up to such high fields as a few tesla while non-linear field dependence dominates at just 3.5K. At this point a first order phase transition from d-wave to s-wave as the temperature is lowered would be an explanation for the persistence of the linear field dependence since a latent heat would be required to make the transition, and this latent heat could be large enough to prevent the field dependence to become non-linear even at a few tesla. The vortex-vortex interaction was used before in order to explain the non-linear field dependence in the conventional s-wave superconductor V_3Si, and a change in the size of the vortex core with magnetic field was suggested as the reason for the non-linear field dependence in $NbSe_2$. Our data qualitatively looks like the V_3Si data, however quantitatively the two data are very different. In our data the transition from non-linear to linear field dependence occurs within a temperature range ($\Delta T=1.5K=T_c/15$) which is much narrower than the transition in V_3Si ($\Delta T>4K=T_c/4$), which makes a vortex scenario unlikely. The absence of hysteresis in the specific heat as the field is ramped up and then down in our data (unlike the V_3Si data which shows a hysteresis) is an indication of the difference in the sample quality since this hysteresis is attributed to pinning of the vortices. In addition the non-linear field dependence in V_3Si is not observed when the field is ramped down (i.e. when vortex pinning effects are

eliminated), whereas in our case there is no difference between ramping the field up or down.

In addition to the symmetry of the order parameter the effects of oxygen doping on the bulk properties of crystals have been studied. It has been shown that variations in the oxygen content have similar effects on the bulk properties of the crystals as the variations in the cerium content.

Chapter 4

Nernst Effect of $Pr_{2-x}Ce_xCuO_4$

Introduction

In the last several years the efforts to understand the mechanism of HTSC have been concentrated on the normal state of these materials. These efforts have resulted in the discovery of a normal state gap, or pseudogap. Whether the pseudogap is related to the superconducting gap or is a different and independent gap has been a very important question for high temperature cuprate superconductors. One of the proposed explanations for the pseudogap has been in terms of the superconducting fluctuations. Because of its high sensitivity to superconducting fluctuations the Nernst effect has been a very important probe of the superconducting and the pseudogap states. In this chapter an explanation of the Nernst effect in terms of macroscopic quantities such as electrical and thermal conductivities is given first (a detailed microscopic picture of carrier transport is given in Appendix-A). This introduction is followed by a short discussion of the special case of Nernst effect in a two-band model. The chapter is concluded with our experimental results and their interpretation.

4.1 The Nernst effect

The Nernst effect is a thermomagnetic effect, in which a transverse potential difference is induced in the presence of a longitudinal thermal gradient and a perpendicular magnetic field. In a normal metal the charge carriers moving along a thermal gradient accumulate on the cold side of the sample and they induce an electric field opposing the thermal force. This electric field in turn induces an electric current in the opposite direction to the thermal current. In steady state these two currents are equal in magnitude and opposite in sign, so that J_x=0 (assuming the thermal gradient is in the $\hat{\mathbf{x}}$ direction). In the presence of a magnetic field along the $\hat{\mathbf{z}}$ direction, the carriers moving in $+\hat{\mathbf{x}}$ and $-\hat{\mathbf{x}}$ directions will be deflected to opposite sides along the y-axis (see Fig. 4.1). In the simplest case of a spherical Fermi surface and one type of carrier, these two currents will be equal to each other, and no transverse voltage will be induced. However in general the two currents will not cancel out exactly because of the energy dependence of the scattering time [90] (the significance of the energy dependence of the scattering time will become clear at the end of this section). In order to satisfy the boundary condition of J_y=0 (since it is an open circuit), a transverse potential has to be induced, which is the Nernst voltage.

Mathematically we can summarize these ideas by starting from the general equation:

$$\vec{J} = \bar{\sigma} \cdot \vec{E} + \bar{\alpha} \cdot (-\vec{\nabla} T), \tag{4.1}$$

where $\bar{\sigma}$ is the electrical conductivity tensor and $\bar{\alpha}$ is the thermoelectric (Peltier) tensor. Before starting the derivation of different quantities from this main equation, we should mention that $\sigma_{xy} = \sigma_{yx}$ and $\alpha_{xy} = \alpha_{yx}$. Solving Eq. 4.1 for J_x yields:

$$J_x = \sigma_{xx} E_x + \alpha_{xx}(-\partial_x T) + \sigma_{xy} E_y + \alpha_{xy}(-\partial_y T). \tag{4.2}$$

The first term in Eq. 4.2 is the current due to the electrical potential of the accumulating charge on the cold side of the sample, the second term is the thermal

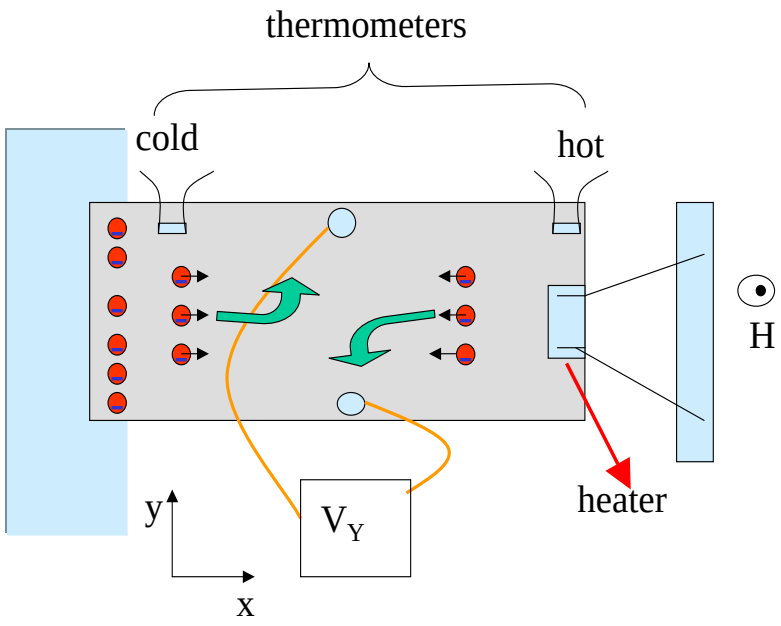

Figure 4.1: Schematic diagram of the Sondheimer cancellation. The dots are electrons.

current due to the applied temperature gradient. The third term can be ignored since $\sigma_{xy} \ll \sigma_{xx}$ [132](the ratio $\frac{\sigma_{xy}}{\sigma_{xx}} \approx 0.01$) and $E_y \ll E_x$ for a normal metal. The fourth term is due to the temperature gradient along y-axis(Righi-Leduc effect). The Righi-Leduc effect can be ignored for thin film samples since the substrate with its large phonon thermal conductivity acts as a shorting medium and prevents a transverse temperature gradient from being established. In measurements on crystals this term can not usually be ignored and it complicates the unambiguous determination of the Nernst signal. Ignoring the last two terms and imposing the boundary condition $J_x = 0$ on Eq. 4.2 results in:

$$E_x = \frac{\alpha_{xx}\partial_x T}{\sigma_{xx}}. \tag{4.3}$$

Solving Eq. 4.1 for J_y yields:

$$J_y = \alpha_{yx}(-\partial_x T) + \sigma_{yx}E_x + \sigma_{xx}E_y + \alpha_{yy}(-\partial_y T). \tag{4.4}$$

The first two terms in Eq. 4.4 are due to deflection of the carriers moving in the $\pm\hat{\mathbf{x}}$ directions (the two terms in Eq. 4.2) by the magnetic field (applied along the $\hat{\mathbf{z}}$ direction), the third term is the Nernst current, and the fourth term is the Righi-Leduc effect which is ignored for the thin film samples. Before deriving the equations for the Nernst effect a few remarks are necessary about the conventional way of representing the Nernst effect and the representation which will be followed in this thesis. The standard way of representing the Nernst effect in metals is by the Nernst coefficient $Q \equiv E_y/(\frac{1}{B}|\frac{\partial T}{\partial x}|)$. In the normal state of a superconductor, because of the linear field dependence of E_y (Lorentz force $q\vec{E} = -\vec{v} \times \vec{B}$), dividing $E_y/|\partial_x T|$ by the magnetic field is just a matter of scaling the signal with the applied field, and removing the field dependence. In analogy with the Hall effect, which is exactly the same as the Nernst effect except an electric current is applied along $\hat{\mathbf{x}}$ direction instead of a thermal gradient, the Nernst coefficient is same as the Hall coefficient. In both cases the slope of the linear field dependence is used to represent the effect. However in the mixed state of a superconductor the field dependence of the Nernst effect is not linear, and hence a linear scaling with the magnetic field does not have any meaning. In order to keep a consistent notation in the normal and the superconducting states, the Nernst effect is represented with $e_y \equiv E_y/|\partial_x T|$ rather than Q, and e_y is referred to as the **Nernst signal**. This Nernst signal has a linear field dependence in the normal state and a non-linear field dependence in the superconducting state.

By using Eq. 4.3 and Eq. 4.4 (after ignoring the last term), and the condition J_y=0, the following equation can be obtained:

$$\begin{aligned} E_y &= (\alpha_{yx}/\sigma_{xx})(\partial_x T) - (\sigma_{yx}/\sigma_{xx})E_x \\ \Rightarrow e_y &= \frac{\alpha_{yx}}{\sigma_{xx}} - \frac{\sigma_{yx}}{\sigma_{xx}}\frac{\alpha_{xx}}{\sigma_{xx}}. \end{aligned} \tag{4.5}$$

Eq. 4.5 can also be written in the more familiar form:

$$e_y = [\alpha_{yx}/\sigma_{xx} - S\tan\theta], \tag{4.6}$$

in terms of the thermopower $S = \alpha_{xx}/\sigma_{xx}$ and the tangent of the Hall angle $\tan\theta = \sigma_{yx}/\sigma_{xx}$, or just in terms of the thermopower:

$$e_y = S(\frac{\alpha_{yx}}{\alpha_{xx}} - \frac{\sigma_{yx}}{\sigma_{xx}}) \tag{4.7}$$

In order to further simplify Eq. 4.7, the expressions for α_{xx} and α_{xy} that are derived from microscopic considerations in Appendix-A (Eq. 5.24 and Eq. 5.25) should be used. For convenience these expressions will be given here again:

$\alpha_{xx} = \frac{\pi^2}{3}\frac{k_B^2 T}{e}(\frac{\partial\sigma_{xx}}{\partial\varepsilon})_\mu$

$\alpha_{xy} = \frac{\pi^2}{3}\frac{k_B^2 T}{e}(\frac{\partial\sigma_{xy}}{\partial\varepsilon})_\mu,$

where μ is the chemical potential and ε is energy. Then the Nernst signal becomes:

$$e_y = \frac{\pi^2}{3}\frac{k_B^2 T}{e}[\frac{\alpha_{xy}}{\sigma_{xx}} - \frac{\sigma_{xy}}{\sigma_{xx}}\frac{\alpha_{xx}}{\sigma_{xx}}] = \frac{\pi^2}{3}\frac{k_B^2 T}{e}\frac{\sigma_{xy}}{\sigma_{xx}}[\frac{\frac{\partial\sigma_{xy}}{\partial\varepsilon}}{\sigma_{xy}} - \frac{\frac{\partial\sigma_{xx}}{\partial\varepsilon}}{\sigma_{xx}}] \tag{4.8}$$

The last simplification that will be made in this discussion is to use the small angle approximation (this is justified since the Hall angle is usually very small in metals): $\tan(\theta) \approx \theta \approx \frac{\sigma_{xy}}{\sigma_{xx}}$ and replace $\frac{\sigma_{xy}}{\sigma_{xx}}$ by θ. This substitution results in:

$$e_y = \frac{\pi^2}{3}\frac{k_B^2 T}{e}\theta[\frac{\partial \ln\sigma_{xy}}{\partial\varepsilon} - \frac{\partial \ln\sigma_{xx}}{\partial\varepsilon}]|_\mu = \frac{\pi^2}{3}\frac{k_B^2 T}{e}\theta\frac{\partial \ln\theta}{\partial\varepsilon}|_\mu \tag{4.9}$$

Since the Hall angle depends primarily on the scattering time, the Nernst coefficient is usually known to give information about the energy dependence of the scattering time. In normal metals the Hall angle θ, and hence the scattering time, is only weakly energy dependent at the Fermi energy, therefore the Nernst signal is usually very small. However, as we will show in Section 4.2 this argument is no longer valid for a system that has two bands of conduction (two types of carriers). The Nernst effect for a system that has two bands of conduction is particularly important for PCCO since the unusual results of the prior transport experiments [133, 130, 132] were explained in terms of a two band model.

4.2 The Nernst effect in a two band model

The Nernst effect for a system that has two bands of conduction is particularly important for PCCO since the unusual results of the prior transport experiments [133, 130, 132] were explained in terms of a two band model. This means that there is a band in which electrons are the dominant carriers and another band in which holes are the dominant carriers. Having two bands for conduction significantly changes the normal state transport properties of these materials. Defining σ_{xx}^{+} as the hole component of the (1,1) element of the conductivity tensor, and σ_{xx}^{-} as the electron component of the same tensor element, the total conductivity can be written as $\sigma_{xx} = \sigma_{xx}^{+} + \sigma_{xx}^{-}$. Similarly the thermopower would be $S = \frac{\alpha_{xx}^{+}+\alpha_{xx}^{-}}{\sigma_{xx}^{+}+\sigma_{xx}^{-}}$. Since Eq. 4.7 is written in terms of electrical and thermoelectric conductivities, just replacing the single band conductivity with the addition of the conductivities from the two bands results in:

$$e_y = S\left(\frac{\alpha_{xy}^{+} + \alpha_{xy}^{-}}{\alpha_{xx}^{+} + \alpha_{xx}^{-}} - \frac{\sigma_{xy}^{+} + \sigma_{xy}^{-}}{\sigma_{xx}^{+} + \sigma_{xx}^{-}}\right) \tag{4.10}$$

In this case, the Nernst effect can be quite large depending on the relative Peltier and electrical conductivities of the two bands. Even in the case of compensated bands, $\sigma_{xy}^{+} = -\sigma_{xy}^{-}$, only the second term on the right hand side of Eq. 4.10 vanishes. The first term does not vanish since α_{xy}^{+} has the same sign as α_{xy}^{-} (since electrons and holes respond in the same way to a temperature gradient).

It is also instructive to understand the Nernst coefficient for a two band system in terms of the mobility of the charge carriers. For this we should start from Sondheimer's expression for a two band system (again + is for holes and - for electrons) [90]:

$$e_y(T) = \frac{e_y^{+}\sigma^{+} + e_y^{-}\sigma^{-}}{\sigma^{+} + \sigma^{-}} + \frac{\sigma^{+}\sigma^{-}(S^{+} - S^{-})(\sigma^{+}R^{+} - \sigma^{-}R^{-})}{(\sigma^{+} + \sigma^{-})^2}, \tag{4.11}$$

where R is the Hall coefficient and S is the thermopower. This formula can be written in terms of the mobilities by using the formulas $\mu^{+} = \sigma^{+}R^{+}$ and $\mu^{-} = \sigma^{-}R^{-}$. Then

Eq. 4.11 can be written as:

$$e_y(T) = \frac{e_y^+\sigma^+ + e_y^-\sigma^-}{\sigma^+ + \sigma^-} + \frac{\sigma^+\sigma^-(S^+ - S^-)(\mu^+ - \mu^-)}{(\sigma^+ + \sigma^-)^2}. \tag{4.12}$$

The first term in Eq. 4.12 is always small and its value changes smoothly from e_y^+ to e_y^- as σ^+/σ^- goes from very large to very small. However the second term can be very large since $sign[S^+] = -sign[S^-]$ and $sign[\mu^+] = -sign[\mu^-]$. This result is important because Nernst effect measurements on optimally cerium doped thin films of NCCO have shown a large change (more than two times) in the Nernst voltage when the oxygen content of the films was slightly changed ($\sim 1\%$). Such a small change in oxygen content can not change the carrier density (or the electrical conductivity) enough as to change the Nernst signal by a factor of two, but it could change the relative mobility of the carriers significantly by introducing disorder into the system. Therefore, in a two-band system not only the relative carrier concentration and the conductivities but also the relative mobilities are important.

A brief summary of the Nernst effect in the superconducting state is given in Chapter 1, hence it will not be repeated here. This concludes the introduction to the Nernst effect. The next section is a summary of the recent experimental results which motivated the work in this thesis.

4.3 Nernst effect as a probe of the superconducting fluctuations

Recently an anomalously large Nernst effect was reported in under-doped LSCO where a large Nernst signal persisted up to 100K above T_c [80]. In the following experiments this anomalous Nernst effect has been observed in almost all hole-doped cuprates, especially in the under-doped regime [80, 81, 82, 134, 83]. An example of this effect is shown in Fig. 4.2. Fig. 4.2-a shows the Nernst signal as a function of magnetic field for three different dopings of $Bi_2Sr_2CaCu_2O_8$ (Bi-2212) [134]. The

measurements are performed at the respective T_c of each compound: T=50K for the under-doped compound, T=90K for the optimally-doped compound and T=65K for the over-doped compound. The Nernst signal does not reduce to the normal state value (a few nV/K) even at magnetic fields as high as 30T. Fig. 4.2-b shows the magnetic field dependence of the Nernst effect at different temperatures in the under-doped Bi-2212. The T_c=50K for this compound but, as seen in the Fig. 4.2-b, 50K is not a special temperature for the Nernst effect, and the Nernst signal remains significantly larger than the normal state value up to T=100K. This temperature is twice the T_c, and it will be referred to as the onset temperature of the anomalous Nernst effect, T_ν. This large Nernst signal has been attributed to phase fluctuations in the superconducting order parameter [80]. Hence in this picture T_ν is the onset temperature of Cooper pair formation and T_c is the onset of macroscopic phase coherence between these Cooper pairs.

The onset temperature of this anomalous Nernst effect increases as the doping is reduced, which is analogous to the doping dependence of the onset temperature of the pseudogap, T^*, in these compounds (see Fig. 1.2 for the doping dependence of T^*). However T_ν is significantly less than T^*, $T_\nu \approx T^*/2$. The similarity between the doping dependence of the pseudogap onset temperature T^* and the onset temperature of anomalous Nernst signal T_ν has been proposed as evidence for a relation between the phase fluctuations and the pseudogap. However the difference in the magnitude of T_ν and T^* suggests that the pseudogap phenomena can not be explained solely by phase fluctuations in the superconducting order parameter.

These Nernst effect measurements have inspired a revisit to the theory of superconducting fluctuations in the cuprates. These theoretical studies have proposed that the anomalous Nernst effect can be explained in terms of various types of fluctuations or in terms of a preformed pair model. Kontani suggests that including antiferromagnetic fluctuations in addition to superconducting fluctuations in the under-doped regime would explain the unusually large Nernst signal above T_c [135].

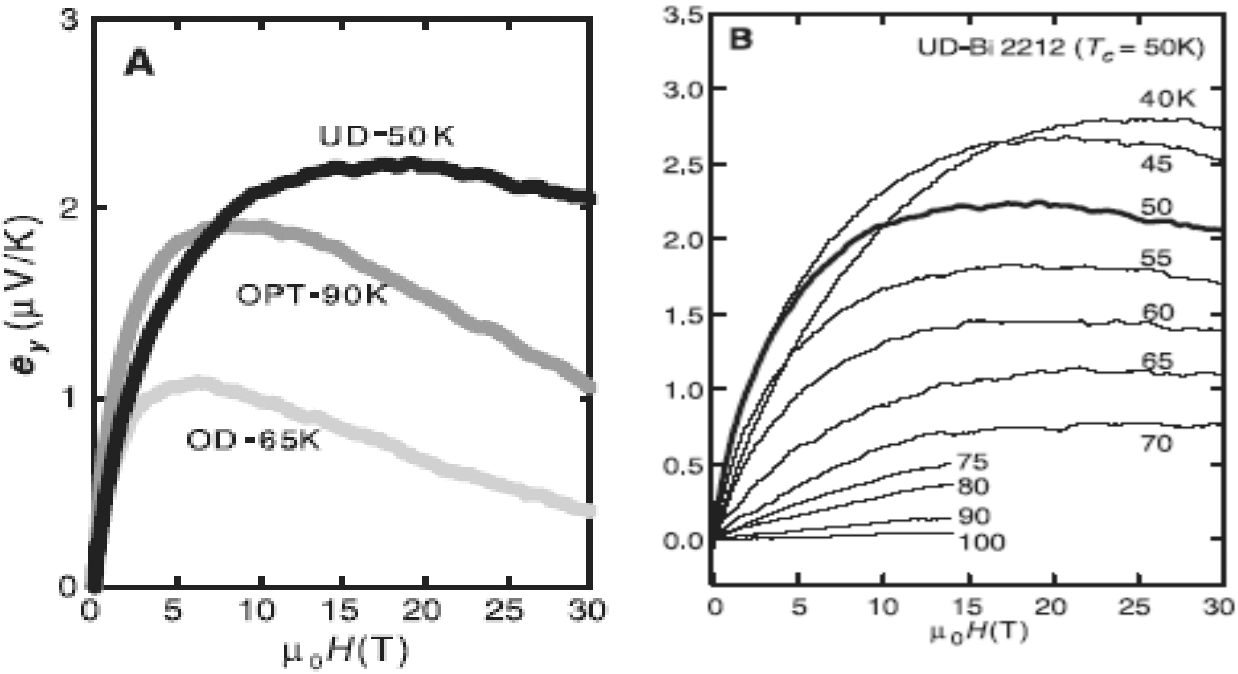

Figure 4.2: **A**-The Nernst effect on three different dopings of Bi-2212 hole-doped sample at their respective T_c's from resistivity. UD:under-doped, OPT:optimally-doped, OD:overdoped. The anomalous Nernst effect is most prominent in the under-doped compound, and in all dopings the anomalous signal persists to very high magnetic fields. **B**- The field dependence of the Nernst signal at different temperatures. The signal remains anomalously large up to 100K when the resistive T_c=50K. The data is from Ref. [134].

Ussishkin *et al.* [136, 137] suggest that Gaussian, non-interacting, superconducting fluctuations above T_c are able to explain the Nernst effect for the optimally-doped and over-doped regimes. For the under-doped regime they suggest that strong non-Gaussian fluctuations reduce the mean-field transition temperature T_c^{MF}, the theoretical transition temperature in the absence of any fluctuations, and therefore the mean field T_c^{MF} should be used in calculations instead of the actual T_c in order to take into account the contribution of the non-Gaussian fluctuations to the Nernst effect [136, 137]. Another proposal came from Tan *et al.* [138] in which they proposed a preformed pair alternative to the vortex-like excitations scenario to explain the anomalous Nernst effect in the under-doped hole-doped cuprates. Honerkamp and Lee [139] suggested that another ordered state (staggered flux state) similar in energy to the superconducting state should be created in the core of the vortices upon the destruction of superconductivity in order to explain the anomalous Nernst effect persisting up to very high temperatures. This would enable the creation of large numbers of vortices without costing too much energy (since the ground state in the vortex core and the superconducting state are similar in energy), and hence result in a large Nernst signal at temperatures significantly higher than T_c. The theoretical work of Emery and Kivelson [84] which preceded the Nernst effect measurements in under-doped cuprates and the follow-up work of Carlson *et al.* [11] are also important studies about the nature of superconducting fluctuations that should be mentioned. In this study the cuprates are classified in terms of their pairing strength (a measure of the superconducting gap) and phase stiffness (a measure of the superfluid density). The formation of the superconducting state requires both the formation of the Cooper pairs (determined by the pairing strength) and establishment of phase coherence between different pairs. The destruction of the superconducting state as temperature is increased is determined by the weaker of these effects. In conventional low-T_c superconductors the pairing strength is the weaker effect and, hence, it determines the disappearance of superconductivity. In

contrast, in the cuprates, it was found that T_c depends linearly on the carrier concentration (the Uemura plot [140]), and hence the T_c is determined, at least in the under-doped regime, by the superfluid density. This theory [11, 84] predicted that in the hole-doped cuprates the fluctuations in the phase of the order parameter would dominate the Nernst signal up to a certain temperature above T_c, and at still higher temperatures there should be contributions to the Nernst effect from fluctuations both in the phase and the amplitude of the order parameter (Gaussian fluctuations). The same study predicted that these fluctuations should be much smaller in the electron-doped cuprates. At present, none of the proposed explanations for the large Nernst signal observed in the hole-doped compounds have gained general acceptance.

Early measurements on hole-doped cuprates, which were concentrated on the optimally-doped regime, showed a large Nernst signal below T_c (the well known vortex Nernst effect) which diminished rapidly close to T_c (H_{c2}), and merged to the normal state Nernst signal [78, 79, 77]. This behavior was similar to that observed in conventional superconductors, except for a broader fluctuation regime. The Nernst effect studies in the electron-doped cuprate superconductors(all previous measurements were on $Nd_{1.85}Ce_{0.15}CuO_{4-\delta}$(NCCO)) showed the same behavior in the superconducting state. However, the normal state behavior was quite different [133, 130, 132]. An anomalously large Nernst voltage in the normal state was interpreted as evidence for the existence of two types of carriers, not vortex-like excitations. The two carrier interpretation has recently been supported for optimal-doping by ARPES measurements which showed electron pockets on a hole-like Fermi surface [24]. The doping dependence of the Nernst effect in the electron-doped superconductors was studied by varying the oxygen content of NCCO, but the cerium doping dependence was not investigated.

In this chapter we report Nernst effect data for the electron-doped superconductor $Pr_{2-x}Ce_xCuO_4$(PCCO) at different cerium dopings, and discuss some of the

important issues that were raised by the recent Nernst effect measurements on the hole-doped compounds. Magnetic field and temperature dependence of the Nernst voltage, and temperature dependence of H_{c2} close to T_c are presented. In addition, H_{c2} values obtained from Nernst effect and resistivity are compared. Unlike the recent results on some hole-doped compounds [80, 81, 82, 83], our data does not show an anomalous Nernst signal above T_c(or H_{c2}) for the optimally-doped and over-doped compounds. The under-doped compound shows a larger fluctuation regime but it is much narrower in temperature compared to the hole-doped materials. The H_{c2}(T) obtained from the Nernst effect follows a conventional linear temperature dependence close to T_c for all dopings we studied in contrast to an anomalous curvature found in many previous resistivity determinations of H_{c2}(T). The critical field, $H_{c2}(0)$, and the superconducting energy gap deduced from $H_{c2}(0)$ increase with decreasing doping even though T_c has a different doping dependence. The magnitude of the Nernst signal in the normal state is very similar for different cerium dopings. It is too large to be explained by a one carrier (one-band) model and it does not show the temperature dependence to be caused by vortex-like excitations or superconducting fluctuations. This suggests that two types of carriers (bands) exist in all the cerium dopings we studied and they are the origin of the large Nernst signal above T_c.

4.4 Samples and experimental setup

The measurements were performed on $Pr_{2-x}Ce_xCuO_4$ (x=0.13, 0.15, and 0.17) thin films grown by the pulsed laser deposition technique on $SrTiO_3$ (STO) substrates. The thickness of the films was around 3000 $\mathring{A}$. The sample was attached on one end to a copper block with a mechanical clamp (for better thermal contact), with the other end left free (see Fig. 4.3 for a similar holder which was used for the Nernst effect measurements in the PPMS).

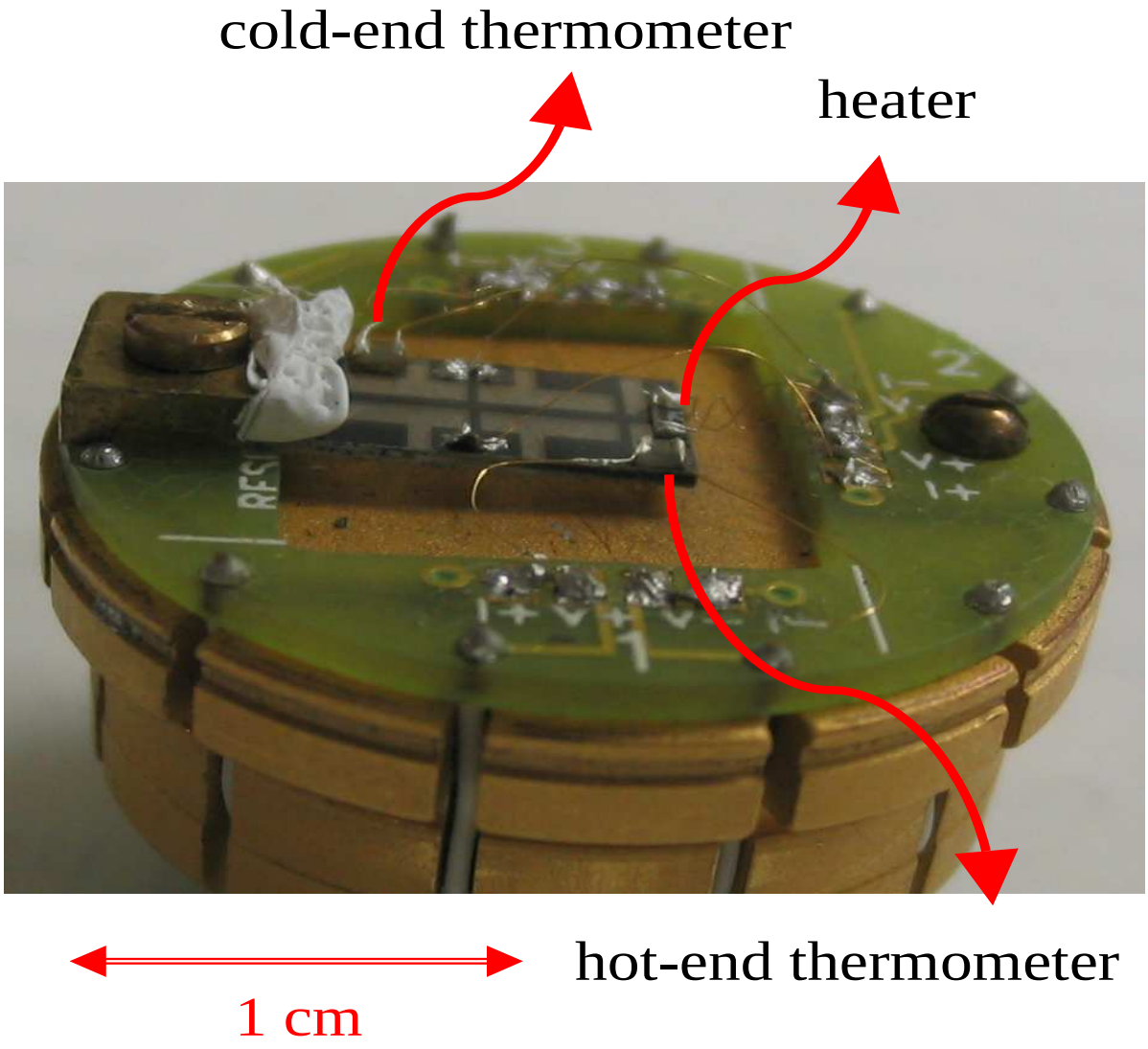

Figure 4.3: PPMS resistivity puck was modified to measure the Nernst effect. The home-made system also had a similar holder. The size of the sample is 5mm×10mm.

A temperature gradient was created by heating the free end with a small metal film heater attached on the film. Two Lakeshore cx-1030 cernox thermometers were attached on the two ends of the sample with a thin layer of GE 7031 varnish to monitor the temperature gradient continuously. The temperature gradient was between 1-2.5 K/cm depending on the temperature of the measurement. The temperature of the sample was determined by taking the average of the temperatures at the hot and cold sides. We calibrated the thermometers on the cold and hot sides of the samples together under the same conditions with respect to the same calibrated thermometer. The temperatures of the hot and cold ends of the sample were measured by continuously monitoring the resistance of the thermometers with two Keithley 182-nanovoltmeters and two Keithley 220 current sources. The resistance is then converted to temperature by using a Labview program that has the calibration file for the thermometers. This method of monitoring the temperature is better than using temperature controllers since the Keithley voltmeters have a much better GPIB interface than the temperature controllers. Also since the calibration file is kept in the computer, it is much easier to recalibrate the thermometers, and there is no limit on the number of points that could be used in the calibration file (as opposed to the 100 data points limit of the Lakeshore-93CA temperature controller). The background temperature was controlled by a Lakeshore-93CA temperature controller. All the data acquisition programs were written in Labview. The measurements were performed under vacuum, and the magnetic field was perpendicular to the ab-plane of the PCCO film. The Nernst voltage was measured with a Keithley 2182 Nanovoltmeter which has a sensitivity of several nanovolts. The copper wires that were used to measure the Nernst effect were taken from the top of the probe to the sample without going through any junction in order to minimize the stray thermal EMF that could be induced in such junctions. In other words the four-pin connectors that are usually used for thermalization of the wires coming from the top of the probe were eliminated and instead the wires were thermalized

by wrapping them around parts of the probe that have a strong thermal link with the 4.2 K helium bath. The wires measuring the Nernst voltage were isolated from the other wires by passing them through grounded copper tubes which is important for reducing the cross talk between the wires. The measurements were made at fixed temperatures while the field was scanned slowly at a rate of 20 Oe/sec. The temperature stability was a few millikelvins during the field scan. The Nernst signal is measured at positive and negative field polarity, and (1/2) the difference of the two polarities is taken to remove any thermoelectric power contribution due to the misalignment of the contacts.

4.5 Data and analysis

Fig. 4.4 shows the resistivity data for the films used in this study. The T_c, the sharpness of the superconducting transition, and the behavior of resistivity in high magnetic fields below the zero-field T_c(insulating-like for optimally-doped and under-doped samples, and metallic for over-doped samples) show the high quality of the films [129].

Fig. 4.5-a, -b, -c show the low temperature Nernst effect data for the three dopings we studied, and Fig. 4.5-d shows a comparison of the Nernst signal for the three dopings at $T/T_c \approx 0.7$. The superconducting vortex Nernst signal of the over-doped and optimally-doped samples crosses over to the normal-state Nernst signal(linear in magnetic field) very close to the resistive H_{c2} (for values of H_{c2}, see Table 4.1) . In the under-doped sample, the transition from the superconducting state to normal state occurs over a wider field range suggesting that the fluctuation regime is broader for the under-doped regime compared to the other dopings. Nevertheless in all three dopings the Nernst signal behaves very differently from the hole-doped cuprates in which an anomalous Nernst signal has been observed [80, 81, 82, 83]. In the electron-doped PCCO the peak of the vortex Nernst signal is quite sharp in all

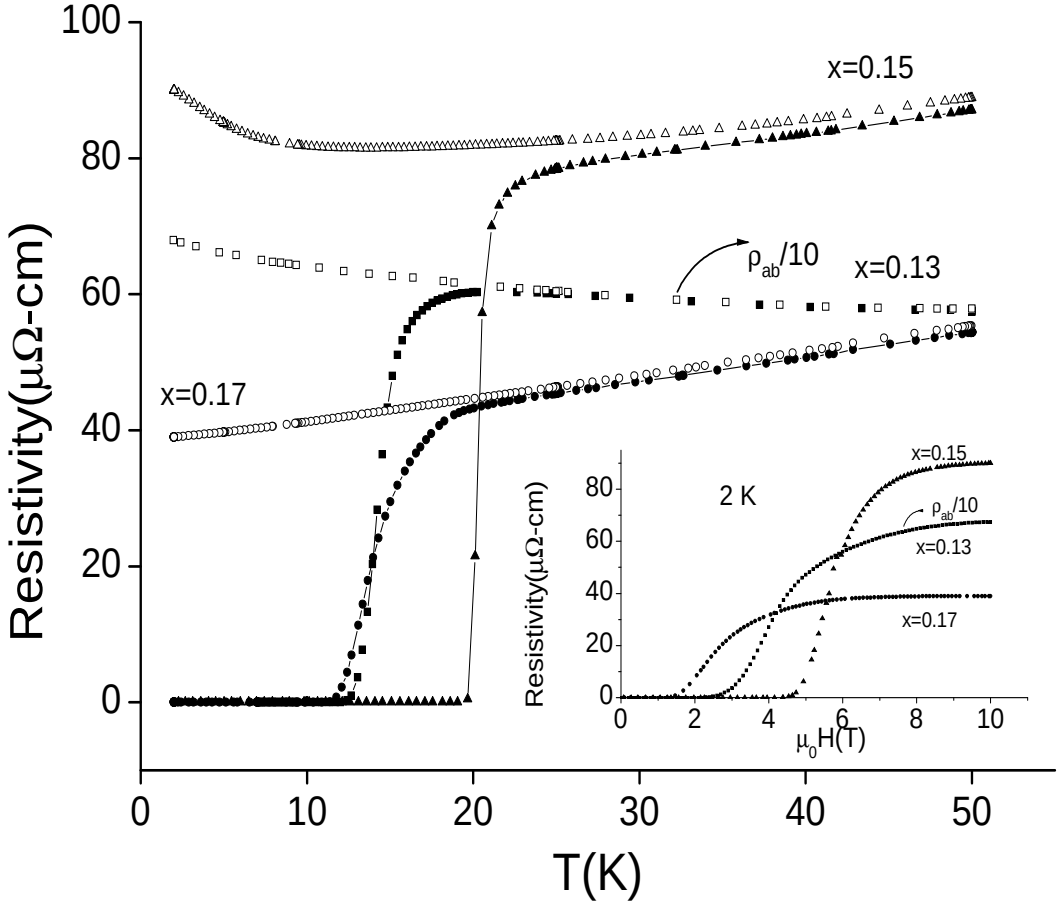

Figure 4.4: Resistivity of the optimal, over, and under-doped PCCO as a function of temperature at zero field (dark symbols) and H=14 T (open symbols). The inset shows the resistivity of the same samples as a function of field at T=2 K.

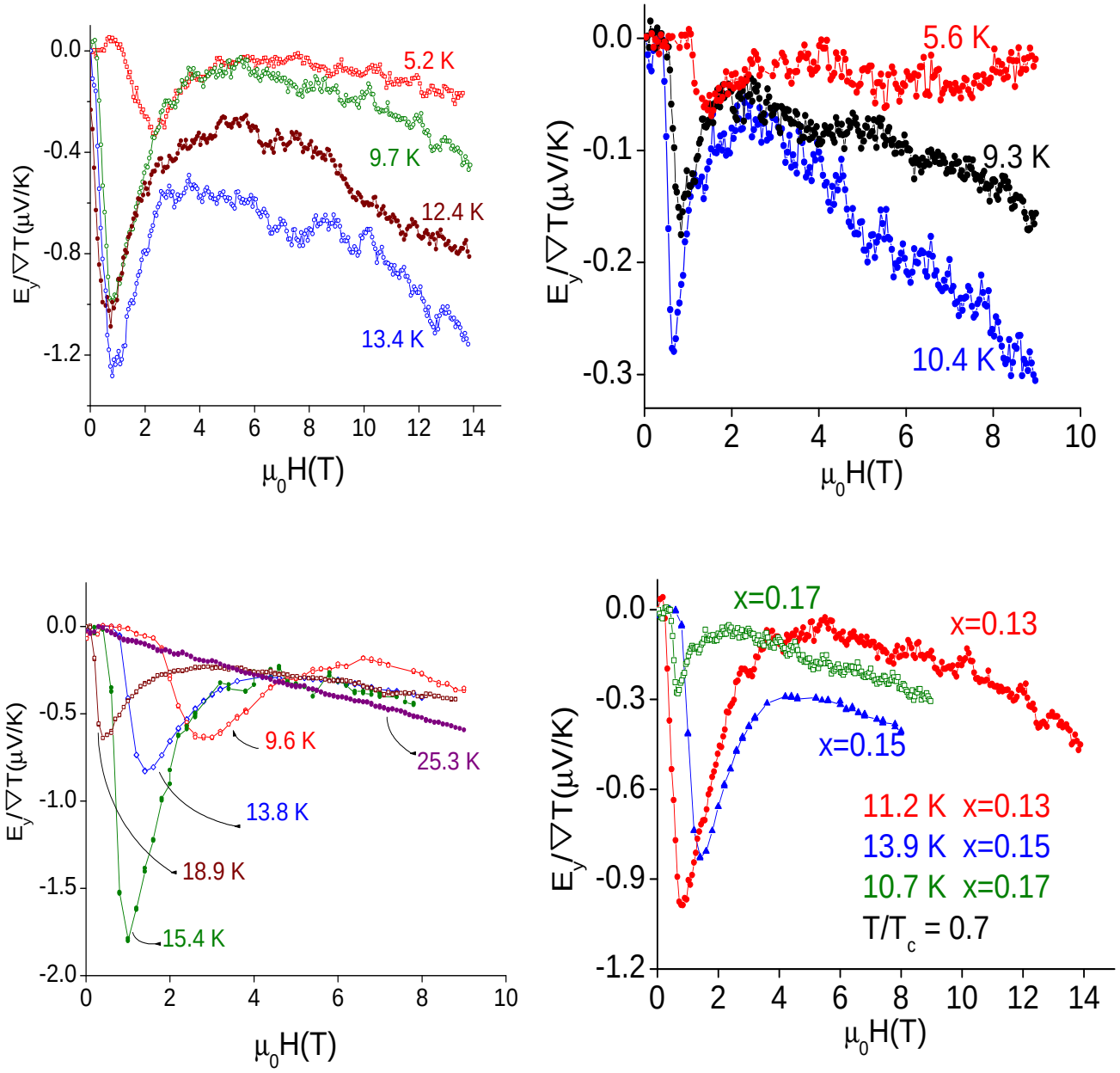

Figure 4.5: The low temperature Nernst effect of **(a)** the under-doped, **(b)** optimally-doped, **(c)** over-doped samples as a function of magnetic field at fixed temperatures. **(d)** shows a comparison of the three dopings at roughly the same T/T_c=0.7.

the dopings we studied. However, the hole-doped compounds [80, 81, 82, 83], particularly the under-doped compounds, show an extended peak for the vortex Nernst signal that persists to fields much larger than the resistive H_{c2} even at temperatures very close to T_c.

Fig. 4.6-a shows the typical Nernst effect for $T>T_c$ for the optimally-doped sample. The linear field dependence of the charge carrier Nernst effect is clearly seen, and no anomalous behavior is observed even at temperatures very close to the resistive T_c. Under-doped and over-doped samples behave very similarly to the optimally-doped sample, therefore the data for these dopings is not shown here. Fig. 4.6-b summarizes the temperature dependence of the Nernst signal at 9 T for $T>T_c$. The dome-like behavior that was observed in $Nd_{1.85}Ce_{0.15}CuO_{4-\delta}$ for different oxygen dopings [130, 132] is also observed in PCCO for different cerium dopings. A quantitative understanding of this temperature dependence is beyond the scope of this thesis. The large magnitude of the Nernst signal is also similar to that observed in NCCO for $T>T_c$. This large magnitude of the Nernst signal and some other observations that are discussed in detail in Ref. [130] were interpreted as evidence for the existence of two-types of carriers in electron-doped cuprates. In consistency with this previous interpretation, our present Nernst effect studies suggest that two-types of carriers exist in PCCO for all the cerium dopings we studied. Quantitative analysis of how two types of carriers are introduced in the system, and the variation of their concentration with cerium and oxygen dopings requires further systematic studies. We should also mention that the Nernst effect of some hole-doped compounds (especially at optimal doping) has been measured to high accuracy in the normal state up to room temperature. These experiments have shown that the Nernst signal decreases dramatically just above T_c, and remains less than 50 nV/K for temperatures up to 330 K [141, 142]. These signal levels are much smaller than what is found in PCCO suggesting one-type of carrier in the hole-doped cuprates.

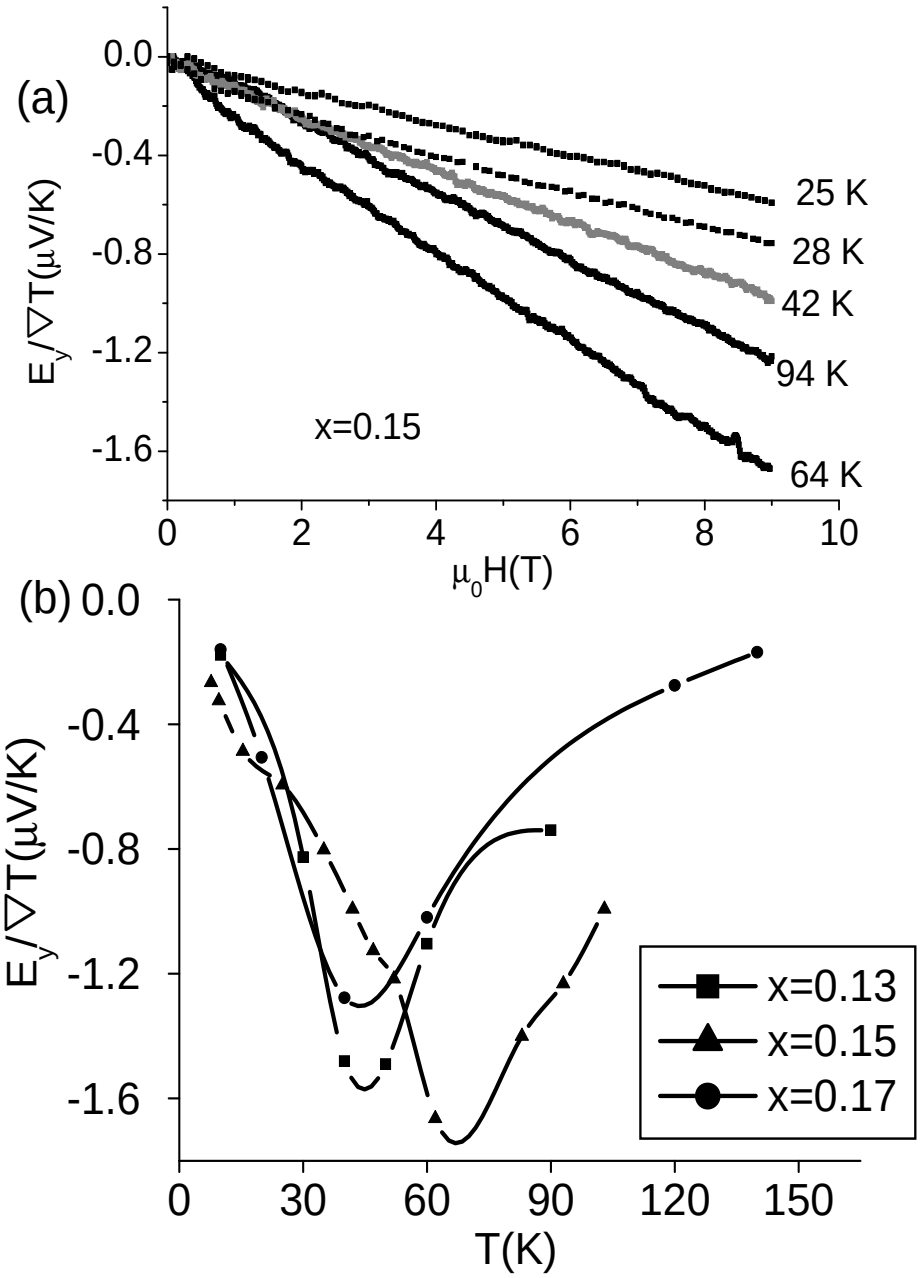

Figure 4.6: **(a)**-High temperature Nernst effect as a function of magnetic field for the optimally-doped sample. **(b)**- The temperature dependence of the Nernst effect at H=9 T for all dopings.

Whether the fluctuation region observed in the under-doped PCCO is related to the pseudogap state is an important issue. The experiments that studied the pseudogap state in electron-doped compounds have not yet produced conclusive results about either the magnitude or the onset temperature (T*) of the pseudogap. Tunnelling spectroscopy experiments have shown evidence for a low energy gap of magnitude comparable to the superconducting gap when the superconducting state is suppressed with the application of a strong enough magnetic field ($T^* \leq T_c$) [37, 85]. On the other hand, optical conductivity shows evidence for a high energy gap at 100-300 meV [143]. Other optical experiments ($T^* > 292$ K [86] and $T^*=110$ K [87]), and photoemission [88], and Raman spectroscopy [89] ($T^*=220$ K) experiments have also shown evidence for a high energy gap. Our Nernst effect data does not show a strong signal that could be related to a pseudogap. For example, in the hole-doped compounds where the anomalous Nernst effect has been observed [80, 81, 82, 83], there is no distinctive feature in the Nernst signal when crossing T_c (i.e. T_c does not seem to be a special temperature). This suggests that these excitations, which could originate at the pseudogap temperature (T*) dominate the signal around T_c. However, we should mention that this type of behavior is not found in all hole-doped cuprates. In some cuprates in which a pseudogap has been observed, the Nernst effect does actually show a transition from a large mixed state signal below T_c to an almost zero normal state signal just above T_c [144, 142]. This issue will be discussed more in the summary section. Our Nernst effect data shows a similar behavior around T_c to these systems, i.e. the distinctive vortex Nernst signal goes to a minimum and a clear normal state signal (linear in field) appears just above T_c (see Fig. 4.5 for example). Therefore, we conclude that there is no pseudogap state with associated superconducting fluctuations in this regime of the electron-doped superconductors. Of course a pseudogap of some other origin is possible. Quantitatively for the under-doped sample at $T \approx 15$K, where an anomalous signal would be expected, the normal state contribution is around 100

nV/K, which is small compared to the vortex-like signal of several μV/K around T_c for under-doped $La_{2-x}Sr_xCuO_4$(LSCO) [81].However, we can not rule out the existence of a weak pseudogap signal in PCCO that is dominated by the normal state (two-carrier) Nernst signal.

We now discuss the $H_{c2}(T)$ extracted from the Nernst signal (see Fig. 4.7-a). The dashed lines in Fig. 4.7-b show our method of extracting $H_{c2}(T)$. The uncertainty in the value of $H_{c2}(T)$ is found from the difference between the point of intersection of the dashed lines and the point one would get from extrapolating the vortex Nernst signal to zero. In our case extrapolating the vortex Nernst signal to zero is the same as extrapolating S_ϕ, the transport entropy per unit length of flux line, to zero since the flux flow resistivity is constant in the relevant field range ($S_\phi = \phi_o e_y/\rho_{ff}$, where ρ_{ff} is the flux flow resistivity and ϕ_o is flux quantum). Due to the complications of extracting the $H_{c2}(T)$ from S_ϕ that are detailed in Ref. [132] (usually $H_{c2}(T)$ is overestimated in this method), $H_{c2}(T)$ is not extracted from S_ϕ. In particular it was shown that determining $H_{c2}(T)$ from S_ϕ does not work at all for under-doped NCCO [132]. Therefore the errors in the value of $H_{c2}(T)$ are taken large enough to take into account this uncertainty. Considering the small difference between the $H_{c2}(T)$ values one would get by using different methods to determine it, some of the important results of this study would be valid in any of the methods used. One of these results is that $H_{c2}(0)$ increases with decreasing doping, since for a given T/T_c the signature of the normal state is seen at a larger field as the doping decreases. The other conclusion that would not change by the uncertainty in determining $H_{c2}(T)$ is that the fluctuation regime becomes narrower as the doping increases. This can be seen by comparing the close proximity of the vortex Nernst peak and the linear field dependent normal state contribution in the over-doped sample vs the broad transition region between these two typical regimes in the under-doped compound. However, one conclusion that would change for the under-doped compound is the linear temperature dependence of $H_{c2}(T)$. Using S_ϕ to determine $H_{c2}(T)$ would make

it very difficult to observe any systematic temperature dependence for $H_{c2}(T)$ as was also found in Ref. [132].

The $H_{c2}(T)$ of the optimally-doped sample shows a linear temperature dependence in the range of our Nernst effect data. $H_{c2}(0)$ is estimated using the Helfand-Werthamer formula [145]

$$H_{c2}(0) \approx 0.7 \times T_c \times \frac{dH_{c2}}{dT}, \tag{4.13}$$

where $\frac{dH_{c2}}{dT}$ is measured at T_c. $H_{c2}(0)$ for optimal doping is found to be 6.3±0.2 T, and therefore the coherence length of the optimally-doped sample is $\xi(0) \approx 75 \pm 2\mathring{A}$ (from $\xi^2(0) = \frac{\phi_o}{2\pi H_{c2}(0)}$) . The $H_{c2}(T)$ of the over-doped sample also shows a linear temperature dependence except for T>13 K where the superconducting-to-normal state transition starts. Using the Helfand-Werthamer formula $H_{c2}(0)$ is found to be 3.7±0.4 T, and $\xi(0) \approx 109 \pm 6\mathring{A}$. Due to the broad fluctuation region, where the Nernst signal had almost no field dependence, it was more difficult to determine $H_{c2}(T)$ for the under-doped sample. However, the fact that the normal state linear field dependence of the Nernst signal in the under-doped compound is observed at fields larger than that in the optimally-doped one suggests that $H_{c2}(T)$ is larger in the under-doped compound. A Helfand-Werthamer extrapolation to the $H_{c2}(T)$ vs T data for the under-doped compound yields $H_{c2}(0)$=7.1±0.5 and $\xi(0) \approx 71 \pm 3\mathring{A}$. For a summary of these results see Table 4.1.

Another important point that we should mention about the upper critical field is the difference in the sensitivity of the Nernst effect and resistivity in determining H_{c2}. The Nernst effect is very sensitive to superconducting fluctuations which are more difficult to observe in resistivity. This is particularly clear in the under-doped compound in which the onset of the normal state contribution is preceded by a wide fluctuation(Fig. 4.5-a) regime in the Nernst effect whereas the resistivity in the same field range is basically flat (Fig. 4.4). Resistivity measurements on PCCO and NCCO have shown the H_{c2} of the under-doped compound to be smaller than

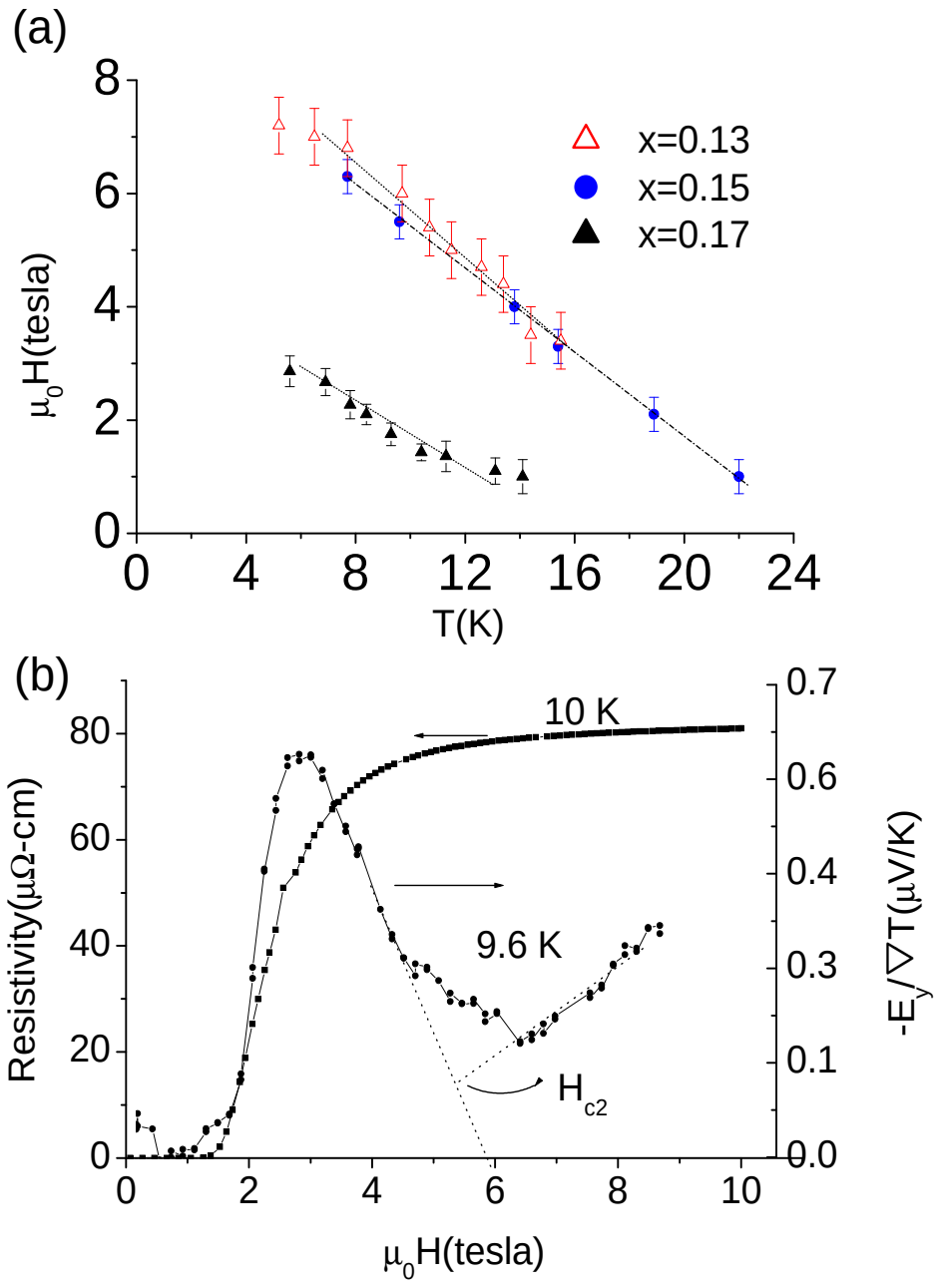

Figure 4.7: **(a)**-The upper critical field $H_{c2}(T)$ extracted from the Nernst effect data of Fig. 4.5 (and other data omitted from Fig. 4.5 for clarity). **(b)**-Comparison of Nernst effect and resistivity in terms of H_{c2} for x=0.15 sample. The dashed lines show the method used to extract H_{c2}.

sample	resistive T_c	$H_{c2}(0)$	$\xi_0(0)$	dH_{c2}/dT
x=0.13	14 K	7.1 T	7.1 nm	0.41 T/K
x=0.15	20.5 K	6.3 T	7.5 nm	0.37 T/K
x=0.17	14.4 K	3.7 T	10.9 nm	0.35 T/K

Table 4.1: A summary of the $H_{c2}(0)$, $\xi(0)$, and dH_{c2}/dT for different dopings determined from the Nernst effect.

that of the optimal-doped compound [146] (this can also be seen in the inset of Fig. 4.4). This would imply that the magnitude of the superconducting gap is larger in the optimally-doped compound ($\xi_0 \approx \frac{\hbar v_f}{\Delta_0}$, where v_f is the Fermi velocity). However, point-contact tunnelling experiments on similar samples have shown that the superconducting gap amplitude is larger in the under-doped compound compared to the optimally-doped one [37]. Our Nernst effect data explains this contradiction by the insensitivity of the resistivity to superconducting fluctuations, and implies that resistivity is not a proper measurement for determining H_{c2} in agreement with the conclusion of Ref. [146].

Resistivity and Nernst effect show similar $H_{c2}(T)$ for all dopings if the initial deviation from the normal state resistivity is chosen as a reference for $H_{c2}(T)$(see Fig. 4.7-b). The under-doped compound shows a larger difference between the Nernst effect and resistivity in terms of $H_{c2}(T)$, which suggests that the fluctuation regime is broader in the under-doped compound. A sample curve showing the superconducting-normal state transition from resistivity and Nernst effect is shown in Fig. 4.7-b) for the optimally-doped sample.

There are important similarities between our Nernst effect data and the recent

Nernst effect data on hole-doped Bi-2212($Bi_2Sr_2CaCu_2O_8$) and Bi-2201($Bi_2Sr_{2-y}La_yCuO_6$) [134]. Similar to our results, $H_{c2}(0)$ was found to increase with decreasing doping for both single layer and double layer Bi compounds studied in Ref [134]. These observations are consistent with other experiments showing an increasing superconducting gap ($\Delta_0 \propto v_f\sqrt{H_{c2}}$, where v_f is the Fermi velocity) amplitude with decreasing doping both for the n-doped and the p-doped cuprates [132, 23].

Summary

Unlike in the hole-doped cuprates where an anomalous Nernst signal has been observed, the vortex Nernst signal in the electron-doped PCCO does not persist above T_c or H_{c2} for over and optimal dopings. The T_c and H_{c2} extracted from the Nernst effect measurements for these dopings are similar to those obtained from resistivity if the start of the resistive superconducting transition is chosen as a reference for T_c or $H_{c2}(T)$. The under-doped compound shows a broader fluctuation regime, and therefore the superconducting to normal state transition look different in Nernst effect and resistivity. Above T_c the temperature dependence of the Nernst voltage is very similar for different dopings, and the magnitude of the Nernst signal is too large to be explained by a one-carrier model. These results are consistent with previous experiments on NCCO which were interpreted as evidence for the existence of a two-carrier transport in these materials [130].

The different behavior of the Nernst effect beyond the resistive T_c (or H_{c2}) for n-doped and the p-doped cuprates in which an anomalous Nernst signal is observed in the optimal and over-doping is a puzzling problem that remains to be resolved. However, it is clear that the large Nernst signal seen in the normal state ($T>T_c$) of the n-doped cuprates has a different origin than the anomalous Nernst signal observed in the p-doped compounds. In our data we see a clear distinction between the vortex Nernst effect contribution (a peak in the superconducting state) and the normal state contribution which is linear in magnetic field and which increases with temperature for $T>T_c$ up to $\sim$ 30 K above T_c. In contrast, the anomalous Nernst signal observed in some of the p-doped compounds is not distinct (there is no feature at or around T_c that would distinguish the two contributions) from the vortex Nernst contribution, and the signal decreases with temperature for $T>T_c$ up to 50 K above T_c [81].

In conclusion, we see a possible explanation in terms of superconducting fluctuations that can reconcile the n-doped and p-doped Nernst experiments. Non-Gaussian

fluctuations in the phase of the superconducting order parameter are dominant between T_c and the mean field critical temperature T_c^{MF}, but between this T_c^{MF} and the onset of the anomalous Nernst signal, T_ν, fluctuations both in amplitude and phase of the order parameter should be considered in order to explain the anomalous Nernst effect [136]. Vortex-like excitations above T_c might be an ambiguous way of describing this phenomenon since at such conditions (high density of fluctuations) the idea of a vortex becomes unclear. And also at temperatures $T>T_c^{MF}$ fluctuations in the amplitude of the order parameter are also important. Hence, this would make a vortex description of such fluctuations questionable since a certain amplitude stability is required for a vortex to be created. These fluctuations are smaller in the electron-doped cuprates due to two main reasons:

1. The effect of amplitude fluctuations is smaller in the n-doped cuprates because of a larger coherence length ($\sim$ 5 times larger in PCCO compared to LSCO).

2. The phase fluctuations that dominate around T_c for the hole-doped cuprates are smaller in electron-doped compounds since the phase stiffness temperature is comparable to the superconducting gap amplitude in these materials. For more details about this issue see Ref [11].

Another important issue that should be reconciled with the results of other experiments is the relation of the anomalous Nernst signal to the pseudogap. This issue will be discussed first for the hole-doped cuprates and then for the electron-doped cuprates.

In the hole-doped cuprates, the onset temperature (T_ν) of the anomalous Nernst signal is still much less than the pseudogap onset temperature observed in NMR [147, 148] or optical conductivity experiments [65, 149] for all the hole-doped cuprates in which an anomalous Nernst signal has been observed. This could imply two things: the anomalous Nernst signal is not related to the pseudogap or there is more than one source for a pseudogap like behavior which give rise to different gaps observed in NMR and the Nernst effect (i.e. multiple pseudogaps).

The fact that the anomalous Nernst signal is more pronounced in the underdoped regime, similar to the pseudogap observed in other experiments, suggests that the two phenomena are related. However, the variation of the strength of the pseudogap and anomalous Nernst effect with doping are not exactly the same. The strength of the pseudogap continues to increase even when the hole doping gets very small [65]. However, the strength of the anomalous Nernst effect peaks at a certain low hole doping (x≈0.1 in LSCO [81]), and decreases when the doping is further reduced. This difference suggests that even though the anomalous Nernst effect is related to the pseudogap, it can not account for all the pseudogap like behavior observed in hole-doped cuprates. The larger value of T^* compared to T_ν also supports the idea of a pseudogap different from that which gives rise to the anomalous Nernst effect. Another important fact that would support this idea is that the anomalous Nernst signal has not been observed in all the hole-doped cuprates that show evidence for a pseudogap above T_c (optimally-doped YBCO is one of these [79]).

The pseudogap detected in different experiments and the anomalous Nernst effect in electron-doped cuprates should also be reconciled. Tunnelling studies on electron-doped PCCO show a pseudogap that has an onset temperature $T^*<T_c$ [37, 150, 85]. It is not clear at this moment if this behavior can be reconciled with the other experiments that suggest a pseudogap at temperatures much higher than T_c. However, the pseudogap observed in tunnelling experiments does not conflict with the absence of a pseudogap in electron-doped cuprates since $T^*<T_c$. This would mean that even if there is an additional Nernst effect due to a pseudogap, it would be mixed with the large vortex Nernst effect, and it would not be detectable above T_c.

Clearly, more work on the nature of the pseudogap state in the n-doped cuprates needs to be done before any conclusive explanation of the n-doped and p-doped Nernst effect data can be made. At the present time a superconducting fluctuation

induced anomalous Nernst effect would appear to be most consistent with all the known experimental data.

Chapter 5

Conclusion

This chapter summarizes the contributions of this thesis to our understanding of high temperature superconductivity in electron-doped cuprates. First a summary of our results for specific heat then for Nernst effect measurements are given. The chapter is concluded with possible new experiments that would further advance our understanding of the electron-doped cuprates.

5.1 Summary of results for the specific heat measurements

Several important parameters have been determined for a member of the electron-doped family, $Pr_{2-x}Ce_xCuO_4$. The Debye temperature θ_D, Sommerfeld constant γ_n, and the coefficient of residual specific heat contribution at zero field $\gamma(0)$ are listed in Table 3.1.

The conventional method of studying the field dependence of the electronic specific heat is to measure the specific heat as a function of temperature at different fields. This data is then fit to a function of the form $C = [\gamma(H) + \gamma(0)]T + \beta T^3 + C_{Schottky}$, and $\gamma(H)$ is extracted for different fields. We have shown that the Schottky contribution, which has been an important obstacle in reliably extracting the

electronic contribution to the specific heat in the hole-doped cuprates, can be made negligibly small (for T>2K) in PCCO with properly prepared single crystals. This in turn eliminates the need for studying the temperature dependence of the specific heat at different fields (and the elaborate fitting required for each field), and makes it possible to study the field dependence of the electronic specific heat by just sweeping the field at a constant temperature. It is possible to take many more data points in the field range of interest (0-2T) in a reasonable time and the analysis of this data is much simpler in this method. Keeping in mind that the electronic contribution is often dominated by the phonon contribution and the Schottky contribution in most materials in the temperature range of this study, the advantage of our analysis is very clear.

By using these simple methods of data acquisition and analysis, the field dependence of the electronic specific heat is determined to be linear at the lowest temperatures studied (≈2K). **This result is valid for both optimal and over-doped crystals, and it is consistent in all the crystals we studied. Such a field dependence is consistent qualitatively and quantitatively with a fully-gapped order parameter in both the optimal and over-doped crystals of PCCO at low enough temperatures (T≈2K).** At higher temperatures both optimal and over-doped crystals show a non-linear field dependence which could have several different explanations: anisotropic s-wave gap, a phase transition from d-wave symmetry to s-wave symmetry, or a vortex effect independent of the gap symmetry. It is not possible at this moment to conclusively determine the correct explanation for this unusual field dependence or to completely rule out any of the possibilities.

Besides the gap symmetry of the electron-doped cuprates, the effects of oxygen reduction on the bulk properties of PCCO were studied. Our data shows that the as grown sample (unannealed, not superconducting) and the annealed sample (same sample but made superconducting after annealing) have the same Debye

temperature θ_D, and the same residual zero field specific heat coefficient $\gamma(0)$. On the other hand it is found that the bulk upper critical field H_{c2} and the Sommerfeld coefficient γ_n significantly vary between superconducting samples which are annealed differently and hence have different T_c's. In addition H_{c2} and γ_n are both smaller while $\gamma(0)$ is larger in the over cerium doped crystals. θ_D is the same in the optimal and over-doped crystals. It is also interesting to note that γ_n depends both on cerium concentration and oxygen concentration. Since γ_n is a measure of the density of states, this result suggests that oxygen reduction has similar effects on the density of states as the cerium doping.

5.2 Summary of results for the Nernst effect measurements

Our Nernst effect measurements do not show any anomalous Nernst effect. This result and the large anomalous Nernst effect of the hole-doped cuprates suggest that the superconducting fluctuations are responsible for the large Nernst signal observed above T_c in the hole-doped cuprates. However, unlike the fluctuations that are observed in conventional superconductors these fluctuations have a significant contribution from phase fluctuations. Particularly for the under-doped compounds the effect of these phase fluctuations has to be taken into account in order to explain the anomalous Nernst effect.

The upper critical field H_{c2} is determined from the Nernst effect. H_{c2} increases as the doping is decreased, and it has a linear temperature dependence for all dopings(for a summary of H_{c2} and the coherence length values in different dopings of PCCO see Table 4.1). The fluctuation regime in PCCO gets broader as the doping is reduced. In particular the broad fluctuation regime of the under-doped compound which is undetectable in the resistivity measurements shows that resistivity is not a

good probe of H_{c2}.

The magnitude of the Nernst effect in the normal state is too large to be explained by a one-band model. A two-band model in which each band has a different type of dominant carrier (electrons in one band and holes in the other) is required in order to explain the Nernst effect data in the normal state.

5.3 Future research

The current specific heat experiments suggest s-wave symmetry at low temperatures. However at high temperatures it is not clear whether the symmetry of the order parameter makes a phase transition to d-wave symmetry or remains s-wave (anisotropic s-wave). A possible experiment to clarify this issue is to observe the response of the electronic specific heat to non-magnetic impurities. An s-wave superconductor responds very differently from a d-wave superconductor to increasing concentration of impurities. Non-magnetic impurities induce pair breaking in a d-wave superconductor, but not in an s-wave superconductor (they merely reduce the size of the gap). This in turn increases the residual zero field specific heat in a d-wave superconductor but not in an s-wave superconductor [119]. In an anisotropic s-wave superconductor which has a non-linear field dependence similar to $\sqrt{H}$ in the clean-limit, the non-magnetic impurities induce a linear field dependence. In a d-wave superconductor with $\sqrt{H}$ type field dependence at the clean limit, the field dependence becomes $H \ln H$ type in the dirty limit. These distinctly different responses should make it possible to distinguish between anisotropic s-wave and d-wave symmetries.

Another possible experiment to distinguish the two possible scenarios of a phase transition in the order parameter and anisotropic s-wave symmetry is to check for latent heat (assuming the phase transition is first order) in the temperature range where such a phase transition is expected. In the optimally doped-sample such a

phase transition should occur around 3K. If this phase transition is of first order, which it is predicted to be [116], there should be a latent heat associated with this transition. The best way to test this idea is to measure the ac-heat capacity of the optimally doped sample at zero field. Zero field is important in order to eliminate any possible vortex effect, and ac-heat capacity is ideal method due to its sensitivity to phase transitions.

The correlation established between oxygen reduction and cerium doping on the bulk properties of crystals suggests that it might be possible to study the doping dependence of the gap symmetry and of the bulk properties of the crystal by varying the oxygen content. In particular under-doped crystals which proved to be very difficult to grow with cerium doping might be possible to obtain with oxygen doping. This idea could be tested by studying the same optimally-cerium doped sample before annealing, after a short annealing (like a few hours), then after optimal annealing time (5 days or more depending on the size of the sample), and finally after annealing the optimally-annealed sample in oxygen-rich environment. In this way it might be possible to study all the phase diagram on the same sample.

Another possible experiment is to study the specific heat of a crystal when the magnetic field is rotated within the ab-plane. This experiment is particularly important since for a d-wave superconductor depending on the orientation of the magnetic field (whether the field is along the nodal or antinodal direction) there is an anisotropy in the specific heat since the number of nodes contributing to the Doppler shift changes. When the magnetic field is along the antinodal direction all four nodes contribute to the specific heat while only two nodes contribute when the field is along the nodal direction, and hence there should be an anisotropy of $\sqrt{2}$ in the specific heat [45]. The interpretation of the results of this experiment could be complicated due to a possible anisotropic s-wave gap, nevertheless finding an anisotropy of $\sqrt{2}$ in the specific heat would be a strong evidence for d-wave symmetry.

The Nernst effect measurements could be expanded to study the evolution of the two-band conduction with doping. The Hall effect measurements on different dopings of PCCO have suggested that only in a certain doping range around the optimal doping should the two band effects be significant, and outside of this doping range the conduction should be dominated by one band. The conduction is dominated by the electron band in under-doped PCCO, and by holes in the over-doped PCCO. Measuring the Nernst effect, which has a distinctively different magnitude for one-band transport and two-band transport, and the Hall effect on the same samples should tell us the evolution of these bands on the Fermi surface with doping. In addition, the results of these measurements could be compared to the predictions of a model which attributes the formation of the two bands to opening of a spin density gap that separates the Fermi surface into two separate parts. This model predicts that the peak observed in the normal state in the Nernst effect around 50K-60K would shift to higher temperatures as the doping is reduced. This shift in temperature is due to the proximity to the AFM phase that is thought to be the reason for opening of a spin density gap.

Appendix A

Boltzmann Transport Theory

Boltzmann theory is the classical model that describes the transport properties of a system in steady state. This definition includes two of the important shortcomings of the theory. The first one is that it describes classical particles, therefore at best it can be used to describe a system in which the excitations can be represented with wave packets. More specifically the corresponding mean free path of the classical particles of Boltzmann theory should be larger than the wavelength of the quantum mechanical wave packet. The other shortcoming of the theory is that the system should be in steady state. Therefore it is assumed that if a system in equilibrium is somehow disturbed, another state will be reached in which the number of particles entering a small region is equal to the number of particles going out of that region.

The following treatment of the Boltzmann equation will basically be a summary and collection of the treatment from several chapters of J.M. Ziman's "Electrons and Phonons" [75].

The number of particles in a small region around $\vec{r}$ with a wave vector $\vec{k}$ is described by a distribution function $f_{\vec{k}}(\vec{r})$. The distribution function can change due to several reasons: diffusion, external fields, and scattering centers. Diffusion is the movement of particles in and out of a small region around $\vec{r}$ due to their diffusion velocity, $\vec{v}$. The time change of the distribution function due to diffusion

is given by:

$$\frac{\partial f_{\vec{k}}}{\partial t}|_{diff} = -\frac{\partial f_{\vec{k}}}{\partial \vec{r}}\frac{\partial \vec{r}}{\partial t} = -\frac{\partial f_{\vec{k}}}{\partial \vec{r}}\vec{v} \tag{5.1}$$

External electric and magnetic fields can also change the distribution function of the particles. They change the momentum of the carriers through the Lorenz force:

$$\hbar\dot{\vec{k}} = e(\vec{E} + \frac{1}{c}\vec{v}_k \times \vec{H}). \tag{5.2}$$

The number of particles with a given wave vector will change due to this change in momentum by:

$$\frac{\partial f_{\vec{k}}}{\partial t}|_{field} = -\frac{\partial f_{\vec{k}}}{\partial \vec{k}}\frac{\partial \vec{k}}{\partial t} = -\frac{e}{\hbar}(\vec{E} + \frac{1}{c}\vec{v}_{\vec{k}} \times \vec{H})\frac{\partial f_{\vec{k}}}{\partial \vec{k}}. \tag{5.3}$$

Another effect that can change the number of carriers entering or exiting a region is scattering with impurities or with other carriers. The effect of these collisions will be represented by :$\frac{\partial f_{\vec{k}}}{\partial t}|_{scat}$.

The total change in the distribution function is:

$$\dot{f}_{\vec{k}} = \dot{f}_{\vec{k}}|_{diff} + \dot{f}_{\vec{k}}|_{field} + \dot{f}_{\vec{k}}|_{scat}, \tag{5.4}$$

where the dot is used for the time derivative. In the steady state the number of particles entering a region should be equal to the number of particles exiting it: $\dot{f}_{\vec{k}} = 0$. Usually the scattering term is the most difficult term to determine, therefore the Boltzmann equation in steady state is written as:

$$\dot{f}_{\vec{k}}|_{diff} + \dot{f}_{\vec{k}}|_{field} = -\dot{f}_{\vec{k}}|_{scat}. \tag{5.5}$$

Or

$$-\frac{\partial f_{\vec{k}}}{\partial \vec{r}}\vec{v} - \frac{e}{\hbar}(\vec{E} + \frac{1}{c}\vec{v}_{\vec{k}} \times \vec{H})\frac{\partial f_{\vec{k}}}{\partial \vec{k}} = -\dot{f}_{\vec{k}}|_{scat}. \tag{5.6}$$

The experimentally accessible and practically important transport properties such as conductivity, Hall coefficient, thermoelectric power, etc can be calculated by solving

for $f_{\vec{k}}$. For example the current density is calculated by:

$$J = \int e\vec{v}_{\vec{k}} f_{\vec{k}} d\vec{k}. \tag{5.7}$$

Unfortunately these very general and simple ideas are not easily applicable to a complicated system like a metal in their most general form. Therefore some assumptions have to be made in order to simplify the problem. The most fundamental of these approximations is to assume that the mechanisms that were mentioned in the beginning of this section (diffusion, scattering, external fields) do not change the distribution function grossly, and that the steady state distribution function, $f_{\vec{k}}$ can be expanded around the equilibrium distribution function $f^0_{\vec{k}}$: $f_{\vec{k}} = f^0_{\vec{k}} + g(\vec{k})$, where g$(\vec{k})$ is a small disturbance on the equilibrium distribution function. Another common assumption is to assume that there is a characteristic relaxation time, τ, over which the carriers do not interact with the scattering centers like other carriers or impurities. In other words the system should exponentially relax to a steady state in the absence of any scattering processes. The relaxation time approximation can be mathematically summarized as:

$$\dot{f}_{\vec{k}}|_{scat} = -\frac{g(\vec{k})}{\tau}. \tag{5.8}$$

In general it is almost impossible to justify this assumption, and therefore the results of an analysis involving a relaxation time approximation should be considered only as an order magnitude type estimate of the real system.

Keeping these approximations in mind we can now study the Nernst effect starting from the Boltzmann theory. In the case of Nernst effect there is a longitudinal temperature gradient and a perpendicular magnetic field applied the sample. The temperature gradient has a diffusive effect and can be explicitly considered in the diffusion term:

$$\vec{v}_{\vec{k}} \cdot \frac{\partial f_{\vec{k}}}{\partial r} = \vec{v}_{\vec{k}} \cdot \frac{\partial f_{\vec{k}}}{\partial T} \nabla T. \tag{5.9}$$

Assuming that the temperature gradient is uniform throughout the sample and that

at any given point the distribution function, $f_{\vec{k}}$, deviates only slightly from a local equilibrium distribution function, $f^0_{\vec{k}}(r)$, the previous equation can be simplified as:

$$\vec{v}_{\vec{k}} \cdot \frac{\partial f_{\vec{k}}}{\partial \vec{r}} = \vec{v}_{\vec{k}} \cdot \frac{\partial f_{\vec{k}^0}}{\partial T} \nabla T. \tag{5.10}$$

The magnetic field on the other hand has a more complicated effect. The previous approximation of substituting $f^0_{\vec{k}}$ instead of $f_{\vec{k}}$ does not work:

$$\frac{e}{c}(\vec{v} \times \vec{H}) \cdot \frac{\partial f_{\vec{k}^0}}{\partial \vec{k}} = \frac{e}{c}(\vec{v} \times \vec{H}) \cdot \frac{\partial \varepsilon_{\vec{k}}}{\partial \vec{k}} \frac{\partial f_{\vec{k}^0}}{\partial \varepsilon_{\vec{k}}} = \frac{e}{c}(\hbar \vec{v} \times \vec{H}) \cdot \vec{v} \frac{\partial f_{\vec{k}^0}}{\partial \varepsilon_{\vec{k}}} = 0 \tag{5.11}$$

The magnetic field does not have any net effect on the equilibrium distribution. Therefore we should go to the next step in the approximation: $f_{\vec{k}} = f_{\vec{k}}{}^0 + g(\vec{k})$. Then the Boltzmann equation becomes:

$$\vec{v}_{\vec{k}} \cdot \frac{\partial f_{\vec{k}}{}^0}{\partial T} \nabla T = -\dot{f}_{\vec{k}}|_{scat} + \frac{e}{c\hbar}(\vec{v} \times \vec{H}) \cdot \frac{\partial g}{\partial \vec{k}} \tag{5.12}$$

Using the relaxation time approximation for the scattering term, $\dot{f}_k|_{scat} = -\frac{g(k)}{\tau}$, the Boltzmann equation can be further simplified. In addition it is more conventional, also easier, to measure the deviation from equilibrium in terms of the group velocity of the carriers, rather then its wave vector. This adjustment can be made by:

$$\frac{e}{c\hbar}(\vec{v} \times \vec{H}) \cdot \frac{\partial g}{\partial \vec{k}} = \frac{e}{c}(\vec{v} \times \vec{H}) \cdot \frac{\partial \vec{v}}{\partial \hbar \vec{k}} \cdot \frac{\partial g}{\partial \vec{v}} \tag{5.13}$$

The Boltzmann equation can now be written as:

$$\vec{v}_{\vec{k}} \cdot \frac{\partial f_{\vec{k}^0}}{\partial T} \nabla T = (\frac{1}{\tau} + \frac{e}{c}(\vec{v} \times \vec{H}) \cdot \frac{\partial \vec{v}}{\hbar \partial \vec{k}} \frac{\partial}{\partial \vec{v}}) g(\vec{v}) \tag{5.14}$$

This equation has the term

$$\mathbf{M}^{-1} = \frac{\partial \vec{v}}{\hbar \partial \vec{k}} \tag{5.15}$$

which is the inverse mass tensor (has the units of inverse mass). This term represents the response of a charge carrier to an applied field, and the sign of it determines whether holes or electrons are the charge carriers. In order to simplify our equation

further we assume that M^{-1} is constant over a constant energy surface (but it can be different at different energy surfaces) and replace it by a scalar mass 1/m*:

$$\vec{v}_{\vec{k}} \cdot \frac{\partial f_{\vec{k}^0}}{\partial T} \nabla T = (\frac{1}{\tau} + \frac{e}{m^* c}(\vec{v} \times \vec{H}) \cdot \frac{\partial}{\partial \vec{v}}) g(\vec{v}). \tag{5.16}$$

It is more conventional to look at the energy dependence of the distribution function rather than the temperature dependence. Hence the left hand side of the equation can be written as:

$$\vec{v}_{\vec{k}} \cdot \frac{\partial f_{\vec{k}^0}}{\partial T} \nabla T = \vec{v}_{\vec{k}} \cdot \frac{\partial f_{\vec{k}^0}}{\partial \varepsilon} \frac{\partial \varepsilon}{\partial T} \nabla T \approx \vec{v}_{\vec{k}} \cdot \frac{\partial f_{\vec{k}^0}}{\partial \varepsilon} (\frac{\varepsilon - \mu}{T}) \nabla T, \tag{5.17}$$

where μ is the chemical potential. The Boltzmann equation can then be written as:

$$\vec{v}_{\vec{k}} \cdot \frac{\partial f^0_{\vec{k}}}{\partial \varepsilon} (\frac{\varepsilon - \mu}{T}) \nabla T = (\frac{1}{\tau} + \frac{e}{m^* c}(\vec{v} \times \vec{H}) \cdot \frac{\partial}{\partial \vec{v}}) g(\vec{v}) \tag{5.18}$$

This equation can further be simplified by looking at the low magnetic field limit. For this we should first define a differential operator:

$$\Omega \equiv \frac{e\tau}{c\hbar} \vec{v} \times \vec{H} \cdot \frac{\partial}{\partial \vec{k}}. \tag{5.19}$$

The Boltzmann equation can then be written as:

$$(1 + \Omega) g(\vec{v}) = -\tau \vec{v}_{\vec{k}} \cdot \frac{\partial f_{\vec{k}^0}}{\partial \varepsilon} (\frac{\varepsilon - \mu}{T}) \nabla T$$

$$\Rightarrow g(\vec{v}) = -(1 + \Omega)^{-1} \tau \vec{v}_{\vec{k}} \cdot \frac{\partial f_{\vec{k}^0}}{\partial \varepsilon} (\frac{\varepsilon - \mu}{T}) \nabla T. \tag{5.20}$$

In small magnetic field limit we can expand $(1+\Omega)^{-1}$ as: $(1+\Omega)^{-1} \approx 1 - \Omega + \Omega^2 - \Omega^3 + ...$ If we substitute this back into the Boltzmann equation and keep only the first two terms of the expansion:

$$g(\vec{v}) = -(1 - \Omega) \tau \vec{v}_{\vec{k}} \cdot \frac{\partial f_{\vec{k}^0}}{\partial \varepsilon} (\frac{\varepsilon - \mu}{T}) \nabla T$$

$$= -(1 - \frac{e\tau}{c\hbar} \vec{v} \times \vec{H} \cdot \frac{\partial}{\partial \vec{k}}) \tau \vec{v}_{\vec{k}} \cdot \frac{\partial f_{\vec{k}^0}}{\partial \varepsilon} (\frac{\varepsilon - \mu}{T}) \nabla T \tag{5.21}$$

This solution is equivalent to determining g(v) accurate up to successive powers of $\vec{H}$ and ∇T. The zeroth order solution which is linear in ∇T would be:

$$g^{(0)}(\vec{v}) = \tau \vec{v}_{\vec{k}} \cdot \frac{\partial f_{\vec{k}^0}}{\partial \varepsilon} (\frac{\varepsilon - \mu}{T}) \nabla T. \tag{5.22}$$

Since the magnetic field is zero and only a thermal gradient is considered in this situation, $g^{(0)}$ is the deviation of the distribution function from the equilibrium for the diagonal component of the Peltier coefficient α_{xx}. By the same reasoning the first order term which is linear in ∇T and $\vec{H}$ gives the distribution function for the off-diagonal Peltier coefficient α_{xy}:

$$g^{(1)}(v) = \frac{e\tau}{c\hbar} \vec{v} \times \vec{H} \cdot \frac{\partial g^{(0)}(v)}{\partial \vec{k}} \tag{5.23}$$

α_{xx} and α_{xy} can be found by integrating the distribution functions $g^{(0)}(v)$ and $g^{(1)}(v)$, respectively, around the Fermi surface. For two-dimensional systems like the cuprates these integrals would result in:

$$\alpha_{xx} = \frac{\pi^2}{3} \frac{k_B^2 T}{e} (\frac{\partial \sigma_{xx}}{\partial \varepsilon})_\mu \tag{5.24}$$

$$\alpha_{xy} = \frac{\pi^2}{3} \frac{k_B^2 T}{e} (\frac{\partial \sigma_{xy}}{\partial \varepsilon})_\mu \tag{5.25}$$

These expressions for Peltier coefficients α_{xx} and α_{xy} are used in the previous section to derive the an expression for the Nernst effect using this microscopic treatment. These expressions for the Peltier coefficients are as far as we need from the microscopic treatment of the Nernst effect.

BIBLIOGRAPHY

[1] H. K. Onnes, Leiden Comm. **120b, 122b, 124c** (1911).

[2] L. N. Cooper, Physical Review **104**, 1189 (1956).

[3] J. Bardeen, L. N. Cooper, and J. R. Schrieffer, Physical Review **108**, 1175 (1957).

[4] H. Fröhlich, Physical Review **79**, 845 (1950).

[5] R. D. Parks, *Superconductivity vols I and II* (Marcel Dekker Inc., New York, 1969).

[6] G. Bilbro and W. L. McMillan, Phys. Rev. B **14**, 1887 (1976).

[7] J. G. Bednorz and K. A. Müller, Zeit. Phys. B **64**, 189 (1986).

[8] M. K. Wu, J. R. Ashburn, C. J. Torng, P. H. Hor, R. L. Meng, L. Gao, Z. J. Huang, Y. Q. Wang, and C. W. Chu, Phys. Rev. Lett. **58**, 908 (1987).

[9] H. Haeda, Y. Tanaka, M. Fukutami, and T. Asano, Jpn. J. Appl. Phys. **27**, L209 (1988).

[10] Z. Z. Sheng and A. M. Hermann, Nature **332**, 55 (1988).

[11] E. W. Carlson, V. J. Emery, S. A. Kivelson, and D. Orgad, Cond-mat **0206217** (2002).

[12] D. Pines and P. Monthoux, Journal of Physics and Chemistry of Solids (1995).

[13] D. Scalapino, Physics Reports **250**, 329 (1995).

[14] P. W. Anderson, P. A. Lee, M. Randeria, T. M. Rice, N. Trivedi, and F. C. Zhang.

[15] F. Bouquet, Y.Wang, I. Sheikin, T. Plackowski, A. Junod, S. Lee, and S. Tajima, Phys. Rev. Lett. **89**, 257001 (2002).

[16] Y. Tokura, H. Takagi, and S. Uchida, Nature **337**, 345 (1989).

[17] B. Khaykovich, Phys. Rev. B **66**, 014528 (2002).

[18] P. H. Hor, Y. Y. Xue, Y. Y. Sun, Y. C. Tao, T. J. Huang, W. Rabalais, and C. W. Chu, Physica C **159**, 629 (1989).

[19] S. Skanthakumar, J. W. Lynn, J. L. Peng, and Z. Y. Li, Phys. Rev. B **47**, 61736176 (1993).

[20] I. W. Sumarlin, S. Skanthakumar, J. W. Lynn, J. L. Peng, Z. Y. Li, W. Jiang, and R. Greene, Phys. Rev. Lett **68**, 2228 (1992).

[21] H. J. Kang, P. Dai, J. W. Lynn, M. Matsuura, J. R. Thompson, S.-C. Zhang, D. N. Argyriouk, Y. Onose, and Y. Tokura, Nature **423**, 522 (2003).

[22] G. M. Luke, Nature **338**, 49 (1989).

[23] A. Ino, C. Kim, M. Nakamura, T. Yoshida, T. Mizokawa, A. Fujimori, Z.-X. Shen, T. Kakeshita, H. Eisaki, and S. Uchida, Phys. Rev. B **65**, 094504 (2002).

[24] N. P. Armitage, D. H. Lu, C. Kim, A. Damascelli, K. M. Shen, F. Ronning, D. L. Feng, P. Bogdanov, Z.-X. Shen, Y. Onose, Y. Taguchi, Y. Tokura, P. K. Mang, N. Kaneko, and M. Greven, Phys. Rev. Lett. **86**, 1126 (2001).

[25] T. Yoshida, X. J. Zhou, T. Sasagawa, W. L. Yang, P. Bogdanov, A. Lanzara, Z. Hussain, T. Mizokawa, A. Fujimori, H. Eisaki, Z.-X. Shen, T. Kakeshita, and S. Uchida, Phys. Rev. Lett. **91**, 027001 (2003).

[26] C. C. Tsuei and J. R. Kirtley, Rev. Mod. Phys. **72**, 969 (2000).

[27] D. J. V. Harlingen, Rev. Mod. Phys. **67**, 515 (1995).

[28] D. H. Wu, J. Mao, S. N. Mao, J. L. Peng, X. X. Xi, T. Venkatesan, R. L. Greene, and S. M. Anlage, Phys. Rev. Lett **70**, 85 (1993).

[29] A. Andreone, A. Cassinese, A. D. Chiara, R. Vaglio, A. Gupta, and E. Sarnelli, Phys. Rev. B **49**, 6392 (1994).

[30] C. W. Schneider, Z. H. Barber, J. E. Evetts, S. N. Mao, and T. Venkatesan, Physica (Amsterdam) **233C**, 77 (1994).

[31] B. Stadlober, G. Krug, R. Nemetschek, R. Hackl, J. L. Cobb, and J. T. Markert, Phys. Rev. Lett. **74**, 4911 (1995).

[32] J. D. Kokales, P. Fournier, L. V. Mercaldo, V. V. Talanov, R. L. Greene, and S. M. Anlage, Phys. Rev. Lett. **85**, 3696 (2000).

[33] R. Prozorov, R. Giannetta, P. Fournier, and R. L. Greene, Phys. Rev. Lett. **85**, 3700 (2000).

[34] C. C. Tsuei and J. R. Kirtley, Phys. Rev. Lett. **85**, 182 (2000).

[35] T. Sato, T. Kamiyama, T. Takahashi, K. Kurahashi, and K. Yamada, Science **291**, 1517 (2001).

[36] G. Blumberg, A. Koitzsch, A. Gozar, B. S. Dennis, C. A. Kendziora, P. Fournier, and R. L. Greene, Science **88**, 107002 (2002).

[37] A. Biswas, P. Fournier, M. M. Qazilbash, V. N. Smolyaninova, H. Balci, and R. L. Greene, Phys. Rev. Lett. **88**, 207004 (2002).

[38] J. A. Skinta, M.-S. Kim, T. R. Lemberger, T. Greibe, and M. Naito, Phys. Rev. Lett. **88**, 207005 (2002).

[39] M.-S. Kim, J. A. Skinta, T. R. Lemberger, A. Tsukada, and M. Naito, Phys. Rev. Lett. **91**, 087001 (2003).

[40] K. A. Moler, D. J. Baar, J. S. Urbach, R. Liang, W. N. Hardy, and A. Kapitulnik, Phys. Rev. Lett. **73**, 2744 (1994).

[41] D. A. Wright, J. P. Emerson, B. F. Woodfield, J. E. Gordon, R. A. Fisher, and N. E. Phillips, Phys. Rev. Lett. **82**, 1550 (1999).

[42] Y. Wang, B. Revaz, A. Erb, and A. Junod, Phys. Rev. B **63**, 094508 (2001).

[43] M. Chiao, R. W. Hill, C. Lupien, B. Popic, R. Gagnon, and L. Taillefer, Phys. Rev. Lett. **82**, 2943 (1999).

[44] N. E. Phillips, CRC Critical Reviews in Solid State Sciences **December**, 467 (1971).

[45] N. E. Hussey, Advances in Physics **51**, 1685 (2002).

[46] C. Kittel, *Introduction to Solid State Physics*, 7th ed. (John Wiley & Sons, New York, 1996).

[47] M. Tinkham, *Introduction to Superconductivity*, 2nd ed. (McGraw-Hill, New York, 1996).

[48] N.P.Phillips, Phys. Rev. **114**, 676 (1959).

[49] W. S. Corak, B. B. Goodman, C. B. Satterthwaite, and A. Wexler, Physical Review **102**, 656 (1956).

[50] R. Radebaugh and P. H. Keesom, Physical Review **149**, 209 (1966).

[51] G. E. Volovik, JETP Lett. **58**, 469 (1993).

[52] C. Caroli, P. G. deGennes, and J. Matricon, Phys. Rev. Lett. **9**, 307 (1964).

[53] G. R. Stewart and B. L. Brandt, Phys. Rev. B **29**, 3908 (1984).

[54] N. W. Ashcroft and N. D. Mermin, *Solid State Physics* (Harcourt Brace College Publishers, Philadelphia, 1976).

[55] N. B. Kopnin and G. E. Volovik, JETP Lett. **64**, 690 (1996).

[56] H. Won and K. Maki, Europhys. Lett. **30**, 471 (1995).

[57] N. Schopohl and K. Maki, (1995).

[58] P. I. Soininen, C. Kallin, and A. J. Berlinsky, Phys. Rev. B **50**, 13883 (1994).

[59] A. J. Berlinsky, A. L. Fetter, M. J. Franz, C. Kallin, and P. I. Soininen, Phys. Rev. Lett. **75**, 2200 (1995).

[60] G. R. Stewart, Rev. Sci. Inst. **54**, 1 (1983).

[61] E. S. R. Gopal, *Specific Heats At Low Temperatures* (Plenum Press, 227 W. 17th St.,NewYork,N.Y.10011, 1966).

[62] Z.V.Kresin and S.A.Wolf, Phys. Rev. B **46**, 6458 (1992).

[63] N.P.Phillips, J.Supercond. **7**, 251 (1994).

[64] K. A. Moler, D. L. Sisson, J. S. Urbach, M. R. Beasley, A. Kapitulnik, D. J. Baar, R. Liang, and W. N. Hardy, Phys. Rev. B **55**, 3954 (1997).

[65] T. Timusk and B. Statt, Rep. Prog. Phys. **62**, 61 (1999).

[66] R. E. Glover, Phys. Lett. **25A**, 542 (1967).

[67] W. J. Skocpol and M. Tinkham, Rep. Prog. Phys. **38**, 1049 (1975).

[68] A. I. Larkin and A. A. Varlamov, *The Physics of Superconductors, Vol 1: Conventional and High-Tc Superconductors* (Springer, Berlin, 2003), chap. page 95.

[69] L. G. Aslamazov and A. I. Larkin, Fiz. Tverd. Tela (Sov. Phys. Solid State) **10**, 875 (1968).

[70] C. J. Lobb, Phys. Rev. B. **36**, 3930 (1987).

[71] D. S. Fisher, M. P. A. Fisher, and D. Huse, Phys. Rev. B. **43**, 130 (1991).

[72] S. Ullah and A. T. Dorsey, Phys. Rev. Lett. **65**, 2066 (1990).

[73] S. Ullah and A. T. Dorsey, Phys. Rev. B **44**, 262 (1991).

[74] R. J. Troy and A. T. Dorsey, Phys. Rev. B. **47**, 2715 (1993).

[75] J. M. Ziman, *Electrons and Phonons* (Oxford University Press, London, 1960).

[76] R. P. Huebener, *Magnetic Flux Structures in Superconductors*, 1st ed. (Springer-Verlag, Berlin, 1979).

[77] H. C. Ri, R. Gross, F. Gollnik, A. Beck, R. P. Huebener, P. Wagner, and H. Adrian, Phys. Rev. B **50**, 3312 (1994).

[78] S. J. Hagen, C. J. Lobb, R. L. Greene, M. G. Forrester, and J. Tallvachio, Phys. Rev. B **42**, 6777 (1990).

[79] M. Zeh, H. C. Ri, F. Kober, R. P. Huebener, A. V. Ustinov, J. Mannhart, R. Gross, and A. Gupta, Phys. Rev. Lett. **64**, 3195 (1990).

[80] Z. A. Xu, N. P. Ong, Y. Wang, T. Kakeshita, and S. Uchida, Nature **406**, 486 (2000).

[81] Y. Wang, Z. A. Xu, T. Kakeshita, S. Uchida, S. Ono, Y. Ando, and N. P. Ong, Phys. Rev. B **64**, 224519 (2001).

[82] Y. Wang, N. P. Ong, Z. A. Xu, S. Uchida, D. A. Bonn, R. Liang, and W. N. Hardy, Phys. Rev. Lett. **88**, 257003 (2002).

[83] C. Capan, K. Behnia, J. Hinderer, A. G. M. Jansen, W. Lang, C. Marcenat, C. Marin, and J. Flouquet, Phys. Rev. Lett. **88**, 056601 (2002).

[84] V. J. Emery and S. A. Kivelson, Nature **374**, 434 (1995).

[85] L. Alff, Y. Krockenberger, B. Welter, M. Schonecke, R. Gross, D. Manske, and M. Naito, Nature **406**, 486 (2000).

[86] E. J. Singley, D. N. Basov, K. Kurahashi, T. Uefuji, and K. Yamada, Phys. Rev. B **64**, 224503 (2001).

[87] C. C. Homes, B. P. Clayman, J. L. Peng, and R. L. Greene, Phys. Rev. B **56**, 5525 (1997).

[88] N. P. Armitage, D. H. Lu, C. Kim, A. Damascelli, K. M. Shen, F. Ronning, D. L. Feng, P. Bogdanov, Z.-X. Shen, Y. Onose, Y. Taguchi, Y. Tokura, P. K. Mang, N. Kaneko, and M. Greven, Phys. Rev. Lett. **87**, 147003 (2001).

[89] A. Koitzsch, G. Blumberg, A. Gozar, B. S. Dennis, P. Fournier, and R. L. Greene, Phys. Rev. B **67**, 184522 (2003).

[90] E. H. Sondheimer, Proc. R. Soc. London, Ser.A **193**, 484 (1948).

[91] B. Josephson, Phys. Lett. **16**, 242 (1965).

[92] F. Vidal, Phys. Rev. B **8**, 1982 (1973).

[93] J. L. Peng, Z. Y. Li, and R. L. Greene, Physica C **177**, 79 (1991).

[94] M. Brinkmann, T. Rex, H. Bach, and K. Westerholt, Phys. Rev. Lett. **74**, 4927 (1995).

[95] J. S. Kim and D. R. Gaskell, Physica C **209**, 381 (1993).

[96] I. J. Goldstein, D. E. Newbury, P. Echlin, D. C. Joy, A. D. R. Jr., C. E. Lyman, C. Fiori, and E. Lifshin, *Scanning Electron Microscopy and X-ray Microanalysis: A textbook for Biologists, Material Scientists, and Geologists*, 2nd ed. (Plenum Press, New York, 1992).

[97] E. F. Skelton, A. R. Drews, M. S. Osofsky, S. B. Qadri, J. Z. Hu, T. A. Vanderah, J. L. Peng, and R. L. Greene, Science **263**, 1416 (1994).

[98] R. B. Flippen, Phys. Rev. B **45**, 12498 (1992).

[99] R. W. Rollins, H. Küpfer, and W. Gey, Jour. Appl. Phys. **45**, 5392 (1974).

[100] R. Singh, R. Lal, U. C. Upreti, D. K. Suri, A. V. Narlikar, V. P. S. Awana, J. A. Aguair, and M. Shahabuddin, Phys. Rev. B **55**, 1216 (1997).

[101] K. H. Müller, Physica C **168**, 585 (1990).

[102] S. Lofland, M. X. Huang, and S. M. Bhagat, Physica C **203**, 271 (1992).

[103] C. H. Ho and A. Cezairliyan, *Specific Heat of Solids*, 1st ed. (Hemisphere Publishing Corporation, New York, 1988).

[104] R. Bachmann, F. DiSalvo, T. H. Geballe, R. L. Greene, R. E. Howard, C. N. King, H. C. Kirsch, K. N. Lee, R. E. Schwall, H.-U. Thomas, and R. B. Zubeck, Review of Scientific Instruments **43**, 205 (1972).

[105] P. F. Sullivan and G. Seidel, Phys. Rev. **173**, 679 (1968).

[106] Y. Kraftmakher, Phys. Rep. **356**, 1 (2002).

[107] J. S. Hwang, K. Lin, and C. Tien, Rev. Sci. Instr. **68**, 94 (1997).

[108] C. Kubert and P. J. Hirschfeld, Solid State Commun. **105**, 459 (1998).

[109] S. J. Chen, C. F. Chang, H. L. Tsay, H. D. Yang, and J.-Y. Lin, Phys. Rev. B **58**, R14753 (1998).

[110] M. N. Khlopkin, G. K. Panova, A. A. Shikov, and N. A. Chernoplekov, Phys. Solid State **41**, 1050 (1999).

[111] M. Sera, S. Shamoto, and M. Sato, Solid State Communications **72**, 749 (1989).

[112] S. C. Sanders, O. B. Hyun, and D. K. Finnemore, Phys. Rev. B **42**, 8035 (1990).

[113] N. Momono, T. Matsuzaki, M. Oda, and M. Ido, Jour. Phys. Soc. Japan **71**, 2832 (2002).

[114] R. A. Fisher, N. E. Phillips, A. Schilling, B. Buffeteau, R. Calemczuk, T. Hargreaves, C. Marcenat, K. W. Dennis, R. W. McCallum, and S. O'Connor, Phys. Rev. B **61**, 1473 (2000).

[115] Y. Sun and K. Maki, Phys. Rev. B **51**, 6059 (1995).

[116] V. A. Khodel, V. M. Yakovenko, M. V. Zverev, and H. Kang, cond-mat **0307454** (2003).

[117] V. M. Yakovenko, Private Communication.

[118] E. Boaknin, R. Hill, C. Proust, C. Lupien, L. Taillefer, and P. C. Canfield, Phys. Rev. Lett. **87**, 237001 (2001).

[119] M. Nohara, H. Suzuki, N. Mangkorntong, and H. Takagi, Physica C **341-348**, 2177 (2000).

[120] J. E. Sonier, K. F. Poon, G. M. Luke, P. Kyriakou, R. I. Miller, R. Liang, C. R. Wiebe, P. Fournier, and R. L. Greene, Phys. Rev. Lett **91**, 147002 (2003).

[121] M. Ichioka, A. Hasegawa, and K. Machida, Phys. Rev. B **59**, 184 (1999).

[122] P. Miranović, M. Ichioka, and K. Machida, cond-mat/0312420 17 Dec 2003.

[123] A. P. Ramirez, Phys. Lett. A **211**, 59 (1996).

[124] J. E. Sonier, M. F. Hundley, J. D. Thompson, and J. W. Brill, Phys. Rev. Lett. **82**, 4914 (1999).

[125] M. Hedo, Y. Inada, E. Yamamoto, Y. Haga, Y. Onuki, Y. Aoki, T. D. Matsuda, H. Sato, and S. Takahashi, Jour. Phys. Soc. Jap. **67**, 272 (1998).

[126] J. E. Sonier, F. D. Callaghan, R. I. Miller, E. Boaknin, L. Taillefer, R. F. Kiefl, J. H. Brewer, K. F. Poon, and J. D. Brewer, cond-mat/0401271 15 Jan 2004.

[127] H. Balci, C. P. Hill, M. M. Qazilbash, and R. L. Greene, Phys. Rev. B **68**, 054520 (2003).

[128] N. P. Armitage, F. Ronning, D. H. Lu, C. Kim, A. Damascelli, K. M. Shen, D. L. Feng, H. Eisaki, Z.-X. Shen, P. K. Mang, N. Kaneko, M. Greven, Y. Onose, Y. Taguchi, and Y. Tokura, Phys. Rev. Lett. **88**, 257001 (2002).

[129] P. Fournier, P. Mohanty, E. Maiser, S. Darzens, T. Venkatesan, C. J. Lobb, G. Czjzek, R. A. Webb, and R. L. Greene, Phys. Rev. Lett. **81**, 4720 (1998).

[130] P. Fournier, X. Jiang, W. Jiang, S. N. Mao, T. Venkatesan, C. J. Lobb, and R. L. Greene, Phys. Rev. B **56**, 14149 (1997).

[131] R. W. Hill, C. Proust, L. Taillefer, P. Fournier, and R. L. Greene, Nature **414**, 711 (2001).

[132] F. Gollnik and M. Naito, Phys. Rev. B **58**, 11734 (1998).

[133] W. Jiang, S. N. Mao, X. X. Xi, X. Jiang, J. L. Peng, T. Venkatesan, C. J. Lobb, and R. L. Greene, Phys Rev. Lett. **73**, 1291 (1994).

[134] Y. Wang, S. Ono, Y. Onose, G. Gu, Y. Ando, Y. Tokura, S. Uchida, and N. P. Ong, Science **299**, 86 (2003).

[135] H. Kontani, Phys. Rev. Lett. **89**, 237003 (2002).

[136] I. Ussishkin, S. L. Sondhi, and D. A. Huse, Phys. Rev. Lett. **89**, 287001 (2002).

[137] I. Ussishkin, Phys. Rev. Lett. **68**, 024517 (2003).

[138] S. Tan and K.Levin, Cond-mat **0302248** (2003).

[139] C. Honerkamp and P. A. Lee, Cond-mat **0309469** (2003).

[140] Y. J. Uemura *et al.*, Phys. Rev. B **68**, 909 (1988).

[141] J. Clayhold, Phys. Rev. B **54**, 6103 (1996).

[142] V. E. Gasumyants and N. V. Ageev, Phys. Rev. B **65**, 180515 (2002).

[143] Y. Onose, T. Taguchi, T. Ishikawa, S. Shinomori, K. Ishizaka, and Y. Tokura, Phys. Rev. Lett. **89**, 5120 (1999).

[144] J. A. Clayhold, A. W. L. Jr., F.Chen, and C.W.Chu, Phys. Rev. B **50**, 4252 (1994).

[145] N.R.Werthamer, E.Helfand, and P. C. Hohenberg, Phys. Rev. **147**, 295 (1996).

[146] P. Fournier and R.L.Greene, Phys. Rev.B **68**, 094507 (2003).

[147] W. W. W. Jr, R. E. Walstedt, J. F. Brennert, R. J. Cava, R. Tycko, R. F. Bell, and G. Dabbagh, Phys. Rev. Lett. **62**, 1193 (1989).

[148] M. Bankay, M. Mali, J. Roos, and D. Brinkmann, Phys. Rev. B **50**, 6416 (1994).

[149] D. N. Basov, R. Liang, B. Dabrowski, D. A. Bonn, W. N. Hardy, and T. Timusk, Phys. Rev. Lett. **77**, 4090 (1996).

[150] S. Kleefisch, B. Welter, A. Marx, L. Alff, R. Gross, and M. Naito, Phys. Rev. B **63**, R100507 (2001).